NASA Contractor Report 159189

ANALYTICAL MODELS FOR USE IN FAN INFLOW CONTROL STRUCTURE DESIGN--INFLOW DISTORTION AND ACOUSTIC TRANSMISSION MODELS

M. R. Gedge

UNITED TECHNOLOGIES CORPORATION
Pratt & Whitney Aircraft Group
East Hartford, Connecticut 06108

NASA Contract NAS1-15085
December 1979

National Aeronautics and
Space Administration

Langley Research Center
Hampton, Virginia 23665

NASA CR-159189

NASA

ANALYTICAL MODELS FOR USE IN FAN INFLOW CONTROL STRUCTURE DESIGN

Inflow Distortion and Acoustic Transmission Models

BY

M.R. GEDGE

Prepared under Contract No. NAS1-15085 by

United Technologies Corporation
Pratt & Whitney Aircraft Group
Commercial Products Division
East Hartford, Connecticut 06108

for

National Aeronautics and Space Administration
Langley Research Center
Hampton, Virginia 23665

Table of Contents

TABLE OF CONTENTS (Cont'd)

TABLE OF CONTENTS (Cont'd)

List of Figures

List of Figures (Cont'd)

List of Figures (Cont'd)

List of Figures (Cont'd)

1.0 SUMMARY

Significant differences exist in the noise generated by engines in flight and engines operating on the test stand. It has been observed that these differences are reduced by the use of an Inflow Control Structure in the static test configuration. It is the purpose of this contract (NAS1-15085) to produce a design system for inflow control structures. This interim report describes the results of the development of the analytical models required for this design system.

Characteristics of the fan inflow field are discussed based on observations of fan blade mounted pressure transducer and inflow hot film data. Models were developed to study the effect of flow contraction and screening on inflow distortions, to describe the acoustic characteristics - transmission loss and directivity change - of honeycomb and perforated plate, and to assess experimentally the directivity change due to a corner between honeycomb panels.

The primary results of this study are:

- The distortions in the engine inflow field during static operation are due to atmospheric turbulence, the nacelle boundary layer, exhaust flow reingestion, and flow over stand structure, the ground plane and the engine casing. The dominant factors depend on the configuration and ambient conditions.

- For the JT9D engine on the PWA test stand, the dominant factor in the distortion field is flow over stand structure and ground effects.

- Flow contraction suppresses, initially, turbulent axial velocity distortions and magnifies turbulent transverse velocity distortions.

- Perforated plate and gauze screens preferentially suppress the axial components of both steady and turbulent velocity distortions to a degree determined by the screen pressure loss coefficient.

- Honeycomb screens preferentially suppress the transverse components of both steady and turbulent velocity distortions, to a degree determined by the length to diameter ratio of the honeycomb. Values of this ratio as small as 2 or 3 produce large reductions in the transverse components.

- There is an observed tendency to isotropy in turbulent velocity fields. This relieves the anisotropy of the turbulent field found downstream of screens and limits the distortion of turbulence fields imposed by flow contraction.

- The acoustic transmission loss of perforated plate is controlled by the reactance of its acoustic impedance. A criterion is given for design of perforated plates having a transmission loss less than 1 dB in the frequency range of interest.

- The acoustic transmission loss of low solidity honeycomb screens is negligible for the external hemispherical design of inflow control structures.

- A model for the direction change due to a corner between honeycomb panels is compared to measured data and the comparison is good.

Based on these studies, certain qualitative design criteria have been identified.

2.0 INTRODUCTION

Reduction of jet engine noise levels is a continuing evolutionary process which has resulted in significant noise reduction since the advent of the original commercial jet aircraft in the early 1950's. Engine noise reduction features are usually verified by means of static or flight testing. Since the cost of flight testing is much greater than that of static testing, use of the latter technique results in significantly lower costs being accrued to the development of engine noise reduction features. As such, the use of static testing techniques should be fully exploited. The purpose of this contract is to develop, for turbofan engines, static testing techniques that result in measurements of fan noise that are representative of inflight levels.

It has been noted by various observers that the noise produced by the fan of turbofan engines operating statically on the test stand is greater than that produced when the engine is operating under flight conditions. This may be a result of both fan blade passing tone and broadband levels being contaminated by extraneous noise sources present during static testing. As a consequence, predictions of flight noise levels using static data are consistently high. A no less important ramification is that flight noise sources cannot be identified from noise measurements from statically operating engines. Correspondingly noise reduction techniques cannot be evaluated on the test stand in the presence of a contaminating noise floor. To identify the source of extraneous noise it is necessary to note that, statically, the fan interacts with a more distorted inflow field than it does when in flight. There are several distinct characteristics of the inflow field that are quite different when the engine is operating statically, each of which could produce extraneous noise.

Firstly, the ambient atmospheric turbulence field in the vicinity of the ground is more turbulent than at higher altitudes. In addition, this turbulence field is convected through a very high flow contraction when the engine is operating statically, whereas, in flight, the turbulence field convects through a very small contraction on its way to the fan. This high flow contraction in the static case results in a distortion of the field in which the "eddies" are "stretched", then "chopped" by successive fan blades, producing "bursts" of discrete noise that are virtually absent in the flight operation of the engine.

Secondly, in the static case, there exists stand structure and a ground plane that are sources of flow disturbances. Engine ingested air passes over the stand structure and the ground resulting in vortices and wakes in the inflow field. Engine case protuberances can also generate ingestible distortions. Usually these sources of distortion do not exist inflight since the air ingested into an engine has not passed over any boundaries.

Thirdly, the nacelle boundary layer is different during static operations of the engine. In flight, at takeoff and approach conditions, air is drawn into the engine through a streamtube forward of the engine, which is slightly larger than the fan, causing the locus of the stagnation points to be near the leading edge of the nacelle. In static operation, however, air is ingested from a much wider streamtube causing the stagnation locus to move rearward on the outside of the flight nacelle. The acceleration of the flow from this stagnation locus around the lip region produces higher local velocities than that occuring in flight and consequently, a larger adverse pressure gradient along the nacelle inner wall than that which is encountered inflight. The boundary layer then becomes thicker in this region and may even separate (the use of bellmouth inlets during static testing is an attempt to alleviate this situation). Due to these differences in boundary layers, the area of the fan tip that is affected by the boundary layer during static operation is probably larger. The nacelle boundary layer in static operation is also affected by the presence of free stream flow distortions which can locally perturb it. It seems probable, then, that the nacelle boundary layer generated by static operation of the engine constitutes a larger flow disturbance than its flight counterpart and thus could be a cause of higher noise levels.

Finally, since it is possible for the flow to be drawn from all angles by an engine on the test stand, turbulent flows from the jet plume may be reingested. This distortion source is not present in flight. These disturbances (i.e., atmospheric turbulence, ground plane and stand induced distortions, dissimilar nacelle boundary layer and jet plume reingestion) are considered to be the most important extraneous noise sources in static engine operation. In order to obtain useful static acoustic data, therefore, it is necessary to develop techniques which modify the inflow field so that, for all intents and purposes, the fan is operating as it would in flight. In the past, various techniques for accomplishing this simulation have been used, including mounting engines in wind tunnels and using devices upstream of the fan to condition the inflow. Inflow Control Structures (ICS) for conditioning the flow have been mounted upstream of the engine by several investigators. A boundary layer suction system has also been used in conjunction with a screen. Both of these techniques have resulted in reduced radiated noise levels, indicating the reduction of inflow distortion.

In view of the encouraging results achieved by the use of ICS's, the present contract was awarded for the purpose of developing an inflow control screen design procedure and a flight noise prediction procedure using data gathered from the static testing of engines equipped with such a structure. The use of wind tunnels, or other techniques for simulating the flight environment are not considered under this contract. In addition, the problem of nacelle boundary layer modification is not addressed under this contract, but is certainly an important area for future work. The major components of the contract are:

Phase I Definition of Atmospheric Turbulence Characteristics and Engine Sensitivity Study.

Phase II Development of Inflow Control Structure (ICS) Preliminary Design System.

Phase III Interim Procedures Report Development and Coordination.

This interim report describes the analytical models developed by the contractor that describe the physical processes involved in the passage of distortions and turbulence through contraction and screening and propagation of sound through screens. These models were developed under Phase II, Tasks A, C, D and E of the contract.

The report contains a brief survey of the literature relevant to inflow control screens followed by a discussion of the various design considerations, both acoustic and aerodynamic. Next, in order that the upwash velocity field at the fan face may be quantified using blade mounted pressure transducer (BMT) data, the relationship between the unsteady velocity field at the fan face and the pressure field at a point on a blade is discussed. (The screen design system will be assessed using this information in a subsequent portion of the contract). The analytical models of the effects of a screen and flow contraction on both steady and unsteady flow distortions are described. The acoustic characteristics of the screen components (including the transmission loss through the screen material and the directivity changes due to screen discontinuities) are then considered, followed by an experimental verification of the directivity model.

3.0 SYMBOLS

A Screen attenuation factor

$\mathcal{A}$ Defined in Section 10.0

a Characteristic dimension

a_o Speed of sound

B Screen process

$\mathcal{B}$ Defined in Section 7.0

b Wake width

C Contraction process

C_c Contraction coefficient

C_D Drag coefficient

C Fresnel integral

c Integration path

D Length of contraction

d Effective diameter of honeycomb

d Distance between ϵ-planes

E Constant in Section 7.0

e_1, e_2, e_3 Components of diagonal strain tensor

F Velocity one dimensional power spectral density

$\mathcal{F}$ Fourier transform of velocity field

f Frequency

G Geometric screen parameter

H Hankel function

$\mathcal{H}$ Defined in Section 8.0

h Plate separation

3.0 Symbols (Cont'd)

I	Intensity
I_1, I_2	Integrals
J	Defined in Appendix C
K	Screen pressure loss coefficient
$\mathcal{K}$	Defined in Section 8.0
$\underline{k}$	Wavenumber
L	Length scale
ℓ	Thickness of honeycomb or screen
ℓ_1	Contraction ratio
ℓ_c	Characteristic length in turbulence
M	Mach number
m	Defined in Appendix G
N	Filtering process
n	Index
P	Pressure power spectral density
p	Acoustic pressure amplitude
p	Instantaneous acoustic pressure
q	Dynamic head
R, Φ, Z	Cylindrical coordinate system
Re	Reynolds number
R	Resistive part of screen acoustic impedance
$\underline{r}$	Position vector
S	Sears response function
S	Fresnel integral
s	Screen solidity

3.0 Symbols (Cont'd)

T	BMT response function
$\mathcal{T}$	Defined in Section 10.0
t	Time
$\underline{U}$	Mean velocity
$\underline{u}$	Acoustic particle velocity amplitude
$\underline{u}$	Instaneous unsteady velocity
$\underline{V}$	Total velocity
V	Distortion velocity field
v	Fan face distortion velocity field
W	Defined in Appendix F
X	Distance downstream of rod
$\underline{x}$	Position vector
$\underline{Z}$	Impedance
z	Complex number
α	Screen flow angle ratio
β	Screen corner angle
Γ	Three dimensional velocity spectrum tensor
γ	Blade relative mean flow angle
δ	End correction
ϵ	Small distance
ζ	Phase difference
η	Lumley's RMS velocity ratio

3.0 Symbols (Cont'd)

θ	Angle
$\mathcal{K}$	Post contraction wavenumber
λ	Wavelength
μ_1, μ_2, μ_3	Mean squared velocity component ratios
ν	Kinematic viscosity
ξ	Distance
ρ	Air density
σ	Open area ratio
ϕ	Unsteady velocity potential
$\mathcal{X}$	Reactive part of screen impedance
Ψ	Stream function
$\underline{\Omega}$	Total vorticity
$\underline{\omega}$	Unsteady vorticity
ω	Radial frequency

Subscripts:

A	Pre, contraction or screen
a	Atmospheric turbulence
B	Post, contraction or screen
b	Stand structure induced
c	ICS induced (5.0), Honeycomb cell (E)
d	Inlet induced
F	In flight
I	Incident
i	Denotes velocity component
j	Denotes wavenumber component
l	Lower
n	Upwash
R	Reflected
S	Statically
s	Screen
T	Transmitted
t	Total
u	Upper

4.0 BACKGROUND AND LITERATURE REVIEW

It has long been known that the flight and static test environments of an engine are different. For instance, in 1966, Sofrin and McCann (1) recognized the existence of noise generation mechanisms peculiar to ground operation of an engine. They identified "natural atmospheric air currents" and ground vortices as causes of inflow distortion that, upon interaction with a rotor, produce noise. They also surmised that the inflow into a fan in flight was not distortion free, but probably had a different distortion flow field than which existed during static testing.

Subsequently, evidence accumulated (2, 3, 4, 5, 6) that showed not only were static and flight inflow distortions different, but that the static distortion field generated noise levels, especially blade passing tone levels (and possibly its harmonics) that were significantly greater than those generated in flight. However, while the source of the extraneous static noise is generally ascribed to the more disturbed inflow field, the particular distortion type responsible is not clearly defined. For example, Cumpsty and Lowrie (2) produced results that indicated that boundary layer changes were important at relative tip Mach numbers less than .85. In the flow outside the boundary layer, they suggest that distortions produced by the contraction of the ambient atmospheric turbulence field are important. Hanson's (7, 8, 9) measurements of inlet flow fields are explained by that author also as the result of contraction of the atmospheric turbulence, although, in some situations, he also identifies distortions due to flow over stand structure. Distortions have also been detected that were generated by protuberances on the exterior nacelle casing (10). Earlier work by Povinelli and Dittmar (11) identified distortions of the inflow by the installation structure. Hodder (12) examined among other things, the noise generated by a JT15D at two heights from the ground, and found the ground vortex interacting with the rotor to be a significant source. Recent P&WA/Boeing experience under the Joint Noise Reduction Program (JNRP) indicates that on a full size test stand, ground effects, stand structure and possibly atmospheric turbulence contribute to inflow distortions. The above review indicates that any or all of the distortion sources can exist but to a varying degree depending on the details of the test stand configuration.

In order to develop a design system for ICS's, it is necessary to quantify the effects of contraction and screening on inflow distortions that are convected into an engine inlet during static testing. Wind tunnel designers have used screens to suppress flow distortions, and as a result a body of literature has evolved describing the effects of screening on flow distortions. For example, Prandtl (16) had long ago determined that wind tunnel flows could be made steadier with gauze screens and honeycomb. He, and later Collar (17), and Batchelor (18) had attempted analyses of the phenomenon. However, it was Taylor and Batchelor (19) who derived a solution of small flow perturbations

convected through a gauze screen. They showed how two characteristics of the screen determine the degree of turbulence of steady distortion suppression. These are the pressure loss coefficient and the flow deflection ratio (the amount of turning of the flow caused by the gauze). Honeycomb, as shown by Lumley (20) acts in a similar manner. A significant factor in the use of screens for flow distortion suppression in wind tunnels is the consideration of the turbulence and distortions generated by the suppressing screens themselves. To minimize self generated turbulence and flow distortions, combinations of honeycomb and screening have been used (See for example, (21)). The body of literature described in this paragraph was used as the basis for developing the models described herein, which account for screen effects on turbulence and steady distortions.

The effects of contraction on turbulence and steady distortion have also been addressed in the literature, again motivated by the need for understanding these phenomena in the design of wind tunnels. Models for the effects of contraction were developed by Prandtl (16), Taylor (35), Kibner and Tucker (37), Batchelor and Proudman (38), and Pearson (39). These authors analyzed the problem using differing assumptions (See detailed discussion in section 7.2). Experimental results have also been reported in the literature, e.g., Townsend (42), Uberoi (38), Hussein and Ramjee (41) and Reynolds (43). Experimental results have been limited to contraction ratios that are small compared to those encountered in static engine operation. Comparisons of existing models with the available data show poor agreement. Postulated reasons for the discrepancies cited in the literature are discussed in section 7.2. In order to define contraction effects for the ICS design system required for this contract, the analytical results of the cited references will be used as a basis for the contraction model, and the results of the test program (Phase II, Task F) will be used to empirically correct the models. This interim report will describe the analytical development of the models.

Most published work to date on the use of screens to better simulate fan inflow fields for fan tests has been performed using model scale fans. The ICS's tested to date have been performed using model scale fans. These ICS's have been of the in-duct type and the externally mounted hemispherical type. The in-duct screen has consisted of either a honeycomb panel mounted upstream of the rotor (12, 22, 23) or multiple gauze screens at the inlet entrance (4) (It should be noted that the tests conducted by Jones et al was not a model test, but was conducted on a JT15D, a small turbofan, at a test stand).

All except Leggat and Siddon observed a reduction in tone level, however, these investigators did note a change in blade loading caused by the suppression of transverse velocities in a ground vortex. Suppression of this vortex nearer its stagnation point resulted in noise reductions. In conjunction with the noise reduction, Hodder (12) observed a reduction in axial length scale, as determined by making auto

correlations of the hot wire signal obtained at the fan face. Hodder ascribed the noise reduction to a change in length scale caused by the screen. However, Jones, et al, (23) demonstrated that honeycomb screens mounted in the inlet duct have a substantial acoustic transmission loss associated with them, so there is some question as to the reason for the noise reductions when the screens are mounted in the inlet, i.e., are they due to source noise reduction, transmission loss across the screen, or a combination of both?

The externally mounted hemispherical screens do not suffer from this problem of acoustic transmission loss to any great degree (27). In general, all screens of this type (13, 14, 23, 28, 29, 30) produced a significant reduction in tone noise, at subsonic relative tip Mach numbers, whether in the anechoic chamber, wind tunnel or on the test stand. The unsteadiness of the tone also decreased. These reductions were also observed with P&WA/Boeing JNRP screens mounted in front of a JT9D on the test stand. This noise reduction was accompanied by a reduction in turbulence level and scale. Only Shaw, et al, (13) show results in conflict with the scale reduction, but in this case, the screen was tested in a rectangular wind tunnel that was not much larger in height than the screen diameter. This situation could result in distortions generated by the screen itself. Based on this review of existing experience with inflow control structures, there appears to be a consensus that use of ICS's during static testing does result in a better simulation of flight fan noise generation mechanisms.

While universal screen design criteria have not yet been determined, certain desirable characteristics have emerged based on the literature reviewed. These characteristics are summarized below:

- The minimization of acoustic transmission loss is enhanced by use of external ICS's as opposed to use of ICS's mounted in the engine inlet.

- Distortion suppression, primarily of transverse velocities, is effected by use of honeycomb. Honeycomb characteristics suggested by Ho, et al, (31) are that a length to diameter ratio of 5 to 10 is necessary. However, Ginder (32) shows that increasing this ratio beyond 2 does not improve disturbance suppression. This latter view is born out, in some degree, by Prandtl (15).

- Axial velocity distortion suppression by use of gauzes or screens because of their relatively high pressure loss coefficients.

- Distortions generated by honeycomb structure can be suppressed by use of gauzes mounted downstream of the honeycomb, as suggested by the work in references (13), (21), (31) and (32).

- Gauzes, screens, and perforated plates can be mounted upstream of the honeycomb to protect it from damage by incoming debris.

- Inflow control devices should be designed to avoid large structural members and discontinuities (as noted by Lowrie and Newby (21) and PWA/Boeing experience) since they can give rise to self generated distortions entering the fan.

As can be seen from the above review of the literature, the feasibility has been shown of using an inflow control structure during static testing to effect a better simulation of the fan inflight flow field. Certain desirable characteristics of ICS designs have been identified, but as yet, a design procedure does not exist. Additionally, models describing the effects of screening and contraction on steady wake and turbulence distortion exist, although verifying test data for contraction ratios of the size encountered in static testing of fans does not exist. Additionally, there is only limited data on the effects of screening. Accordingly, the objective of the subject contract is to develop a procedure for design of ICS's by developing appropriate analytical models of screening, contraction and acoustic transmission effects and to provide the data required to empirically verify and/or correct these models.

5.0 INFLOW CONTROL STRUCTURE DESIGN CONSIDERATIONS

The inflow control screen has to perform the function of suppression, in some degree, of ambient flow distortions. It has to fulfill this requirement in such a manner that it does not itself produce significant flow distortions and such that the acoustic data, gathered when using it, is meaningful. Furthermore, the inflow control screen should not significantly affect the engine operating line. The criteria specifying the suppression, generation and acoustic effects of the inflow control screen are examined in the following subsections. In the following discussion, the term distortion velocity is used to indicate the fan face velocity induced beyond that which would exist if the fan were operating in isolation, in an undisturbed atmosphere.

5.1 Distortion Suppression Criteria

The use to which the acoustic data, gathered with an inflow control device in front of the fan is put, determines the criteria governing the design of the screen. Currently two uses are identifiable:

a) The acoustic data are corrected to give corresponding flyover levels.

b) The acoustic data are used to evaluate the effects of design changes on radiated noise levels. These changes may be made on full scale engine or on models.

The first data use requires that all screens should produce a fan face velocity field that is substantially the same as that in flight. The second data use requires that the screen suppress the fan face distortion field to flight levels, or to as low a value as possible, depending on whether the application is assessed of the impact of the change in flight noise levels or a scientific study where suppression of all inflow distortion sources is desired. To aid in considering what the criteria for simulation and minimization should be, a schematic diagram of the sequence of events involved in static and flight operation is shown in Figures 1 and 2. Considering Figure 1, four source types of fan inflow distortion are shown, i.e., atmospheric turbulence, distortions induced by stand structure, etc., distortions induced by the ICS and finally, inlet induced distortions. The boxes show the processes that alter these distortions, with C_{1aS} for example indicating alteration of atmospheric turbulence by contraction from the atmosphere to the screen, in the static case. B_a signifies its alteration by passage through the screen and C_{2aS} signifies the alteration caused by further contraction from the screen to the fan face. The alterations of the other disturbance sources are indicated in similar fashion. The static case without an ICS is obtained by noting that there is no attenuation by the screen. The processess shown in Figure 1 for each source type can be written symbolically as shown below in Equations 1, 2, 3 and 4.

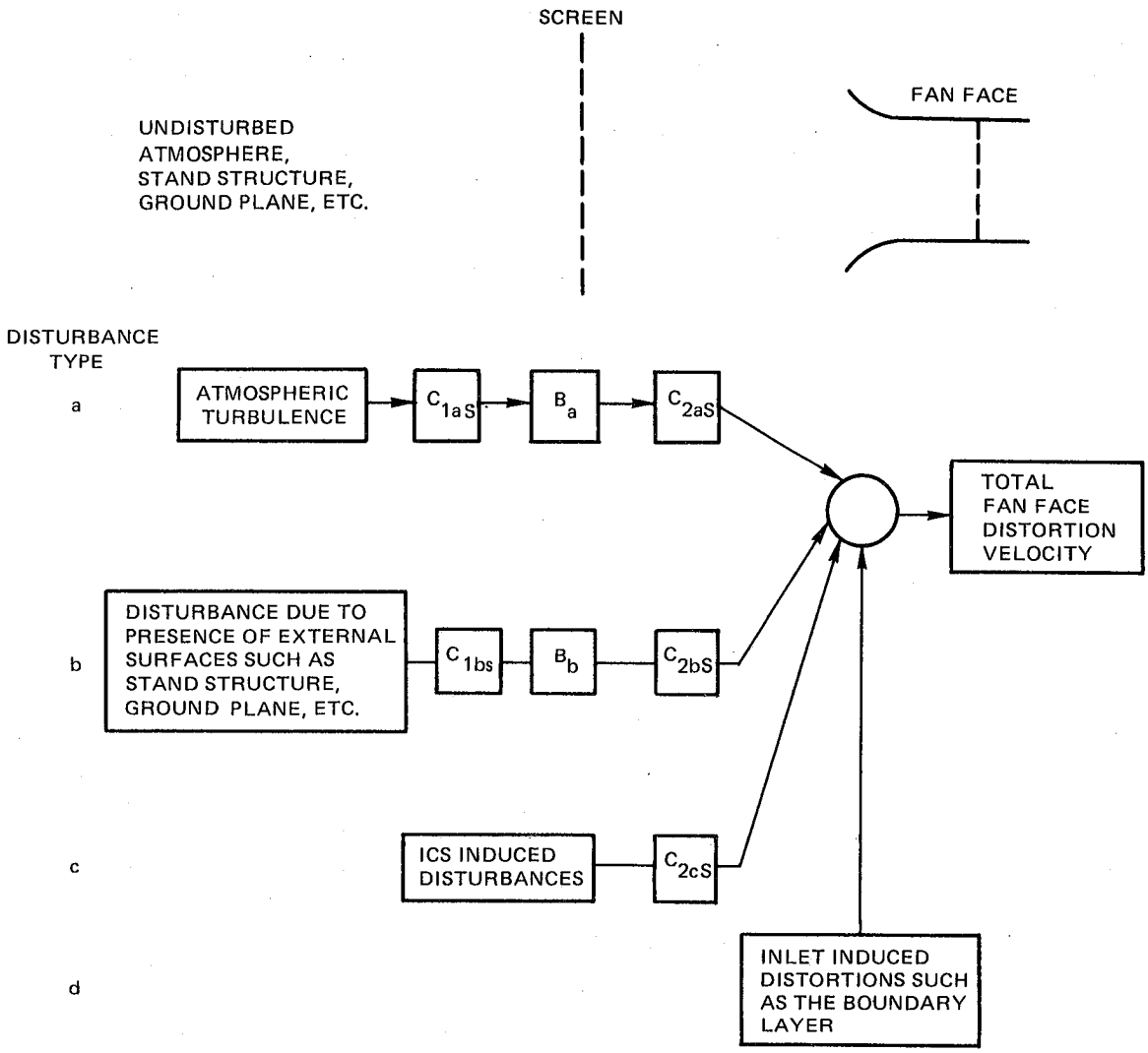

Figure 1 Sources of fan face distortion during static operation.

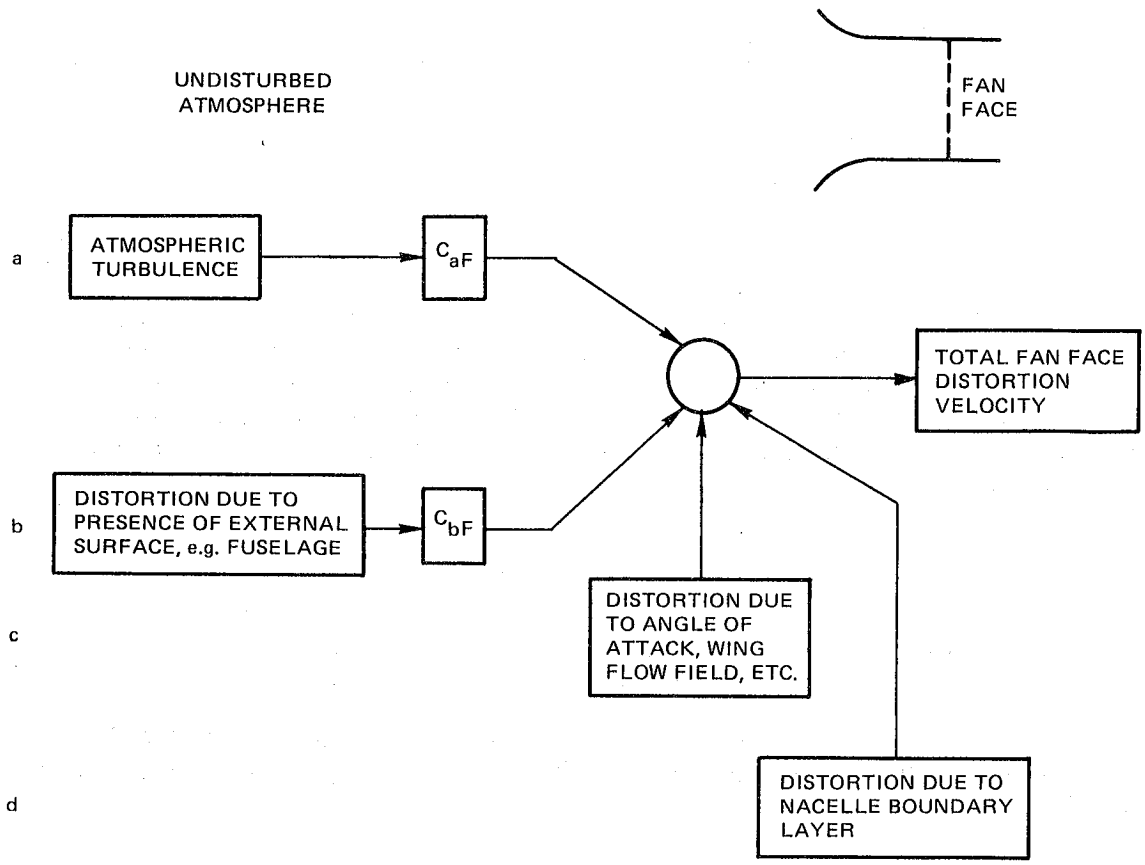

Figure 2 Sources of fan face distortion during flight operation.

$$V_{aS} = C_{2aS}\left[B_a\left[C_{1aS}\left[V_{aS}\right]\right]\right] \quad (1)$$

$$V_{bS} = C_{2bS}\left[B_b\left[C_{1bS}\left[V_{bS}\right]\right]\right] \quad (2)$$

$$V_{cS} = C_{2cS}\left[V_{cS}\right] \quad (3)$$

$$V_{dS} = V_{dS} \quad (4)$$

where the variables $V_{aS}, V_{bS}, V_{cS}, V_{dS}$ represent distortion velocities as they exist at the source, $V_{aS}, V_{bS}, V_{cS}, V_{dS}$, represent the distortion velocities at the fan face under static conditions and the symbols $C[\,]$ and $B[\,]$ represent operators for alterations caused by contraction and screening. The total fan face distortion velocity is the summation of Equations 1, 2, 3 and 4, i.e.,

$$V_S = C_{2aS}\left[B_a\left[C_{1aS}\left[V_{aS}\right]\right]\right] + C_{2bS}\left[B_b\left[C_{1bS}\left[V_{bS}\right]\right]\right] + C_{2cS}\left[V_{cS}\right] + V_{dS} \quad (5)$$

Reference to Figure 2, which shows the sources of fan face distortion during flight operation, results in the following equation for the fan face distortion velocity

$$V_F = C_{aF}\left[V_{aF}\right] + C_{bF}\left[V_{bF}\right] + V_{cF} + V_{dF} \quad (6)$$

where V_F is the total fan face distortion velocity in flight, V_{aF}, V_{bF}, V_{cF}, V_{dF} represent distortion velocities as they exist at their source and, as before, the symbol $C[\ ]$ represents an operator for the alterations caused by contraction.

Simplification of Equations 5 and 6 may be achieved by assuming that the self generated distortions V_{cF}, V_{dS} and V_{dF} are zero. In flight this assumption is true away from the boundary layer, at small angles of attack, and for engines mounted not too close to the fuselage (Blade Mounted Transducer data from a JT9D engine mounted inboard on a 747 verify these assumptions for this installation). Statically this assumption is true outside the boundary layer and then only if the inlet flow control screen does not generate distortions, a property that can be incorporated by proper design. This latter point is examined in the next subsection.

To further refine the expressions in 5 and 6, if it is noted that the fluctuating fan blade forces are the dominant noise generation mechanism, then only that component of the external velocity field that contributes to the fluctuating blade forces, i.e., the component of the distortion velocity perpendicular to the mean velocity, is of interest. In addition, this upwash velocity field can be considered to be made up of contributions from many distortions eddies of varying cross section and length. Only certain of these eddies contribute velocities that produce noise at blade passing frequency and its harmonics (although all unsteady components may produce broadband noise). The expressions 5 and 6 can be rewritten to reflect these considerations, i.e.,

$$N\{V_S\}_n = N\{C_{2aS}[B_a[C_{1aS}[V_{aS}]]] + C_{2bS}[B_b[C_{1bS}[V_{bS}]]] + C_{2cS}[V_{cS}]\}_n \tag{7}$$

$$N\{V_F\}_n = N\{C_{aF}[V_{aF}] + C_{bF}[V_{bF}]\}_n \tag{8}$$

where the subscript n denotes the upwash component of velocity and symbol $N\{\ \}$ represents the operation of selecting only those "eddies" that give rise to blade passage frequency tone noise and its harmonics; i.e., it is mathematically equivalent to filtering in wave number space.

Having evolved Equations 7 and 8, the next step is to establish criteria for a) simulation and b) minimization. Based on earlier discussions, these criteria are a) $N\{V_S\}_n = N\{V_F\}_n$ and b) $N\{V_S\}_n = 0$. Using these expressions, and Equations 7 and 8, there results:

$$N\left\{C_{2aS}\left[B_a\left[C_{1aS}\left[V_{aS}\right]\right]\right]+C_{2bS}\left[B_b\left[C_{1bS}\left[V_{bS}\right]\right]\right]+\right.$$

$$\left.C_{2cS}\left[V_{cS}\right]\right\}_n = \qquad (9)$$

simulation

$$N\left\{C_{aF}\left[V_{aF}\right]+C_{bF}\left[V_{bF}\right]\right\}_n \qquad (10)$$

suppression

In Equation 9, the filtering operation $N\{\ \}$ identifies the portion of the upwash velocity wave number spectrum (or eddy field) that contributes to tone noise. This subject has been addressed in the Phase I contract report, ref. (33). Models for the contraction and screen effects, denoted symbolically by $C[\ ]$ and $B[\ ]$ respectively, are discussed in this report.

A model for the atmospheric contribution to the external velocity is also defined in (33). The development of models for the distortion velocities generated by stand structure, ground planes, etc. and consideration of boundary layer and angle of attack effects are outside the scope of the current contract, but should be considered in future work.

Equations 9 and 10 can be used to illustrate the ICS design process. In both cases, the ICS designer can control the suppression characteristics of the screen, i.e. in essence he controls the operation $B[\ ]$ and can also control the location of the screen. The design procedure to be developed will be to define the screen characteristics and location in a manner that best satisfies Equations 9 or 10, subject to the constraints of minimizing ICS self-generated distortions and acoustic transmission losses across the screening.

5.2 Distortion Generation Constraint

The ICS should be designed to minimize or eliminate distortions inside and outside the boundary layer. Two possible design approaches for achieving this can be identified. Firstly, design the ICS without any significant distortion generator (such as struts and other inhomogeneities) in the structure. Alternatively, if such distortion generators exist then the distortions generated must be suppressed by a downstream device that does not have additional distortion generators or by the contraction that occurs downstream of the ICS.

5.3 Acoustic Transmission Constraint

Two approaches are available that account for the acoustic transmission characteristics of the inflow control screen. Either it can be required that the screen have negligible effect on the radiated sound field or it can be required that, in the event that there is an effect, that effect is to be defined. The second criterion is the less satisfactory on two counts. Firstly, the effect of a screen on the radiated field is, in general, a function of the source. Thus acoustic data gathered using different engines with the same inflow control screen could require different corrections and even data from the same engine at different operating conditions could require different corrections. Secondly, the necessity of having to correct acoustic data for inflow control screen effects increases the complexity of, and thus probability of error in the data reduction process.

An inflow control screen design that has as small effect as possible on the sound radiation field is thus the preferred result.

6.0 FAN FACE VELOCITY FIELD DEFINITION (PHASE II, TASK A)

6.1 Introduction

During the JNRP, (which was aimed at reducing the noise of a P&WA JT9D mounted on a Boeing 747), measurements were taken with pressure transducers surface mounted on the rotor blades. The same instrumented JT9D was operated at a test stand, with and without an inflow control screen, and in flight. It was the objective of this task to use these BMT data and hot film data to specify the turbulence velocity characteristics - intensity and length scale - at the fan face for each of these configurations over a range of engine speeds. These characteristics would then be used to provide an assessment of the preliminary ICS design system. In order to quantify the velocity field, it is necessary to define the response function relating the pressure sensed by a BMT to the unsteady upwash velocity field at the fan face. This response function was obtained by measuring the velocity fluctuations in the vicinity of the fan face with a hot film, and, by sampling of the BMT signal at each revolution, determining the corresponding pressure fluctuations at the blade surface. However, the once per revolution rate at which the BMT signal is sampled imposes an upper frequency limit on the empirical response function and so, beyond this frequency, a Sears response form is assumed. This response function can then be applied to the BMT data for the different conditions and speeds to determine a velocity spectrum, provided the BMT is responding to the velocity field. However, there is some question, at this time, as to whether the BMT signal is due to the inflow velocity field for all configurations and speeds. The possibility is discussed that, with the ICS and in flight, the BMT's may be responding to other stimuli such as the local noise field. Consequently application of the response function to the BMT data has been postponed pending resolution of this question.

6.2 Discussion of Blade Mounted Pressure Transducer Measurements

The BMT's with which the JT9D rotor was instrumented were thin film pressure sensors manufactured by Kulite Corporation. The frequency response of this sensor is greater than 20,000 Hz. The diameter of the sensor is .203 cms. while that of its diaphragm is .102 cms. The total sensor installation was less than .046 cms. above the blade surface, including a thin coating of RTV to provide protection from debris. A typical installation is shown in Figure 3. The transducers were located on the pressure surface approximately .318 cms. from the leading edge of the fan blade. Some were mounted in the tip region of the blade such that they were immersed in the nacelle boundary layer. Others were in the free stream region of the fan face. The leadwork was run along the pressure surface of the blade and attached to a telemetry transmitter in the nose cone of the engine. The data signals were transmitted to an antenna on the nacelle wall and subsequently recorded on magnetic tape. In order to relate this signal to specific circumferential locations,

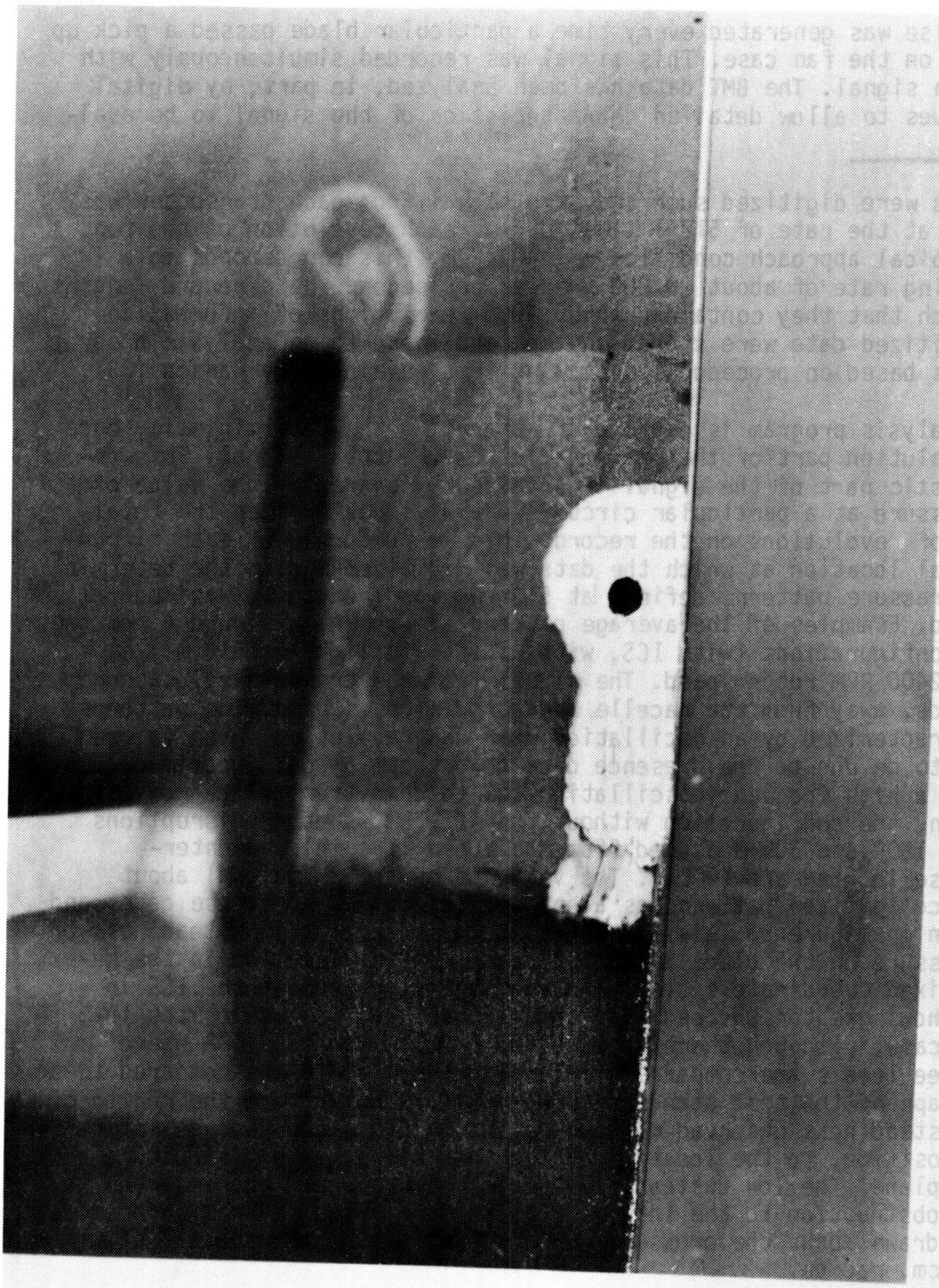

Figure 3 Blade mounted pressure transducer.

an impulse was generated every time a particular blade passed a pick up mounted on the fan case. This signal was recorded simultaneously with the data signal. The BMT data has been analyzed, in part, by digital techniques to allow detailed characteristics of the signal to be evaluated.

The data were digitized such that the signal from each transducer was sampled at the rate of 512+1 times during each revolution of the fan. At a typical approach condition of 2400 RPM, this corresponds to a digitizing rate of about 20,000 samples per second. Data record lengths were such that they contained about 1000 revolutions of information. The digitized data were stored on tape and input to an analysis program that was based on procedures and algorithms developed by Hanson (33).

This analysis program is capable of separating the deterministic, once per revolution part of the BMT signal from the total signal. This deterministic part of the signal is obtained by averaging the value of the pressure at a particular circumferential location over the total number of revolutions on the record. This is performed at each circumferential location at which the data was digitized and so the deterministic pressure pattern, defined at 512 angular locations, was constructed. Examples of the average pattern are shown in Figure 4 for the three configurations (with ICS, without ICS, inflight at 610 m.) at around 2400 RPM rotor speed. The signal from the transducer located on the blade, away from the nacelle boundary layer is used. The patterns are characterized by an oscillation over one revolution which is believed to be due to the presence of a downstream pylon. Superimposed on this is a high frequency oscillation due to downstream blade rows. In addition, the configuration without the ICS, shows other disruptions between 180° and 30° measured from the top of the inlet counterclockwise looking aft (°CCA). The variance of the BMT signal about this nacelle fixed pattern has also been determined for these cases and is shown in Figure 5. This quantity is a measure of the unsteadiness of the pressure on the blade at each circumferential location in the nacelle fixed coordinate system. The configuration without the ICS in place shows greater unsteadiness than either the ICS case or the inflight case, although there is a region from 10° to 120° CCA where all three levels are comparable. When Figures 4 and 5 are compared to a photograph of the test stand (Figure 6), it is noted that the region of high unsteadiness observed without an ICS in place corresponds in angular position, to the location of the test stand support structure and ground plane. The low unsteadiness region occurs where there is the lowest obstruction to the inflow. From these figures several inferences may be drawn about the pressure field sensed by the transducers at 107.75 cm. radius.

- Without an ICS in place the unsteady pressure field is dominated between 120° and 10° CCA by stand/ground generated distortions.

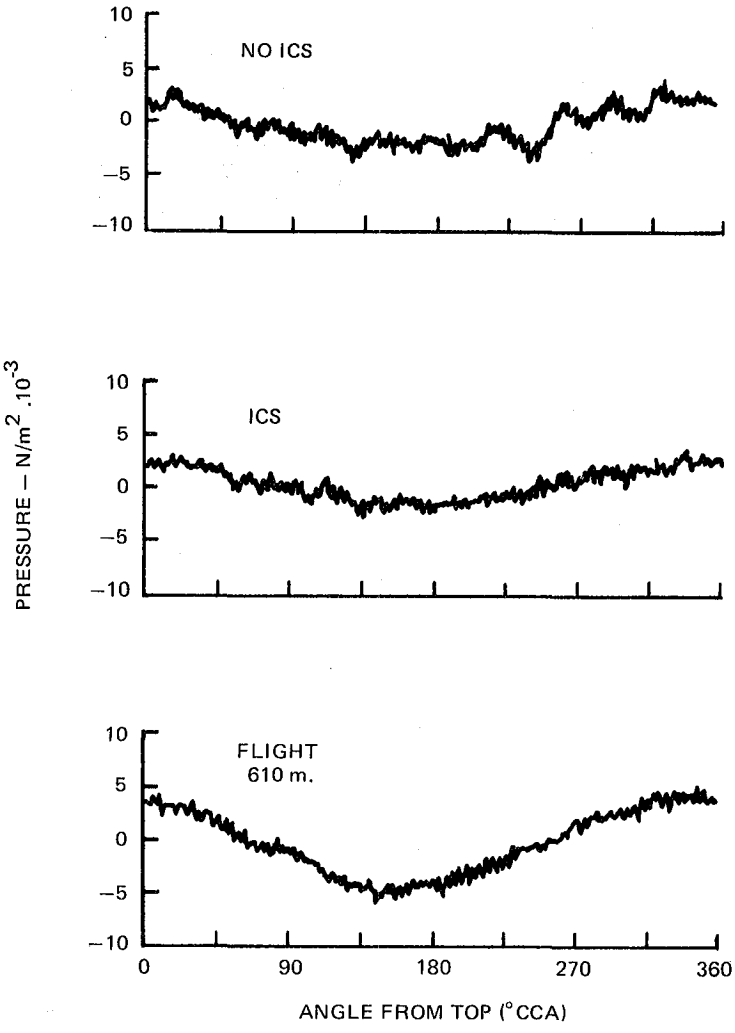

Figure 4 The deterministic part of the BMT pressure signal. Engine speed: 2400 rpm BMT radius: 107.95 cm.

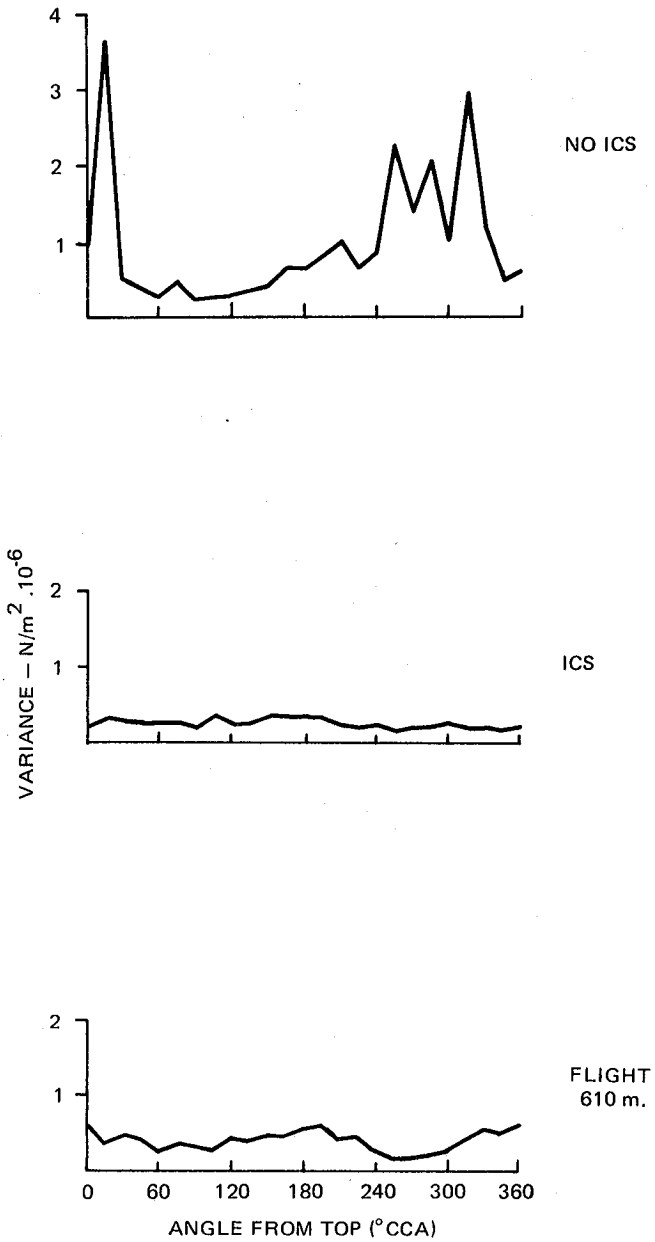

Figure 5 The variance of the BMT pressure signal. Engine speed: 2400 rpm. BMT radius: 107.95 cm.

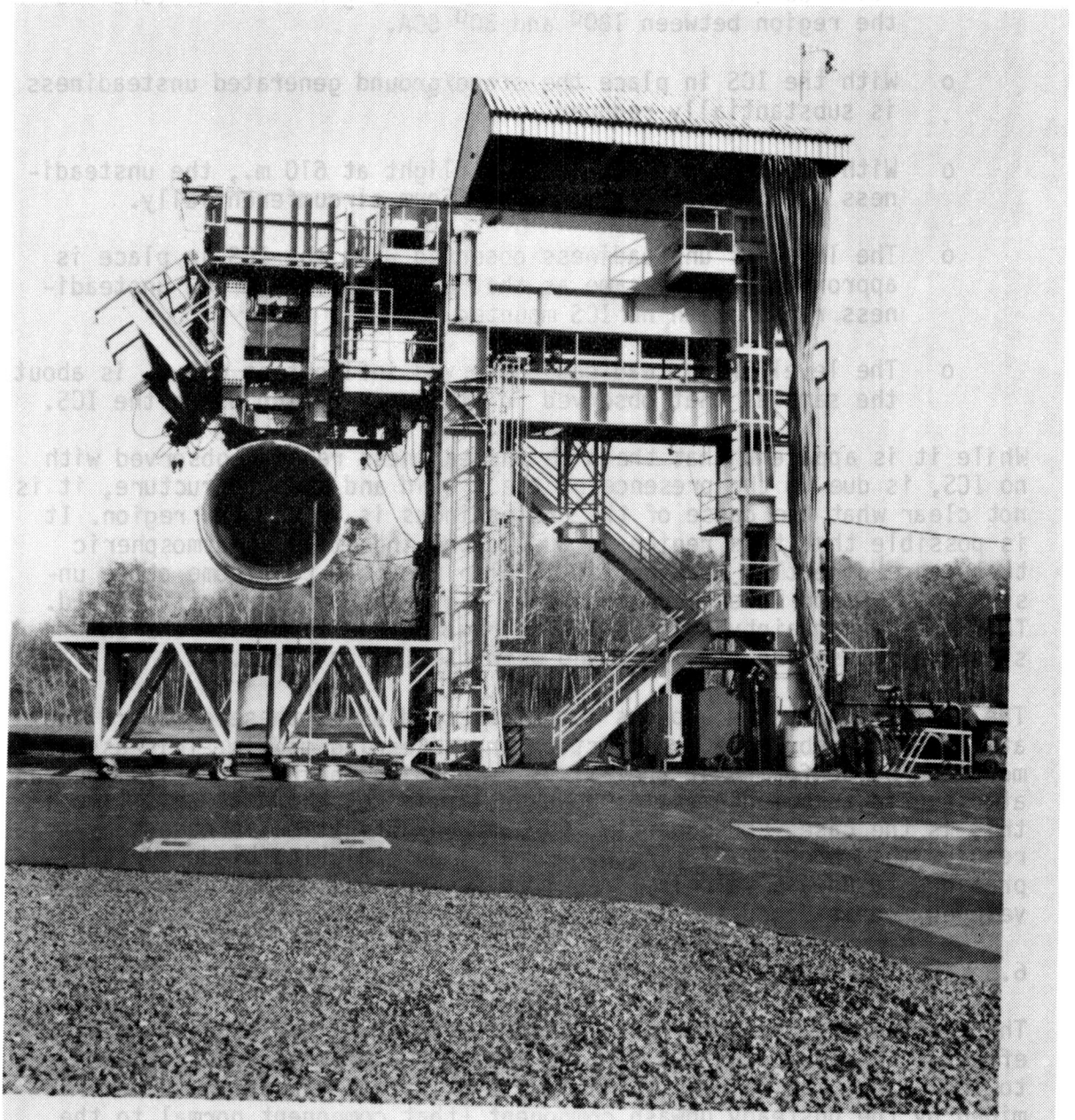

Figure 6 JNRP test stand.

- Without an ICS in place the deterministic pressure field contains contributions from stand/ground generated distortions in the region between 180^{o} and 30^{o} CCA.

- With the ICS in place the stand/ground generated unsteadiness is substantially reduced.

- With the ICS in place, and in flight at 610 m., the unsteadiness level is approximately uniform circumferentially.

- The level of unsteadiness observed with the ICS in place is approximately the same as that observed in the low unsteadiness region with no ICS mounted.

- The level of unsteadiness observed inflight at 610 m. is about the same as that observed in static operation using the ICS.

While it is apparent that the high unsteadiness region, observed with no ICS, is due to the presence of the ground and stand structure, it is not clear what the cause of the unsteadiness is in the low region. It is possible that this region is due to the ingestion of atmospheric turbulence directly, however, it is also possible that some other unsteadiness floor is encountered here; e.g., the local acoustic field. This same uncertainty exists also as regards the source of the unsteadiness observed in flight and with the ICS in place.

The ICS design system aspects to be assessed using these data are the atmospheric turbulence, contraction and screening models. This assessment can be performed if the BMT is responding to the directly ingested atmospheric turbulence field. However, it is not known at this time if this is the case. Consequently, further investigation is necessary to resolve this problem. The response function (relating blade surface pressure to upwash velocity) required for this assessment has been developed and is discussed in the following section.

6.3 The BMT Response Function

The fluctuating pressure on the blade surface, in the absence of other effects, is due to the fluctuating angle of attack of the flow incident to the blade. The nature of this angle of attack variation is determined by the unsteady upwash component (that component normal to the mean velocity vector) of the incident velocity field. The BMT response function, $T(\omega)$ is the ratio of the power spectral densities of the BMT pressure signal, $P(\omega)$, and the upwash velocity, $F_n(\omega)$, producing it; i.e.,

$$T_{(\omega)} = \frac{P_{(\omega)}}{F_{n(\omega)}} \qquad (11)$$

The power spectral density of the upwash velocity signal is found from the hot film measurements made during the JNRP. The hot film measurements, made with no ICS in place, were taken in a region where the BMT's were responding to the inflow unsteadiness generated by the ground and/or stand structure and so an estimate of the BMT response function using these measurements can be made.

The hot films were used to measure the streamwise and circumferential components of the unsteady inflow field at a station a short distance upstream of the fan. The films were mounted on a probe in the inlet. The installation is shown in Figure 7. Some films lay within the nacelle boundary layer and others were in the free stream. From the velocity measurements, the power spectral densities of the streamwise and circumferential velocity components, $F_1(\omega)$ and $F_2(\omega)$ respectively, were found. Using the relationships between the various velocity components, shown in Figure 8, the expression for the power spectral density of the upwash velocity component, $F_n(\omega)$, was determined in terms of the power spectral densities, $F_1(\omega)$ and $F_2(\omega)$ and the cross spectral density $F_{12}(\omega)$ of the streamwise and circumferential velocity components. The derivation of this expression, Equation 12, is given in Appendix A.

$$F_n(\omega) = F_1(\omega)\cos^2\gamma + F_2(\omega)\sin^2\gamma - Re\left(F_{12}(\omega)\right)\sin 2\gamma \quad (12)$$

For the computation of the upwash velocity spectrum, it has been assumed that the cross spectral term is negligible. Support for this contention is provided by a typical coherence plot shown in Figure 9 and an order of magnitude analysis described in Appendix A. The coherence is defined as

$$\frac{|F_{12}(\omega)|^2}{F_1(\omega)F_2(\omega)}$$

With this assumption Equation (12) becomes

$$F_n(\omega) = F_1(\omega)\cos^2\gamma + F_2(\omega)\sin^2\gamma \quad (13)$$

The corresponding blade pressure power spectral density was obtained from BMT's located at roughly the same radius as the hot films. Since it was not possible to use simultaneous hot film and BMT measurements because of the contamination of the BMT data by the wake of the hot film probe, the BMT measurements were taken with this probe removed. The ambient conditions under which the two sets (hot film and BMT) of measurements were taken were different. However, data taken from the same BMT under different ambient conditions, without an ICS, indicate

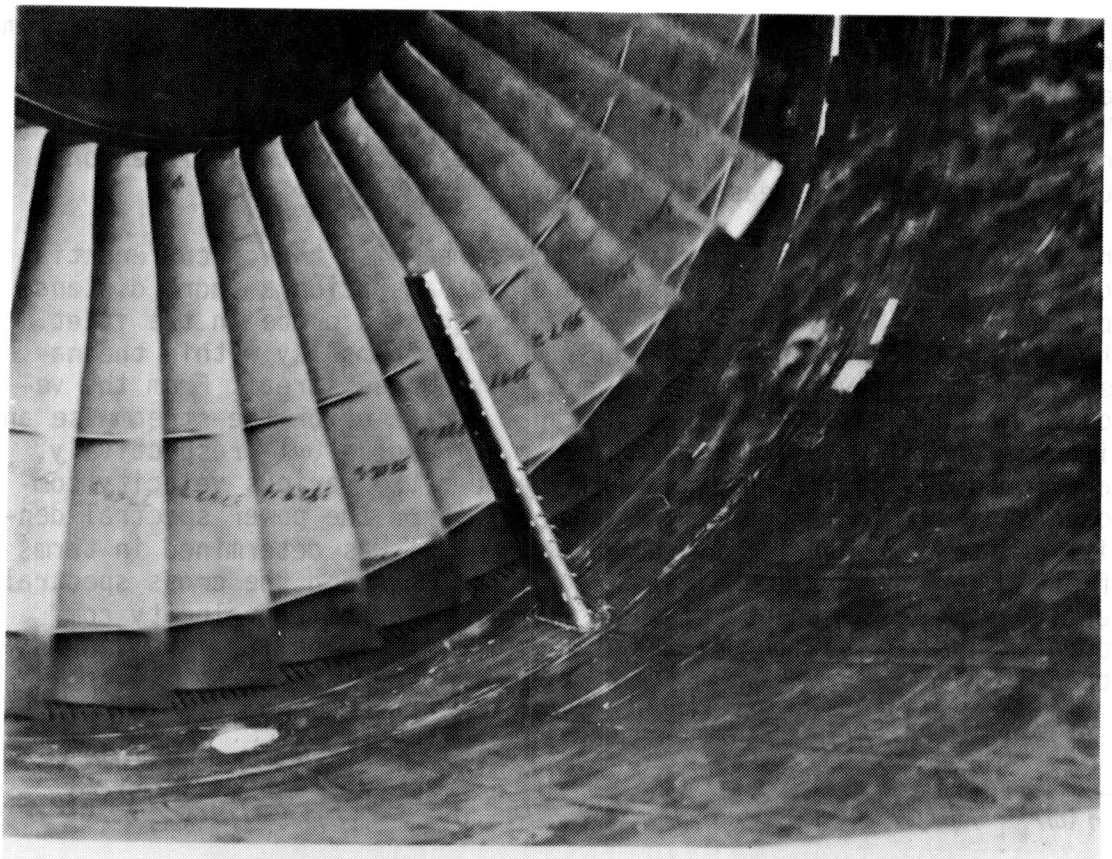

Figure 7 Hot film probe in JT9D inlet.

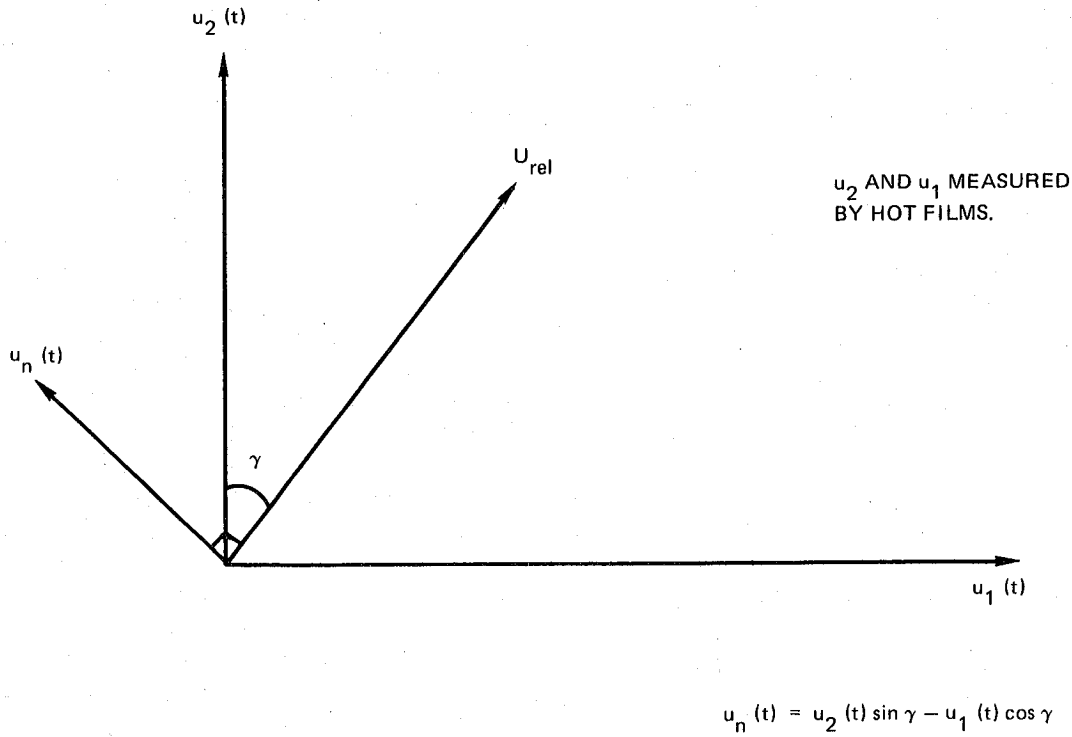

Figure 8 The relationship between the upwash velocity and the measured velocity components.

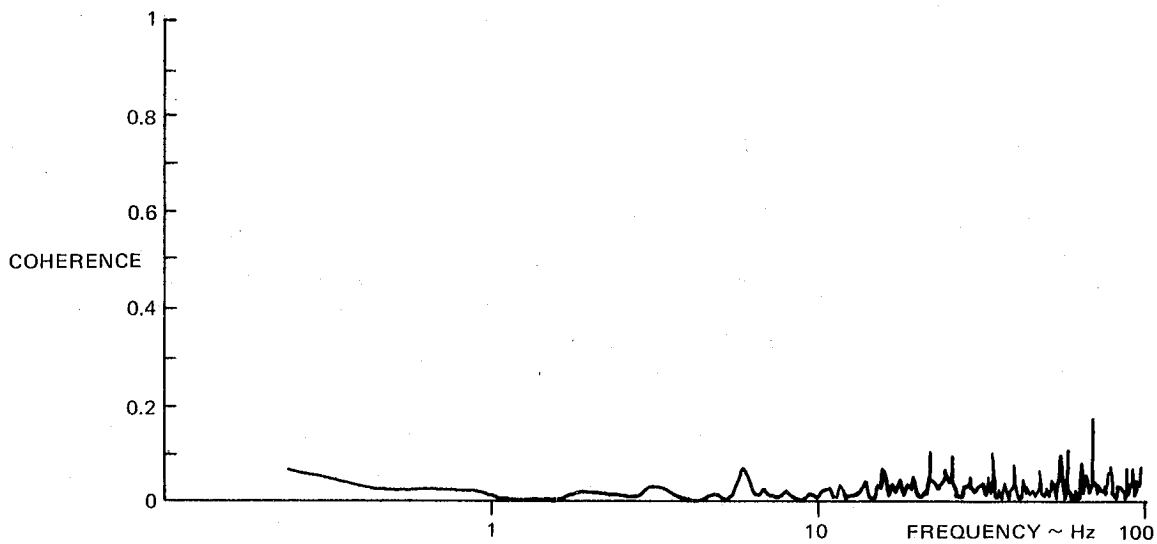

Figure 9 The coherence between the streamwise and circumferential unsteady velocity components.

that the inflow fields are substantially the same. This data is shown in Figure 10. The plots are of the circumferential variation in the pressure signal variance (a measure of the unsteadiness of the inflow) at two different times. Thus, it may be assumed that the film data was gathered under substantially the same inflow conditions as the BMT data, even though the measurements were not taken simultaneously.

Now the BMT pressure data may be viewed in the θ , t plane, where the pressure at the BMT is a function of the circumferential location and time. As shown in Figure 11 the BMT measures the pressure in this plane along lines determined by the velocity of the BMT relative to the mean inflow velocity. The dimension is related to an axial coordinate fixed with respect to the inflow by the mean inflow velocity. As can be seen from Figure 11, only once per revolution does the angular location of the BMT correspond to the angular location of the hot film. Further, it is necessary to define the temporal behavior of the pressure signal at that angular location in order to compute the BMT power spectral density required for Equation 11. Therefore, to determine the temporal behavior of the BMT signal due to the flow that passed in the vicinity of the hot film probe, the pressure signal must be sampled at this angle (202° CCA), during each revolution (Figure 12). At an approach fan speed of 2400 RPM, the sampling rate is about 40 samples per second, which provides a data point every .025 seconds. Consequently, a reliable estimate of the pressure power spectral density is available only to about 20 Hz. To obtain an estimate of the pressure power spectral density beyond 20 Hz it was assumed that the blade had a Sears response.

This assumption leads to the following form for the response function,

$$T(\omega) = \frac{P(\omega)}{F_n(\omega)} \qquad f < 20\ Hz$$

$$T(\omega) \propto |S(\omega)|^2 \qquad f > 20\ Hz \tag{14}$$

where $S(\omega)$ is Sears' function.

The response function computation has been performed for two BMT's located at 107.95 cm. radius on two blades. The engine condition was about 2400 RPM fan speed and with no ICS. The response functions are shown in Figure 13. At the condition for which they were calculated there were strong indications that the BMT's were responding to the inflow field, so that the calculations are valid.

The reason for the difference in the two curves is unknown. Conceptually, if both blades, transducers and mountings are geometrically similar, both should give the same response function. Differences may be due to differences in the way the transducers are mounted or to slight geometric differences between them.

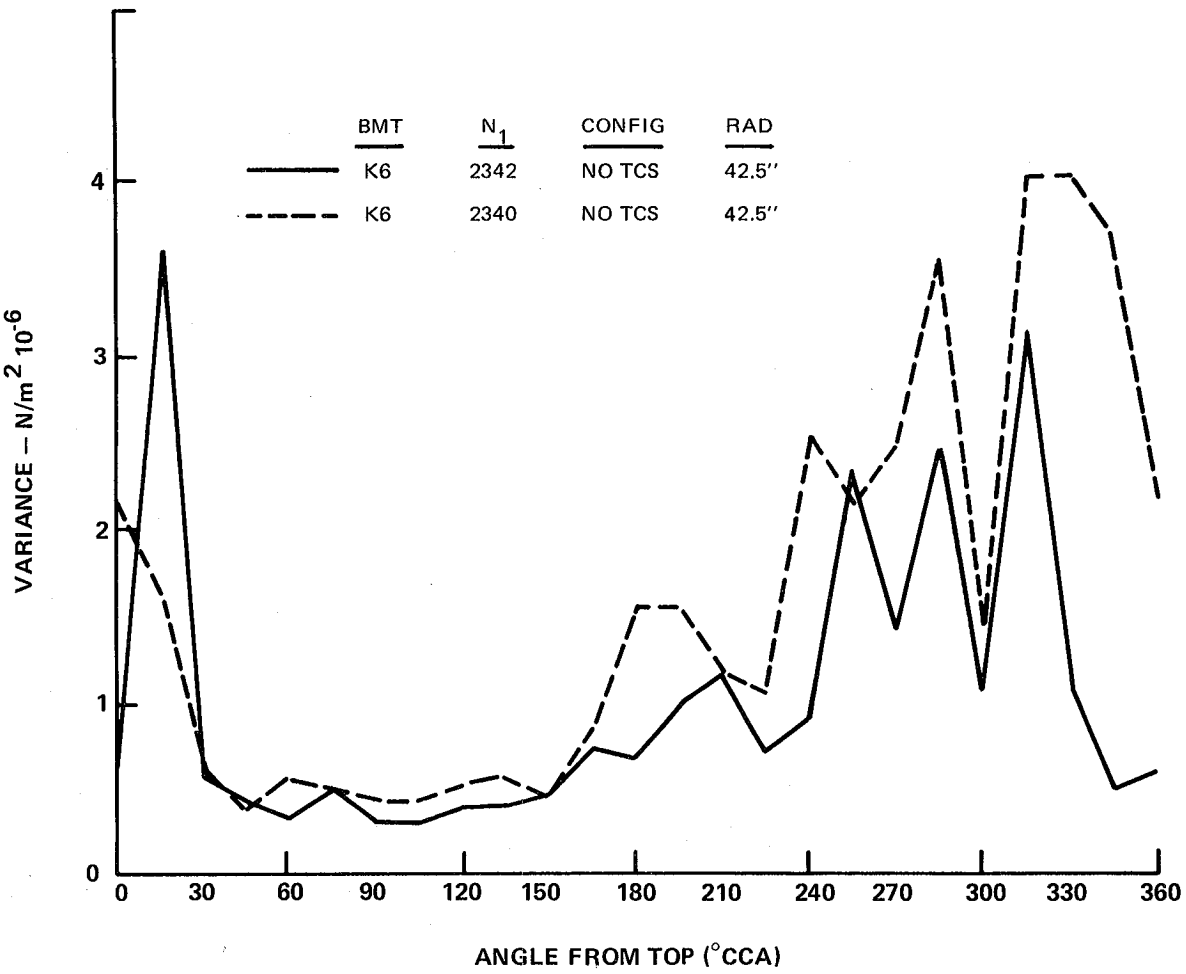

Figure 10 The variance of the BMT pressure signal at different times.

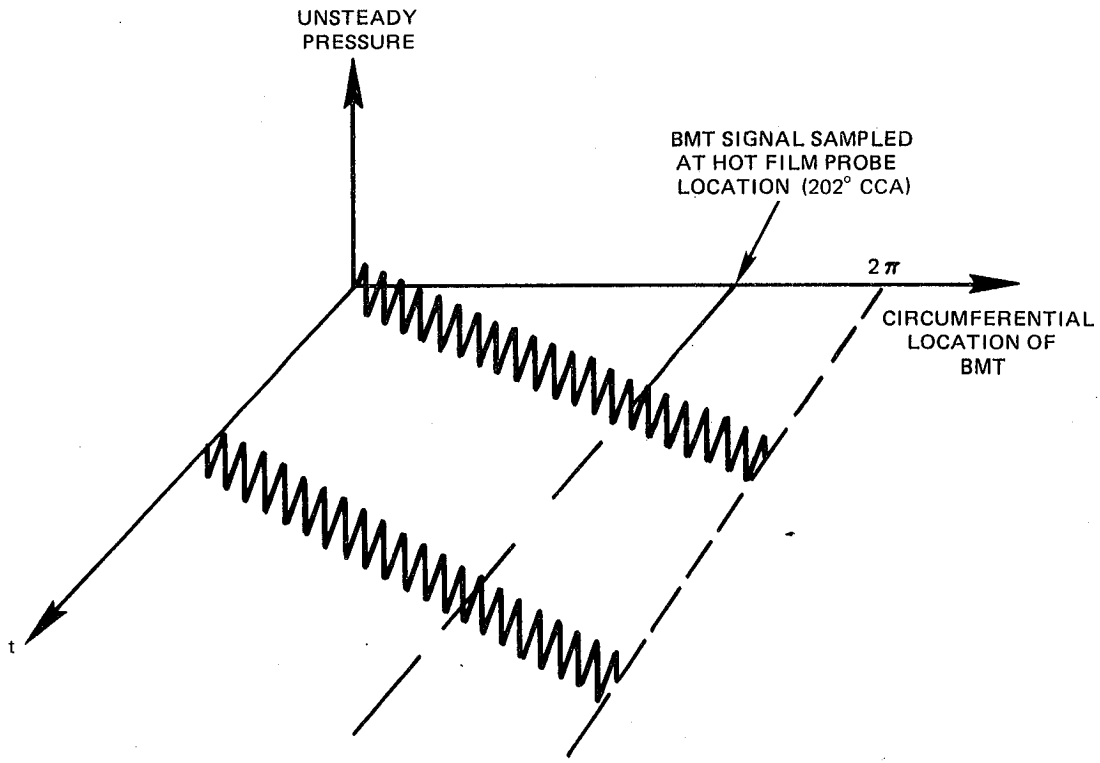

Figure 11 The sampling of the BMT pressure signal.

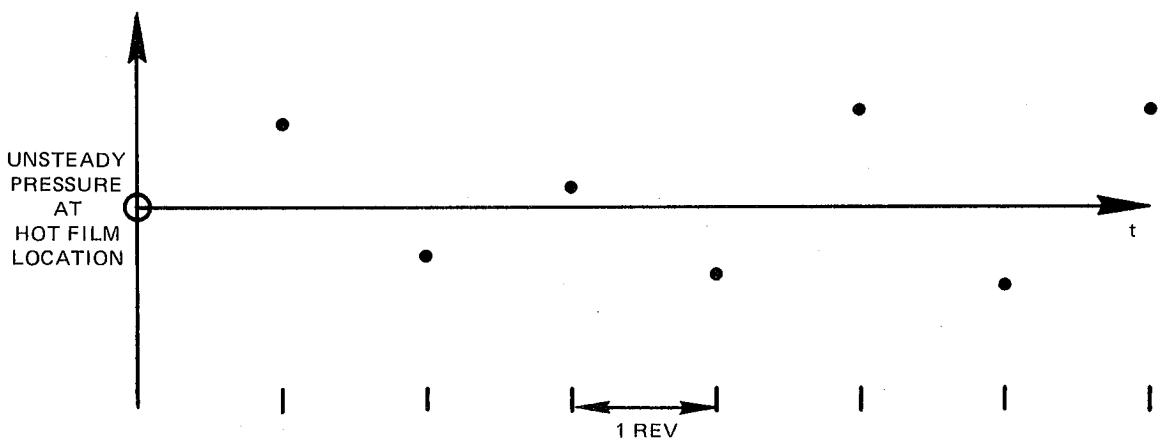

Figure 12 The pressure-time history at the hot film location.

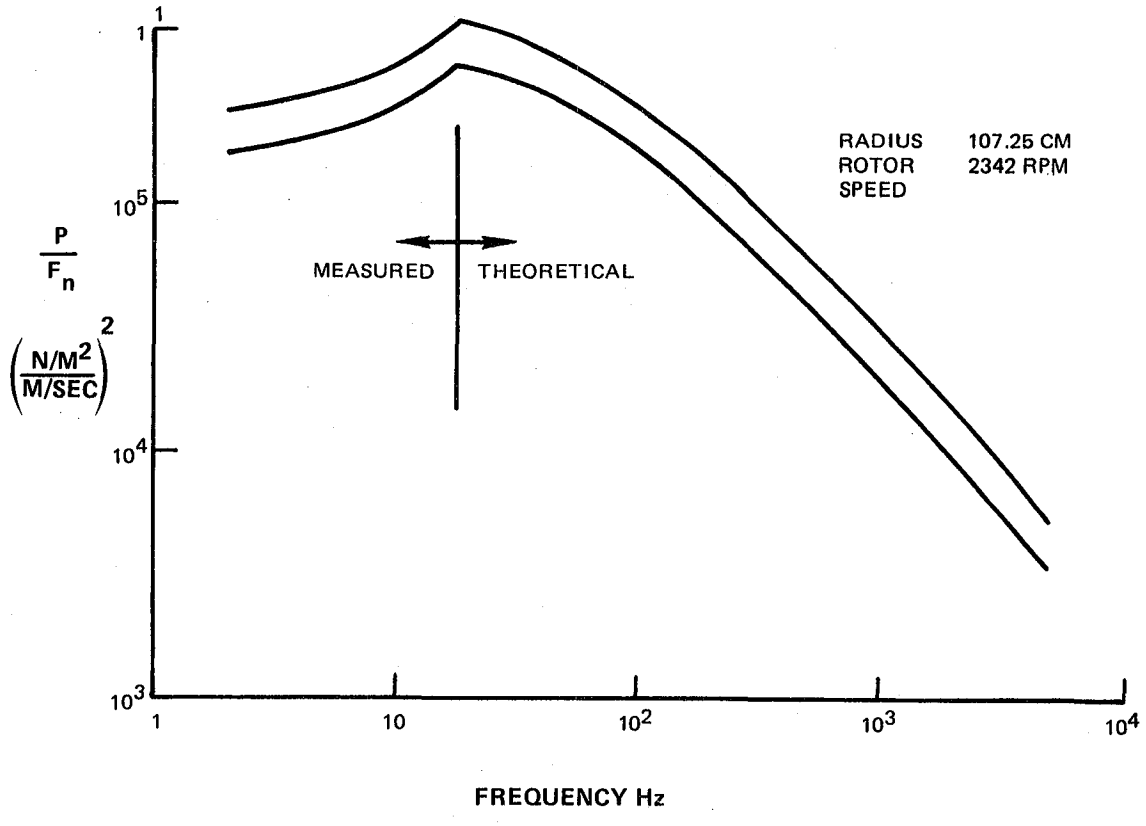

Figure 13 Composite response functions for two BMT's.

The application of these response functions to the BMT data obtained in flight and with the ICS in place has been deferred until the questions discussed earlier, concerned with determining whether the BMT signal is due to inflow velocity perturbations or some other cause, have been resolved.

7.0 THE EFFECT OF A FLOW CONTRACTION ON CONVERTED TURBULENCE (Phase II, Task C)

7.1 Introduction

The flow field into an engine is neither uniform nor steady. The unsteadiness may be considered to have two parts: (i) that part which relies upon the engine flow field for its existence and (ii) that part which does not. Included in the first category are such disturbances as ground or other surface associated vortices, engine induced wakes and the nacelle boundary layer. The second category consists of disturbances of the atmosphere due to the shear of the earth's boundary layer and buoyancy forces. These disturbances are referred to as atmospheric turbulence and its characteristics depend on such factors as terrain, altitude and temperature distribution. It is not isotropic. However, it tends to become more so as altitude increases, i.e., more of the turbulence spectrum has an isotropic form. The atmospheric turbulence phenomenon and representations of it are discussed in detail in the Phase I Report of this contract (34). The effect of the flow contraction on this atmospheric turbulence as it is convected into the engine is discussed in this section.

7.2 Background

The effect of a contracting flow on a turbulent field became of interest when it was observed that unsteadiness in wind tunnel working sections was significantly reduced by an upstream contraction. Prandtl (16) analyzed the phenomenon using very simple models that nevertheless provided a description, in terms of velocity changes, that corresponded well, qualitatively, with subsequent more complicated models. He showed that transverse velocity perturbations are amplified by the contraction while the streamwise component is attenuated. Taylor (34) in a more soundly based analysis showed that the problem could be linearized provided that turbulent inertial and viscous forces could be neglected. The consequence of his linearization is that the relationship between the pre and post contraction vorticity is determined by the change in the relative position of the fluid particles and is thus given by Cauchy's equation (36). Taylor's linearization constrains the rapidity of the flow contraction for a given initial turbulence field. Taylor solved the problem for particular convected velocity fields. Subsequently Ribner and Tucker (37) and Batchelor and Proudman (38) using Taylor's linearization and a Fourier representation of the turbulent velocity field solved the problem for arbitrary homogeneous convected velocity fields and contractions. Both sets of authors investigated isotropic initial turbulence convected through an axisymmetric contraction. Batchelor and Proudman showed that the mean square velocity relationships were independent of the initial isotropic spectrum. Ribner and Tucker determined expressions for certain post contraction one dimensional spectra, having assumed that the initial form was of the Dryden type. Pearson (39) linearized the problem by retaining the vis-

cous decay term, and neglecting the turbulence inertial effects. He examines, in particular, the effect of an axisymmetric contraction on weak isotropic turbulence and shows that as the contraction ratio tends to infinity the suppression of the streamwise pertubation velocities is accelerated and the amplification of the transverse components is finally balanced by viscous decay. In general, however, the total turbulent energy for a uniform irrotational distortion is found to increase without limit. These two linearizations of the Navier Stokes equations neglect turbulent inertial forces, with the result that the "return to isotropy" tendency observed experimentally is not modelled.

The attempt by Ribner and Tucker to provide experimental verification of the theory by using previously acquired data was not successful, due in part, to questions of data validity, and, in part, to violation of linearization assumptions. Subsequent comparisons by Uberoi and Hussein and Ramjee (40,41) also fLoundered on this point. In addition, there was some possibility of acoustic contamination in Uberoi's data. However, both concluded that the theory was most in agreement with measurement at low contraction ratios. They observed that the linear theory, beyond a certain contraction ratio, over predicts both the increase in transverse velocity perturbations and the attenuation of the streamwise component. This observation suggests that turbulence inertial effects are important in this region. It is significant, as Ribner and Tucker note, that the measurements themselves are inconsistent, indicating the dependence of the phenomenon on turbulence and contraction characteristics and also the difficulty of making uncontaminated measurements.

Townsend (42) also made detailed measurements of turbulence convected through a small contraction (4:1) and concluded that, for small strains, the structure of the energy containing "eddies" is similar to that produced by instantaneous strain. He further detected, at larger contraction ratios, an equilibrum condition at which the turbulence mean square velocity components are equal, though still changing. Tucker and Reynolds (43) disagreed that this equilibrium condition existed at the strain that Townsend had determined and further maintained that the total turbulent kinetic energy was reasonably predicted by the linear theory if it was corrected for viscous decay. However, they admitted that individual component changes were not satisfactorily predicted. Both sets of measurements indicated an initially rapid return to isotropy after the distortion has ceased.

The measurements to date have been made in flow contractions of velocity ratio that is small compared to that encountered in static engine operation. The details of these flows have not been well predicted by the linear theory which is supposedly valid only for the physically unrealizable instantaneous contraction.

Based on this review, it was concluded that there is no contraction model that has been developed that can be directly applied to the design of inflow control structure.

It is in part the purpose of the contract to develop such a model by building on existing analytical theories and providing empirical corrections to these theories. The empirical corrections will be derived by obtaining data on the effects of contraction on turbulence and mean flow distortion characteristics for contraction ratios and contraction rates that are more representative of those that result during static testing of engines. Since the effects of contraction will be based on existing models, a discussion of their underlying theory will be considered in the following sections.

7.3 Theory

The Navier-Stokes equations provide a suitable starting point for the discussion of the problem. Lamb (36) has shown that they may be written in terms of vorticity of the flow for an incompressible, constant viscosity fluid with no body forces.

$$\frac{D\Omega_i}{Dt} = \Omega_j \frac{\partial V_i}{\partial x_j} + \nu \nabla^2 \Omega_i \qquad (15)$$

If it is assumed furthermore, that the mean flow is irrotational, then the vorticity vector is solely due to the turbulent velocity fluctuations. Thus after expanding slightly, Equation 15 becomes

$$\frac{D\omega_i}{Dt} = \omega_j \frac{\partial U_i}{\partial x_j} + \omega_j \frac{\partial u_i}{\partial x_j} + \nu \nabla^2 \omega_i \qquad (16)$$

and the dynamics of the vorticity variation may be ascertained. Equation 16 states that the rate of change of the vorticity of a point moving in a fluid is determined by the sum of (i) the production of vorticity by the mean motion straining the turbulent "eddies", (ii) the transfer of vorticity amongst turbulent "eddies" by one "eddy" straining another and (iii) the diffusion of vorticity by viscosity. The rapid distortion assumption allows the two latter contributions to be ignored on the grounds that the flow is distorted so quickly that no vorticity is transferred or dissipated in the contraction time. It is this assumption that was invoked by Taylor, et al, to simplify and solve Equation 16.

The validity of the rapid distortion assumption must be assessed relative to the flow contractions experienced during engine operation both statically and in flight. An order of magnitude analysis of the terms in Equation 16, and following Ribner and Tucker is described in Appendix B. Application of this analysis to the engine contraction problem shows that under flight conditions the rapid distortion assumption is valid, whereas under static conditions, it is not.

Accordingly, use of results based on the simplified form of Equation 16 should be valid in flight, but questionable for static applications. As discussed above, the linearized theories will be used as the basis for our models, with empirical corrections used to account for the errors introduced by the neglect of the last two terms in Equation 16.

This simplified equation was solved in detail by both Ribner and Tucker and Batchelor and Proudman for an isotropic turbulence field convected through an axisymmetric contraction. Ribner and Tucker's treatment is discussed in the Phase 1 report. Batchelor's somewhat more elegant formulation produced the same results, namely that

$$\mu_1 = \frac{\overline{u_{1B}^2}}{\overline{u_{1A}^2}} = \frac{3}{4}\ell_1^{-2}\left\{\frac{1+\beta^2}{2\beta^3}\ln\frac{1+\beta}{1-\beta} - \beta^{-2}\right\}$$

$$\mu_2 = \frac{\overline{u_{2B}^2}}{\overline{u_{2A}^2}} = \frac{3}{4}\ell_1 + \frac{3}{4}\ell_1^{-2}\left\{\frac{\beta^{-2}}{2} - \frac{1-\beta^2}{4\beta^3}\ln\frac{1+\beta}{1-\beta}\right\}$$

where

$$\beta^2 = 1 - \ell_1^{-3} \qquad (17)$$

$$\frac{L_{11B}}{L_{11A}} = \frac{1}{\ell_1\mu_1}, \quad \frac{L_{22B}}{L_{22A}} = \frac{L_{33B}}{L_{33A}} = \frac{\sqrt{\ell_1}}{\mu_2}$$

$$\frac{L_{31B}}{L_{31A}} = \frac{L_{21B}}{L_{21A}} = \frac{\ell_1^2}{\mu_2},$$

The length scales shown above are derived in Appendix C. The subscripts refer to the velocity component and direction of the dimension. For instance, L_{13} is the length scale of the axial velocity component in one of the transverse directions. There are nine of such length scales in general associated with the three Cartesian coordinates and velocities. The above length scale ratios are true, within the assumptions of the linear theory, for any initial isotropic turbulence field. The length scale ratios not formulated above depend on the particular form of the spectrum tensor of the incoming turbulence and therefore cannot be generalized.

7.4 Eddy Model

Prandtl used simple "eddy" models to solve the contraction problem. He considered two types of flow elements; a steady axial velocity deficit, and an axially oriented vortex filament and their modification by an axisymmetric flow contraction. Considering the first distortion element, with reference to Figure 14 and applying Bernoulli's incompressible equation to two streamlines and assuming that before and after the contraction there are no transverse static pressure gradients, yields:

$$\left[{}_1U_A - {}_2U_A\right]\left[{}_1U_A + {}_2U_A\right] = \left[{}_1U_B - {}_2U_B\right]\left[{}_1U_B + {}_2U_B\right]$$

Now if

$${}_1U_A \Omega {}_2U_A \quad \text{AND} \quad {}_1U_B \Omega {}_2U_B \tag{18}$$

$$\therefore \quad \frac{{}_1U_B - {}_2U_B}{{}_1U_A - {}_2U_A} \Omega \frac{{}_1U_A}{{}_1U_B} = \frac{1}{\ell_1}$$

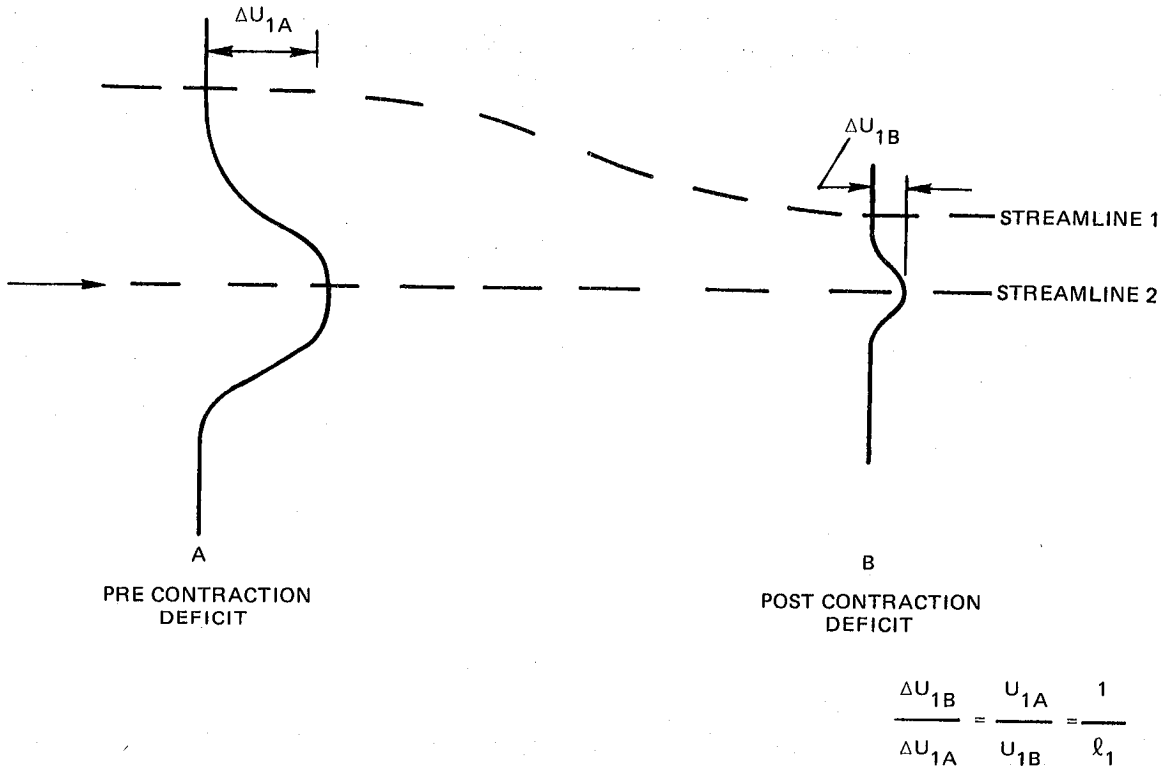

$$\frac{\Delta U_{1B}}{\Delta U_{1A}} = \frac{U_{1A}}{U_{1B}} = \frac{1}{\ell_1}$$

Figure 14 Contraction of a small steady axial velocity distortion.

Thus Prandtl determined that small axial distortions were attenuated according to the inverse of the flow contraction ratio. For the convection of the axially oriented vortex, again the convecting flow was assumed to be axial before and after the contraction. Conserving circulation around a circular path in a plane perpendicular to the convecting flow, (see Figure 15), yields

$$\oint_{CA} \underline{U_A} \cdot d\underline{s}_A = \oint_{CB} \underline{U_B} \cdot d\underline{s}_B$$

So that (19)

$$U_{\theta A}\, r_A = U_{\theta B}\, r_B$$

or

$$\frac{U_{\theta B}}{U_{\theta A}} = \sqrt{\ell_1}$$

Thus from this type of distortion element Prandtl deduced that transverse velocity components were amplified by the flow contraction according to the square root of the contraction ratio. Now if the turbulence field is considered to be made up of many eddies and if, furthermore, the unsteady velocities associated with this eddy field behave, through the contraction, in the same manner as a velocity field made up of many of Prandtl's elements, then an ensemble average over the upstream and downstream velocity fields, yields relationships between the mean square values of the perturbation velocity components.

$$\frac{(\overline{u_1^2})_B}{(\overline{u_1^2})_A} \quad \frac{1}{\ell_1^2}\,, \quad \frac{(\overline{u_2^2})_B}{(\overline{u_2^2})_A} \quad \frac{(\overline{u_3^2})_B}{(\overline{u_3^2})_A} = \ell_1 \qquad (20)$$

Furthermore an examination of the distortion of a cubical fluid element by an axisymmetric contraction where the field particle displacements are dominated by the mean flow gradients (Figure 16) produces estimates of the eddy length scale changes.

$$\frac{L_{1B}}{L_{1A}} = \ell_1\,, \quad \frac{L_{2B}}{L_{2A}} = \frac{L_{3B}}{L_{3A}} = \ell_1^{-1/2} \qquad (21)$$

These length scale ratios are considerably simpler than those derived from Taylor and Batchelor's work. Here, there is no dependence on the velocity component and the ratios are only functions of the direction denoted by the subscript. The length scale ratios then for all three velocity components in a given direction are the same.

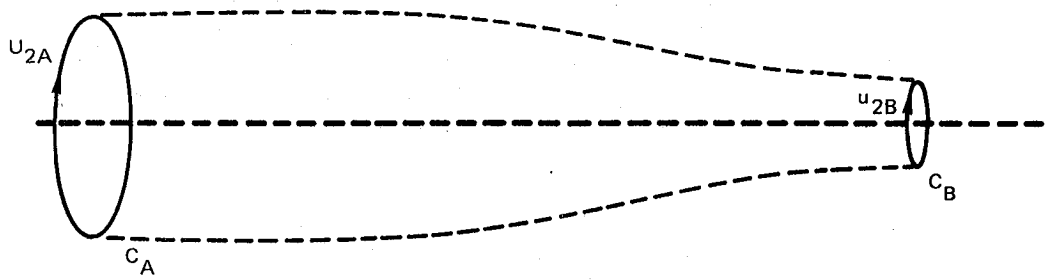

$$\frac{U_{2B}}{U_{2A}} = \frac{U_{1B}}{U_{1A}} = \ell_1$$

Figure 15 Contraction of a steady axial vortex.

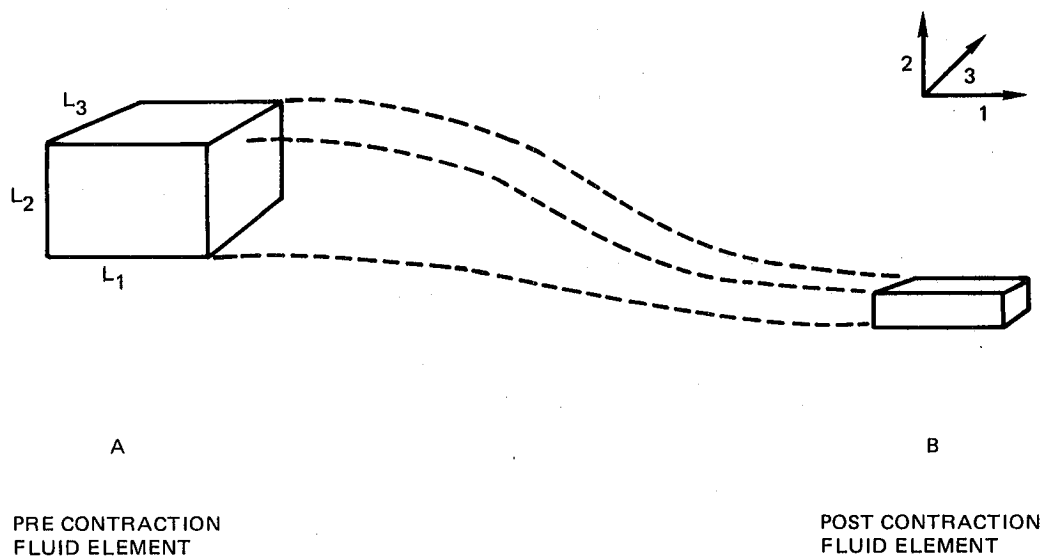

Figure 16 The axisymmetric contraction of a fluid element.

Expressions 20 and 21 describe the effect of an axisymmetric contraction on a turbulent field. In view of the absence of viscous decay effects on the distortions elements, together with the assumed absence of any interaction between these elements, this model can be considered to be an approximation of the general solution of Taylor's linearized problem, determined in Refs. 37, 38. A comparison of the two sets of results is shown in Figure 17. As can be seen the trends are similar for the mean square values of the velocity components, and for the larger contraction ratios. The corresponding predictions of the kinetic energy ratio across contraction are shown in Figure 18. The comparison of scale changes predicted by the two theories is shown in Figure 19. The dashed lines are the scale ratios given in Equation 21 while the solid lines are the ratios obtained from Batchelor and Proudman's results.

The predictions of the scale change in L_{11} are not in close agreement and this reflects the different upstream turbulence fields that were examined. The general significance of the integral length scales is somewhat obscure on a physical basis, they are however, a measure of the one dimensional spectral shapes. The one dimensional power spectral density $F_i(k_j)$ is the power spectral density of the ith velocity component as a function of the wavenumber component in the jth direction. This power spectral density is analogous to the Fourier decomposition of a particular velocity component in a periodic velocity field in a particular direction.

If in addition to the earlier assumptions it is required that the "eddies" be axially oriented, then the downstream one dimensional spectra are functions only of the corresponding upstream one dimensional spectra and the contraction characteristics. In this situation the energy in the wave number range Δk_{jA} about k_{jA} will be converted into energy in the range Δk_{jB}, see Figure 20. Now with the one dimensional spectra represented by $F_i(k_j)$

Then $$\Delta (\overline{u_i^2})_A \triangleq F_{iA}(k_{jA}) \Delta k_{jA}$$

But $$\Delta (\overline{u_i^2})_B \triangleq F_{iB}(k_{jB}) \Delta k_{jB}$$

Now $$\Delta (\overline{u_i^2})_B = \frac{1}{e_i^2} (\overline{u_i^2})_A$$

And $$\therefore F_{iB}(k_{jB}) = \frac{1}{e_i^2} F_{iA}(k_{jA}) \frac{\Delta k_{jA}}{\Delta k_{jB}} \qquad (22)$$

$$\frac{k_{jB}}{k_{jA}} = \frac{1}{e_j} \quad \therefore \quad \frac{k_{jA}}{k_{jB}} = e_j$$

$$\therefore F_{iB}(k_{jB}) = \frac{e_j}{e_i^2} F_{iA}(k_{jA})$$

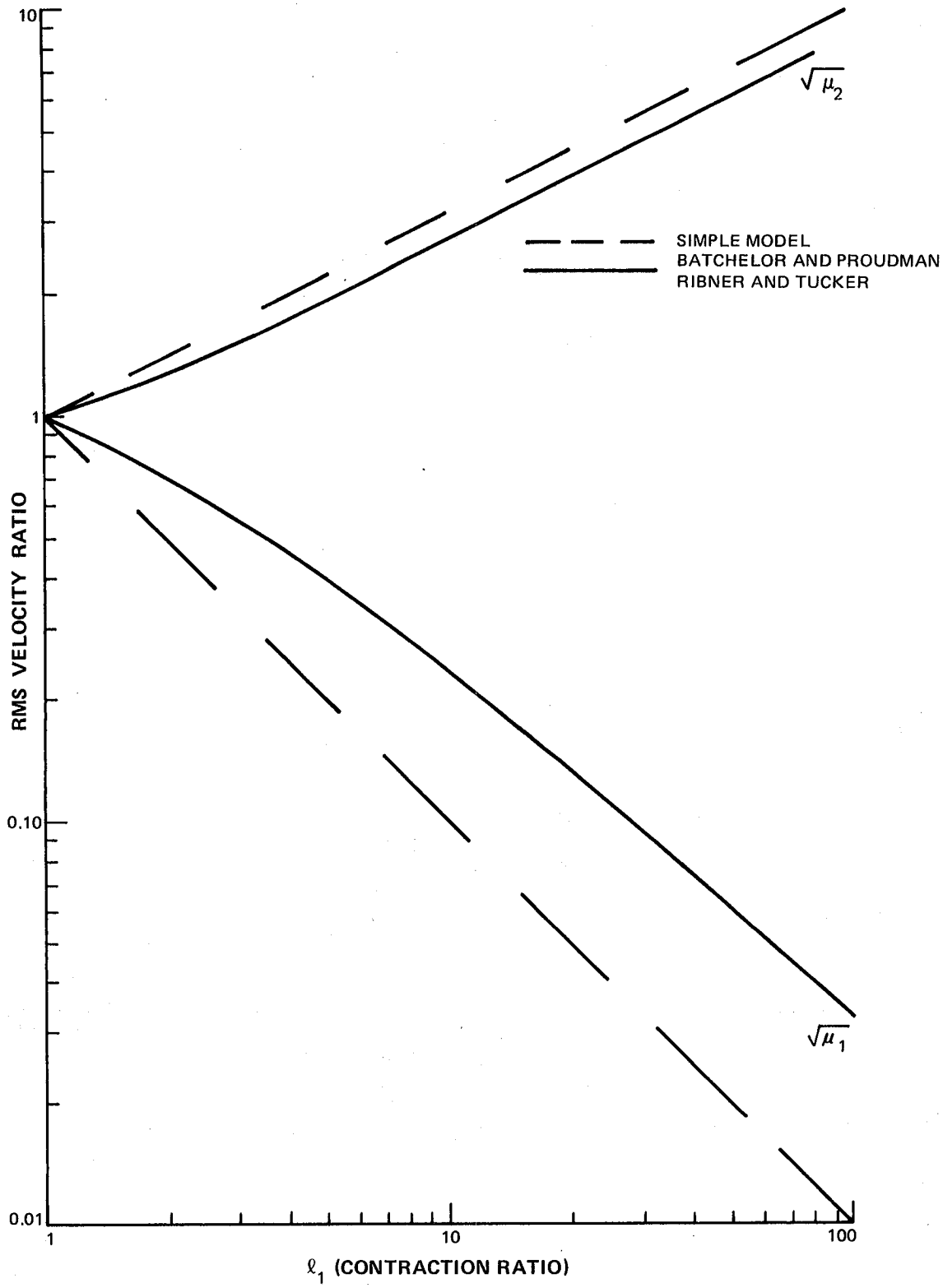

Figure 17 The effect of a contraction on the turbulent RMS velocity ratios.

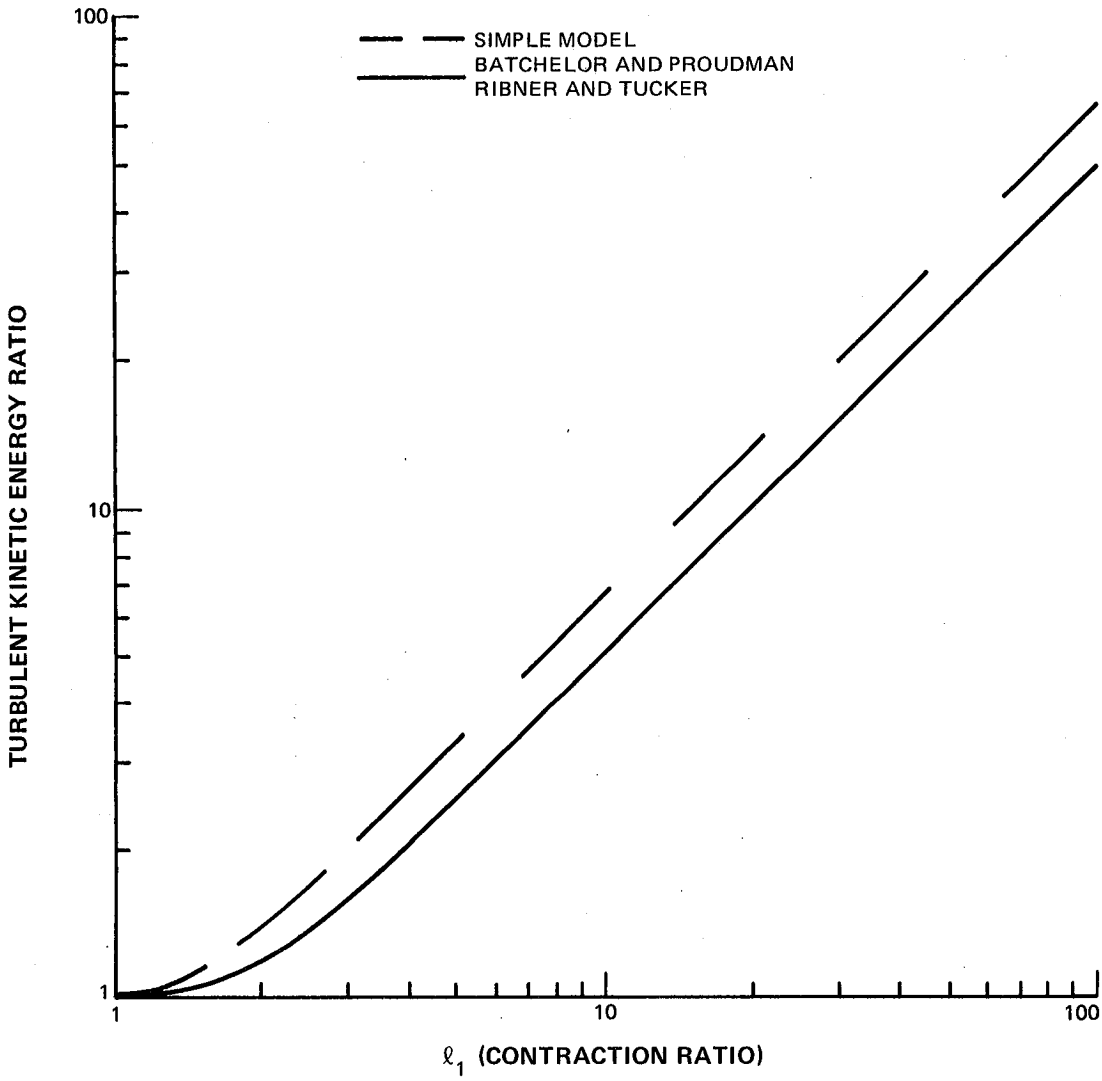

Figure 18 The turbulent kinetic energy ratio across a contraction.

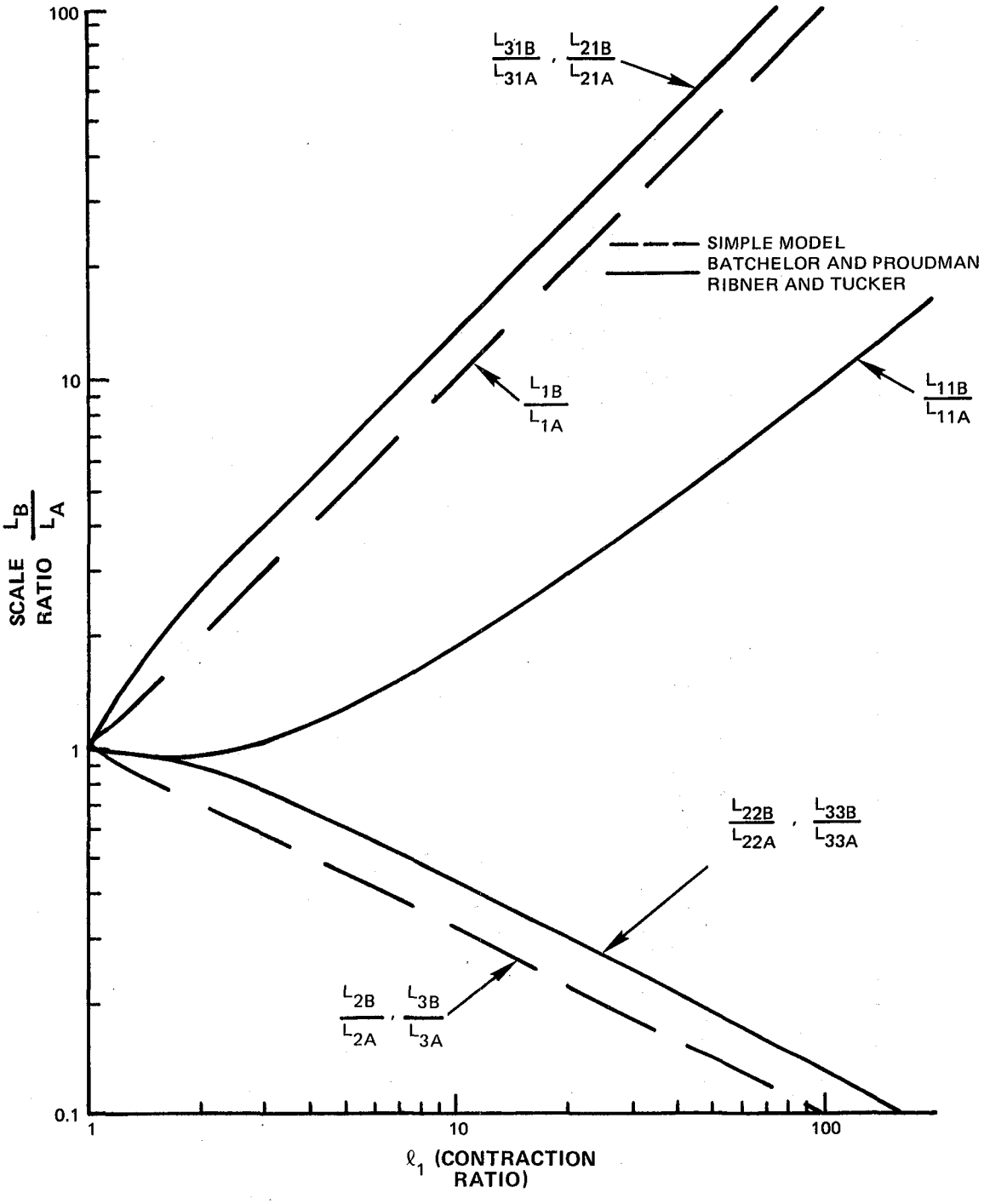

Figure 19 The effect of a contraction on the turbulent scale ratios.

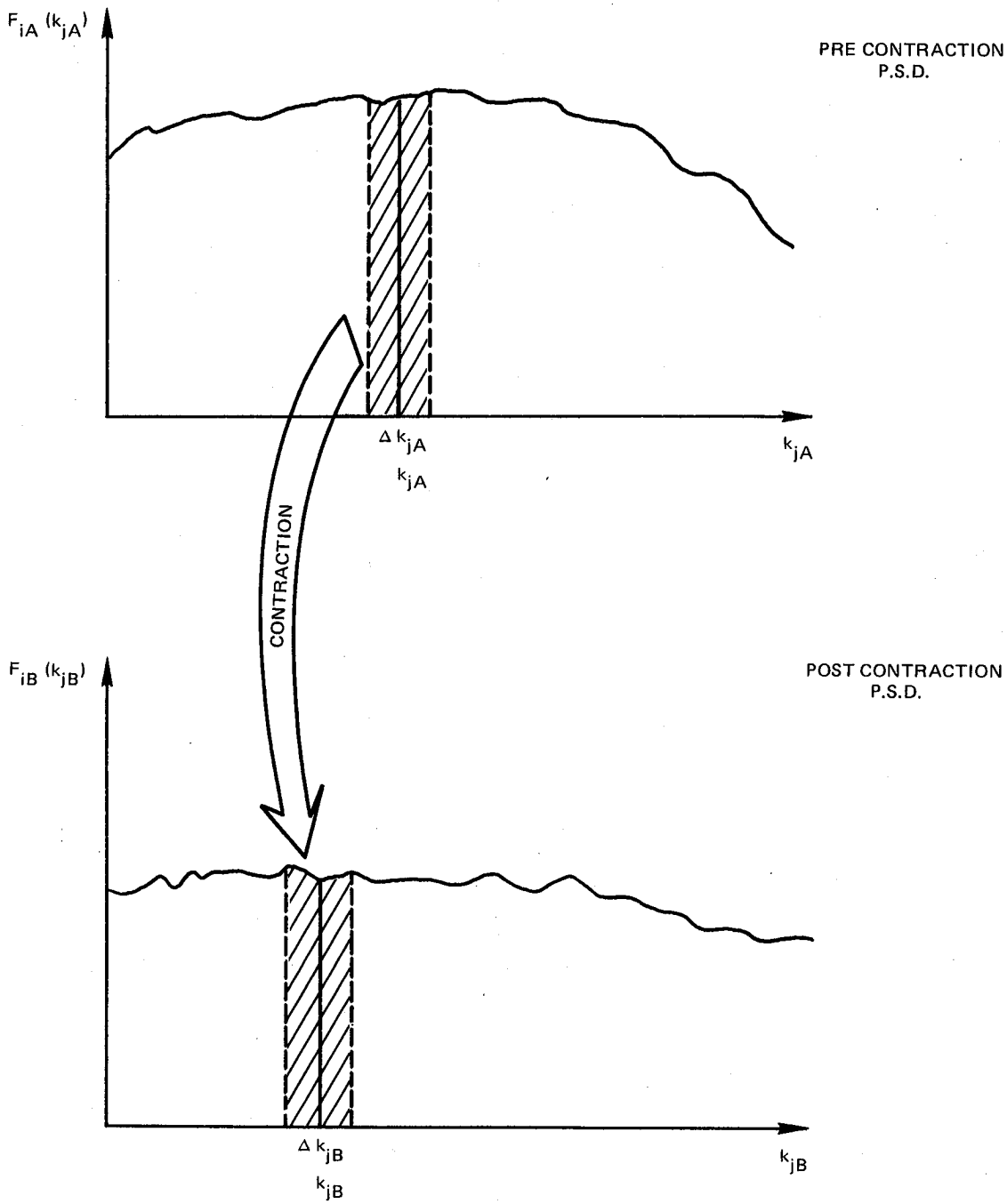

Figure 20 A simple model of the contraction effect on one dimensional PSD's.

Where $u_i = u_1, u_2, u_3$ are the Cartesian components of the unsteady velocity field and $k_j = k_1, k_2, k_3$ are the Cartesian wave number components.

Comparisons between two downstream spectra as predicted by Equation 22 and Ribner and Tucker are shown in Figures 21 and 22. In view of the discrepancy noted previously for the L_{11} integral length scale, the large difference in the corresponding spectra is not unexpected. However, there is close correspondence between the predictions of the transverse spectrum, again in accordance with the length scale comparisons.

The predictions using the eddy model are then close enough to those using the more rigorous theory to provide a basis for experimentation. The simplicity of the one dimensional spectral relationships recommends their use in the inflow control system design procedure. Figure 23 contains a summary of the eddy model results.

The linear theories account only for the distortion process and this proceeds, according to Uberol, et al, unrelieved by an turbulence inertial or viscous decay effects. Consequently the higher the contraction ratio, the more in error will be the linear theory.

7.5 Conclusions

I. Based on the discussions in the section, the simple theory of Prandtl, summarized in Figure 23, will be used as the basis for the models that account for contraction effects on turbulence. Tendencies toward isotropy, observed experimentally for small contraction ratios relative to the static case, will be incorporated empirically as necessary, by use of the test data from Task F of this contract.

II. The measurements of Uberoi, et al, indicate that the contraction process is characterized by:

- o A distortion of the turbulence field.
- o Amplification of the transverse turbulent velocity components.
- o Attenuation of the streamwise turbulent velocity components, at least, initially.
- o An equilibrium condition attained after a certain amount of contraction beyond which further distortion does not occur. This equilibrium condition is determined by the contraction rate variation through the contraction.
- o A rapid initial rate of return to isotropy followed by an asymptotic approach to that state. The initial return rate is determined by the distortion of the field.

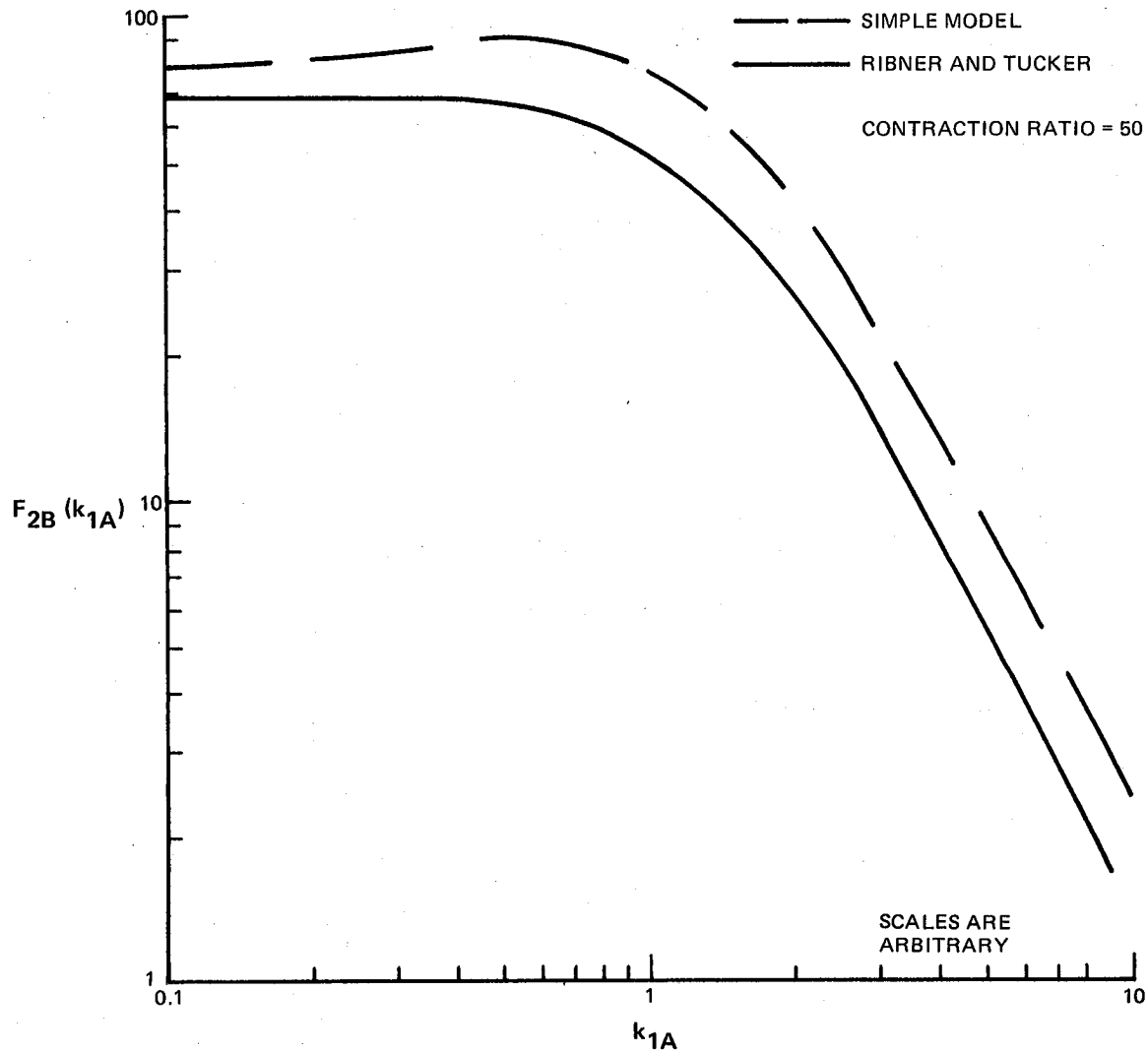

Figure 21 The one dimensional post contraction PSD of a transverse velocity component.

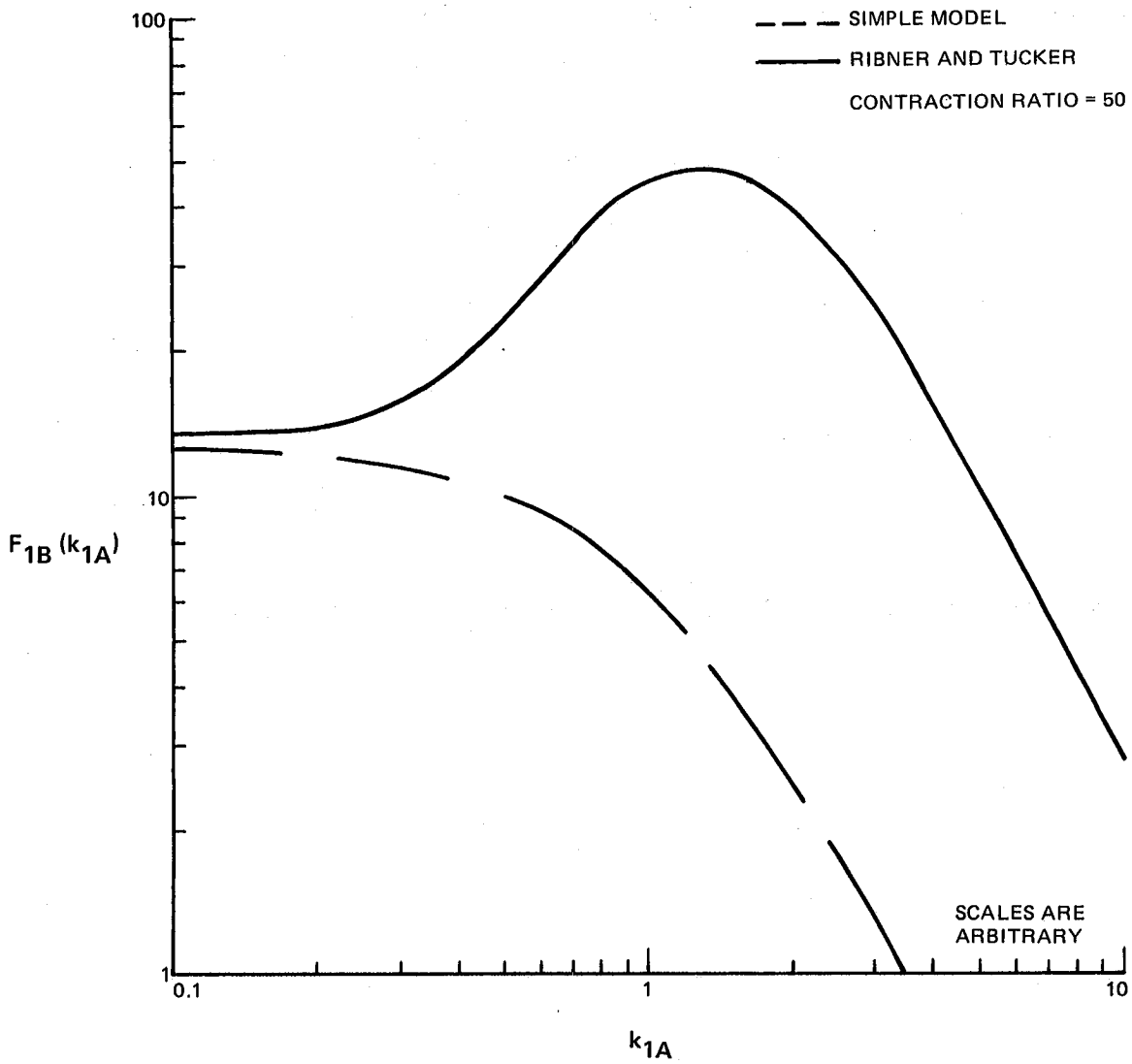

Figure 22 The one dimensional post contraction PSD of the streamwise velocity component.

- **TURBULENT KINETIC ENERGY RATIO** $\dfrac{(\overline{u_{ii}})_B}{(\overline{u_{ii}})_A} = 2\ell_1 + \dfrac{1}{\ell_1^2}$

- **COMPONENT MEAN SQUARE VELOCITY RATIOS** $\dfrac{(\overline{u_i^2})_B}{(\overline{u_i^2})_A} = \dfrac{1}{\ell_1^2}, \dfrac{(\overline{u_2^2})_B}{(\overline{u_2^2})_A} = \dfrac{(\overline{u_3^2})_B}{(\overline{u_3^2})_A} = \ell_1$

- **EDDY LENGTH SCALE RATIOS** $\dfrac{L_{1B}}{L_{1A}} = \ell_1 \ , \dfrac{L_{2B}}{L_{2A}} = \dfrac{L_{3B}}{L_{3A}} = \dfrac{1}{\sqrt{\ell_1}}$

- **POWER SPECTRAL DENSITY RATIOS** $F_{iB}(k_{jB}) = \dfrac{e_j^2}{e_i^2} F_{iA}(k_{jA})$

Figure 23 The eddy model for the contraction of turbulence.

III. The comparison of the rigorous and simple theories should be viewed with this in mind. The main points of the comparison are:

- o The predictions of the turbulent kinetic energy ratio across the contraction produced by both theories are in close agreement.

- o The predictions of the ratio of the RMS values of the individual transverse velocity components across the contraction produced by the two theories are in reasonably close agreement.

- o The predictions of the ratio of the RMS values of the streamwise velocity component across the contraction produced by the two theories are not in good agreement, although the trends with increasing contraction ratio are similar.

- o Correspondingly the predictions of integral length scales and one dimensional spectra of the transverse components of turbulent velocity produced by the two theories are in reasonably close agreement. But the predictions for these quantities for the streamwise component of turbulent velocity are not in good agreement except at low contraction ratios.

In general then, the more detailed the description of the phenomenon, the more divergence between the predictions of the simple and rigorous theory.

IV. The applicability of the linear theories to a JT9D operating in flight and statically was examined and it was concluded that:

- o The linear theory describes the inflight contraction of atmospheric turbulence for the JT9D.

- o The linear theory does not describe the contraction of atmospheric turbulence by the JT9D at the test stand. In this situation the non linear turbulence inertial effects are not negligible and the linear theory will overpredict the distortion of the turbulence field.

V. The contraction ratio in flight is of the order one and statically this ratio is large and so, bearing the comparison of the linear theories in mind, it is suggested that:

- o The simple model is quite adequate to describe the contraction of turbulence in flight for the JT9D.

- o Either the simple model or more rigorous theory produce an upper bound to the distortion of the atmospheric turbulence produced by the contraction due to the JT9D operating statically. A lower bound is provided by the assumption of a complete return to isotropy.

8.0 THE EFFECT OF A SCREEN ON ATMOSPHERIC TURBULENCE (Phase II, Task C)

8.1 Introduction

The problem of the interaction of screens and flow was originally addressed to optimize the design of screens for use in wind tunnels. These screens had been observed to suppress turbulent fluctuations in wind tunnel flow. The solution was provided, after several partially successful attempts by other investigators (16, 17, 18), by Taylor and Batchelor (19). They solved the problem for thin gauzes subject to flows of small turbulent intensity. They deduced the relationships between the upstream and downstream intensities and Batchelor (43), in a later, more elegant analysis showed the relationships between the velocity spectrum tensors of the two flow fields. They also considered specifically the case of initially isotropic turbulence and showed for this case, that the intensity ratios are independent of the form of the energy spectrum. The analysis, as in the contraction problem, was made tractable by a linearization of the Navier Stokes equations. This solution, as in the case of the contraction problem, results in no representation of the inertial "return to isotropy" phenomenon or viscous decay.

As noted before, the ability of the screen to attenuate unsteadiness in the flow is determined by two of its characteristics; (i) the pressure loss coefficient and (ii) the amount of turning the screen inflicts on the flow. The screens remove vorticity from the flow by absorbing it as a torque. In the following sections, a brief survey of the theory of Taylor and Batchelor is presented together with their approximate form. Then, using Lumleys results, it is shown that the results of Taylor and Batchelor's analysis for gauzes are applicable to honeycomb screens, if the incident turbulence scale is large compared to the honeycomb length. Subsequently, expressions for determining the pressure loss coefficient, K , and flow angle ratio, α, for honeycomb and perforated plate are given.

8.2 General Theory for Thin Screens

The fundamental assumption of Taylor and Batchelor's approach is that the turbulent velocity fields upstream and downstream of the screen do not decay and the distribution of energy is unchanged away from the screen. This, (coupled with the knowledge that the effect of the screen on the adjacent flow is due entirely to the pressure change across it, and is therefore irrotational), allows the velocity field induced by the screen to be superimposed on the turbulence field. In short, the convection process is linear, the effect of the screen on the flow field is linear, and therefore, the velocity fields can be summed. The flow is considered inviscid, except insofar as the screen constitutes an impedance to it, thus the turbulence generation characteristics of a screen are not accounted for. Furthermore, in Taylor and Batchelor's

treatment, the screen afflicts the flow with a sudden pressure drop and a sudden change in direction. The screen is therefore considered infinitely thin and appears to the turbulence as a continuum requiring that the transverse turbulent scales are large compared to the mesh size.

The condition under which the decay processes are negligible is that the time scale of the decay is large compared to the time taken for a particle to traverse the screen influenced flow region so that

$$\frac{1}{\overline{u_{ii}}} \frac{d\overline{u_{ii}}}{dt} \ll \frac{U_{1AV}}{\ell} \tag{23}$$

As in the contraction problem Batchelor approximates the derivative with an empirically derived relationship

$$\frac{d\overline{u_{ii}}}{dt} \sim \frac{(\overline{u_{ii}})^{3/2}}{\ell} \tag{24}$$

to reduce the criterion to

$$\frac{(\overline{u_{ii}})^{1/2}}{U_{1AV}} \ll 1 \tag{25}$$

Again, this empirical expression may not be valid for the screen region in view of the disruption of the decay process there. It does, however provide a tractable criterion for linearization and, in the absence of any superior relationship, will be used here. It should be noted that this linearization, performed in the absence of mean flow gradients, leads to turbulent velocity fields where vorticity is conserved. Only in the vicinity of the screen itself is there a change in vorticity.

Taylor and Batchelor argue that the effect of the screen on the flow is irrotational and therefore the contribution to the velocity field due to the screen may be expressed as a velocity potential. Thus the form of the total unsteady velocity field is

$$\underline{u}(x_1 - U_1 t, x_2, x_3) + \nabla \phi (x,t) \tag{26}$$

where $\underline{u}$ is the turbulent velocity vector far away from the screen.

With this velocity field form, and the linearization discussed previously, together with the small perturbation assumption, the problem is solvable since the upstream and downstream velocity fields may be related at the gauze through the screen pressure loss coefficient.

$$\left[\left\{\frac{\partial}{\partial t} + U_1 \frac{\partial}{\partial x_1}\right\}(\phi_B - \phi_A)\right]_{x_1=0} \underline{\Omega}\ K U_1 \left(u_{1A} + \frac{\partial \phi_A}{\partial x_1}\right)_{x_1=0} \tag{27}$$

The remaining relationships are those produced by considering

o The Turning of the Screen

$$\left\{u_{2A} + \frac{\partial \phi_A}{\partial x_2}\right\}_{x_1=+0} = \alpha \left\{u_{2B} + \frac{\partial \phi_B}{\partial x_2}\right\}_{x_1=-0} \tag{28}$$

$$\left\{u_{3A} + \frac{\partial \phi_A}{\partial x_3}\right\}_{x_1=+0} = \alpha \left\{u_{3B} + \frac{\partial \phi_B}{\partial x_3}\right\}_{x_1=-0} \tag{29}$$

o Continuity Across the Screen

$$\left\{u_{1A} + \frac{\partial \phi_A}{\partial x_1}\right\}_{x_1=+0} = \left\{u_{1B} + \frac{\partial \phi_B}{\partial x_1}\right\}_{x_1=-0} \tag{30}$$

o Continuity in the Upstream and Downstream Flow Fields

$$\nabla \cdot \underline{u}_A = 0$$
$$\nabla \cdot \underline{u}_B = 0 \tag{31}$$

In the above $\alpha \underline{\Omega}$ $\dfrac{\text{Local outflow angle}}{\text{Local inflow angle}}$

when the inequality (25) is satisfied, i.e., for small perturbations.

The coordinate system is shown in Figure 24.

If the turbulent velocities and potential are Fourier decomposed, then this set of equations allows the statistical characteristics of the upstream and downstream velocity fields to be determined in terms of the pressure loss coefficient, K, and the flow angle ratio α .

For the particular case of initially isotropic turbulence, Taylor and Batchelor found that the ratios of the mean square values of the upstream and downstream velocity components away from the screen were the same for all isotropic fields.

Specifically they found that

$$\mu_1 = \frac{\overline{u_{1B}^2}}{\overline{u_{1A}^2}} = \frac{(1+\alpha-\alpha K)^2+2\alpha^2}{(1+\alpha+K)^2-4} + \frac{(1+\alpha-\alpha K)^2-4\alpha^2}{(1+\alpha+K)^2-4}\,\frac{3}{2}(1-\mathcal{H}^2)$$
$$\left\{1+\frac{\mathcal{H}^2-\mathcal{K}^2}{2\mathcal{H}}\log\frac{\mathcal{H}-1}{\mathcal{H}+1}\right\} \tag{32}$$

$$\mu_2 = \frac{\overline{u_{2B}^2}}{\overline{u_{2A}^2}} = \alpha^2 + \frac{1}{3}\left[(1+\alpha-\alpha K)^2-(1+\alpha+K)^2\mu_1\right] \tag{33}$$

where,

$$\mathcal{K}^2 = \frac{(1-\alpha-\alpha K)^2}{(1-\alpha-\alpha K)^2-4\alpha^2}\,,\quad \mathcal{H}^2 = \frac{(1+\alpha+K)^2}{(1+\alpha+K)^2-4}\,,\quad 1+\alpha+K > 4$$

It is also possible to show (see Appendix D) that the form of certain integral length scale ratios is independent of the initial turbulence spectrum. Specifically

$$\frac{L_{11B}}{L_{11A}} = \frac{(\alpha K-1-\alpha)^2}{(K+1+\alpha)^2}\,\frac{1}{\mu_1}$$

$$\frac{L_{21B}}{L_{21A}} = \frac{\alpha^2}{\mu_2}\,,\quad \frac{L_{22B}}{L_{22A}} = \frac{\alpha^2}{\mu_2} \tag{34}$$

$$\frac{L_{31B}}{L_{31A}} = \frac{\alpha^2}{\mu_3}\,,\quad \frac{L_{33B}}{L_{33A}} = \frac{\alpha^2}{\mu_3}$$

For initially isotropic turbulence these ratios may be evaluated using Taylor and Batchelor's expressions for μ_1 and μ_2 for a gauze. For this case α and K are apparently related so that the velocity ratios may be plotted against K as shown in Figure 25. The corresponding scale ratios are shown in Figure 26. As Taylor and Batchelor note, in general, there exists a screen such that the integral length scale L_{11B} is totally suppressed. This occurs when

$$\alpha K - 1 - \alpha = 0 \tag{35}$$

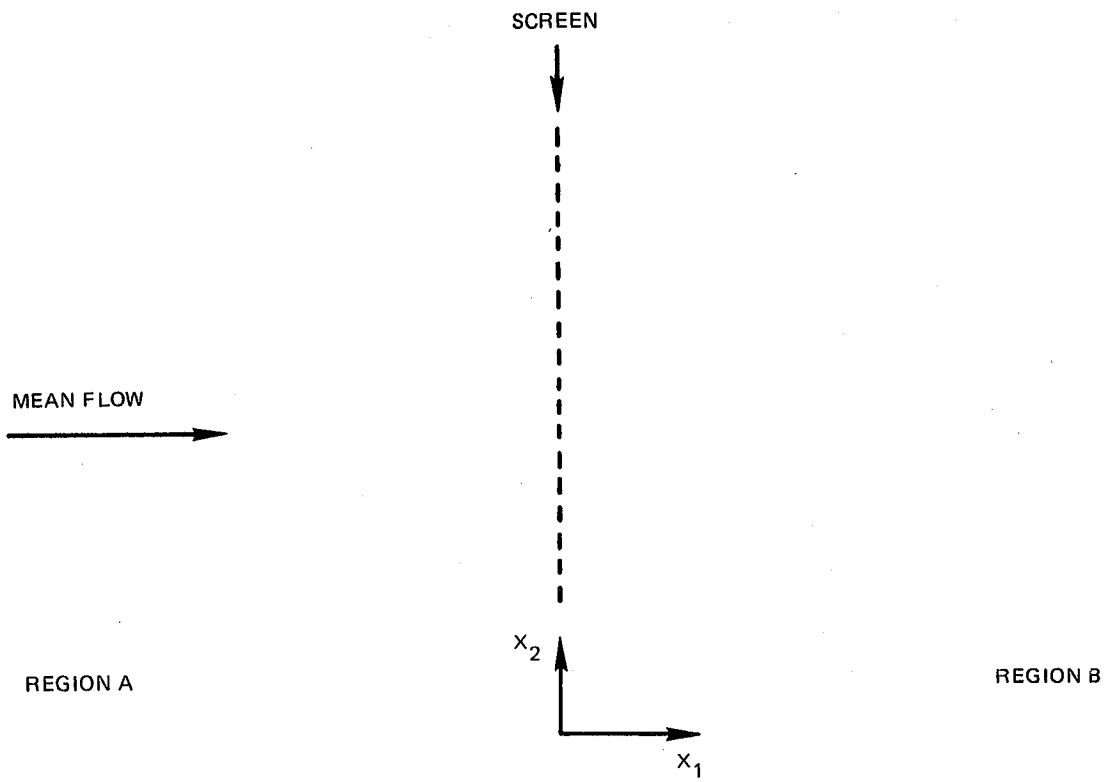

Figure 24 The coordinate system for Taylor and Batchelor's theory.

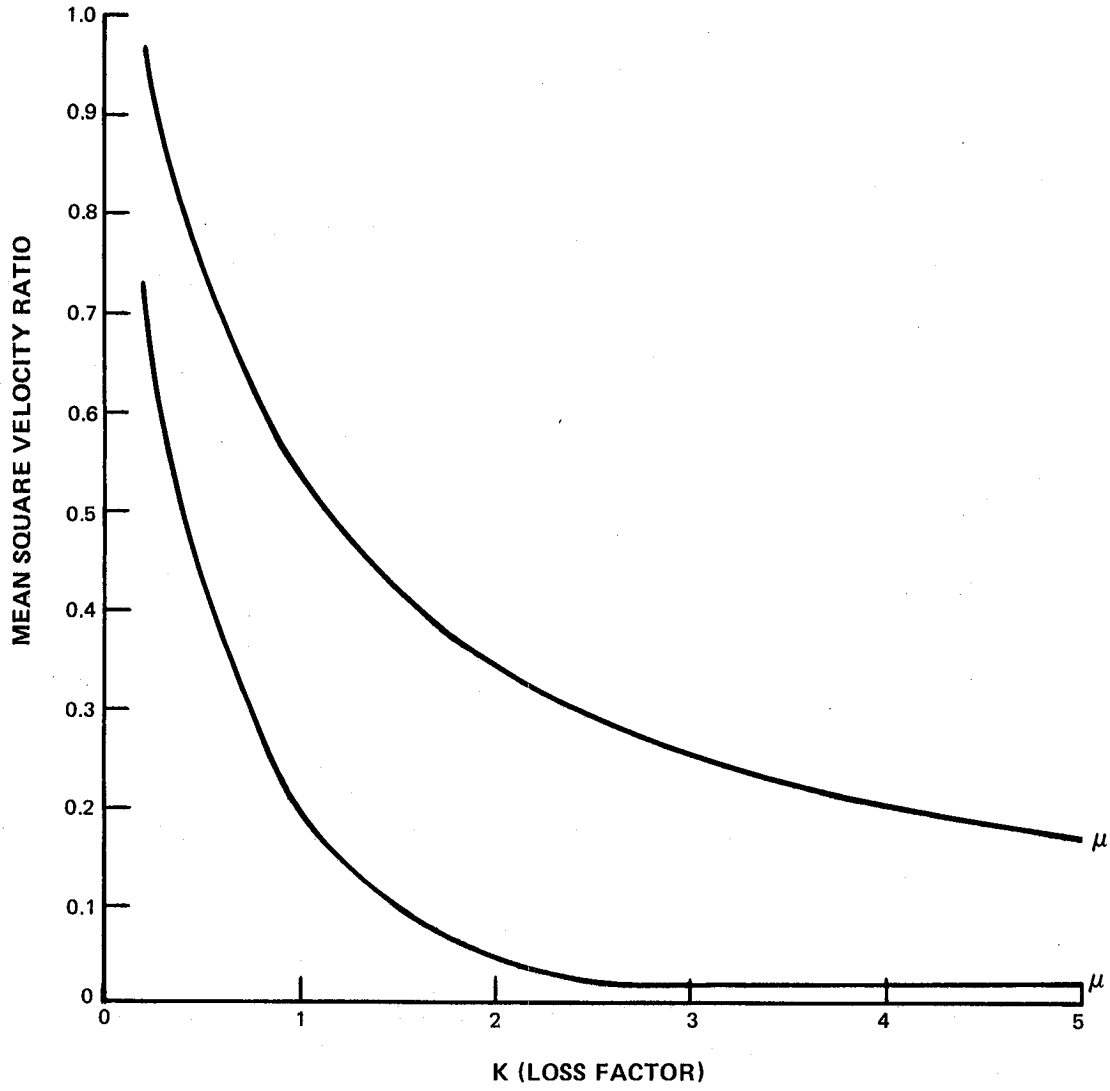

Figure 25 The ratios of the mean square velocity components upstream and downstream of a gauze (Taylor and atchelor).

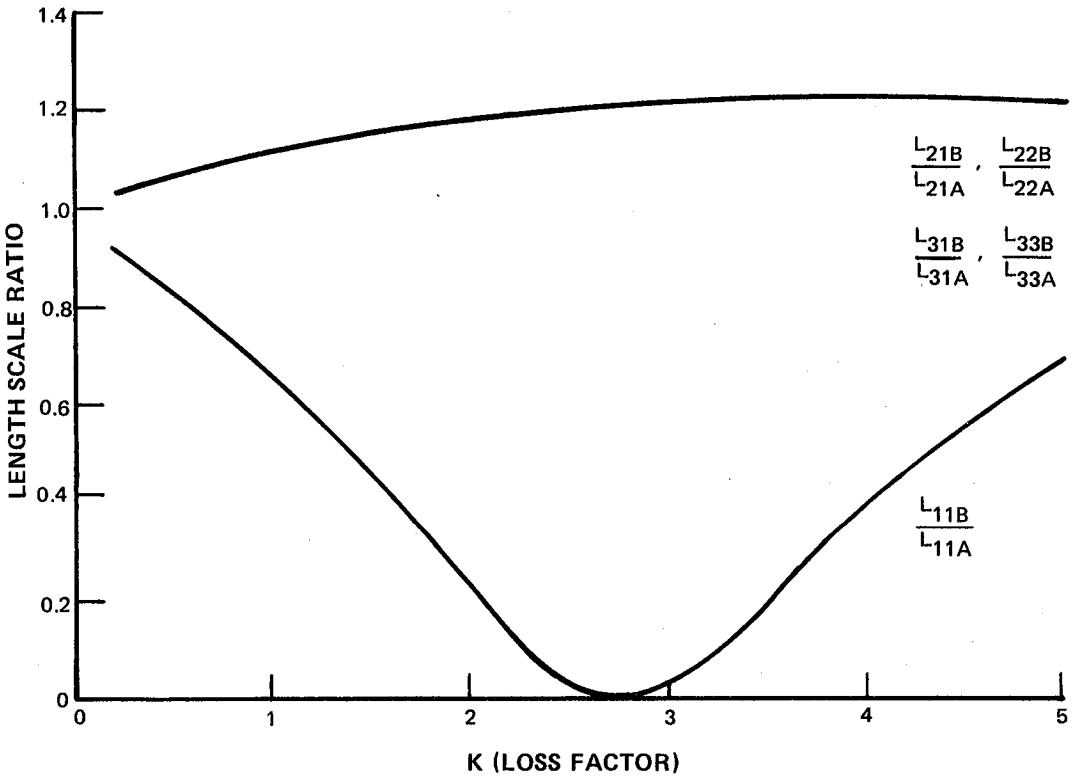

Figure 26 The ratios of the integral length scales upstream and downstream of a gauze.

The other scales in Equation 34 are suppressed when $\alpha = 0$.

The results of Taylor and Batchelor's analysis have been compared to data gathered by Townsend (45). On a kinetic energy basis there is close agreement between measurements and predictions (Figure 27) (Ignore the square symbols at this time). Comparisons of the mean square velocity ratios highlighted the absence of any "tendency to isotropy" considerations in the theory, Figure 28. (Ignore dashed lines at this time.) Townsend's measurements indicated a less anisotropic downstream field than Taylor and Batchelor would predict.

It is possible to determine, if a form for the upstream isotropic spectrum tensor is assumed, the changes in the one dimensional power spectral densities as a result of the turbulence being convected through the screen. The manipulations required are complicated and in view of the return to isotropy observed by Townsend would produce results that require empirical correction. Consequently a simpler model will be described that readily permits calculation of the change in the one dimensional spectra. While these results will probably also require empirical correction, it is considered that the amount will be no more than for the results of Taylor and Batchelor's more rigorous analysis.

8.3 Simple Screen Model

In a manner analogous to Prandtl's treatment of the contraction phenomenon, Taylor and Batchelor developed a simple model that considered the effect of a screen on simple flow distortion elements. These elements are (i) a steady distortion of the streamwise velocity component that varies sinusoidally in the transverse direction and (ii) an arbitrary steady transverse velocity distortion.

To determine the solutions of the problems, the Navier Stokes equations are linearized by requiring that the amplitudes of the distortions be small compared to the mean flow velocity. Viscous effects are also neglected except insofar as they give rise to the resistance of the screen. The assumption of incompressibility, applied to the first distortion element, leads to the equations of motion of the fluid, upstream and downstream of the screen, in terms of the stream function;

$$\nabla^2 \psi_A = u_{1A} k \sin k x_2 \qquad (36)$$

$$\nabla^2 \psi_B = u_{1B} k \sin k x_2 \qquad (37)$$

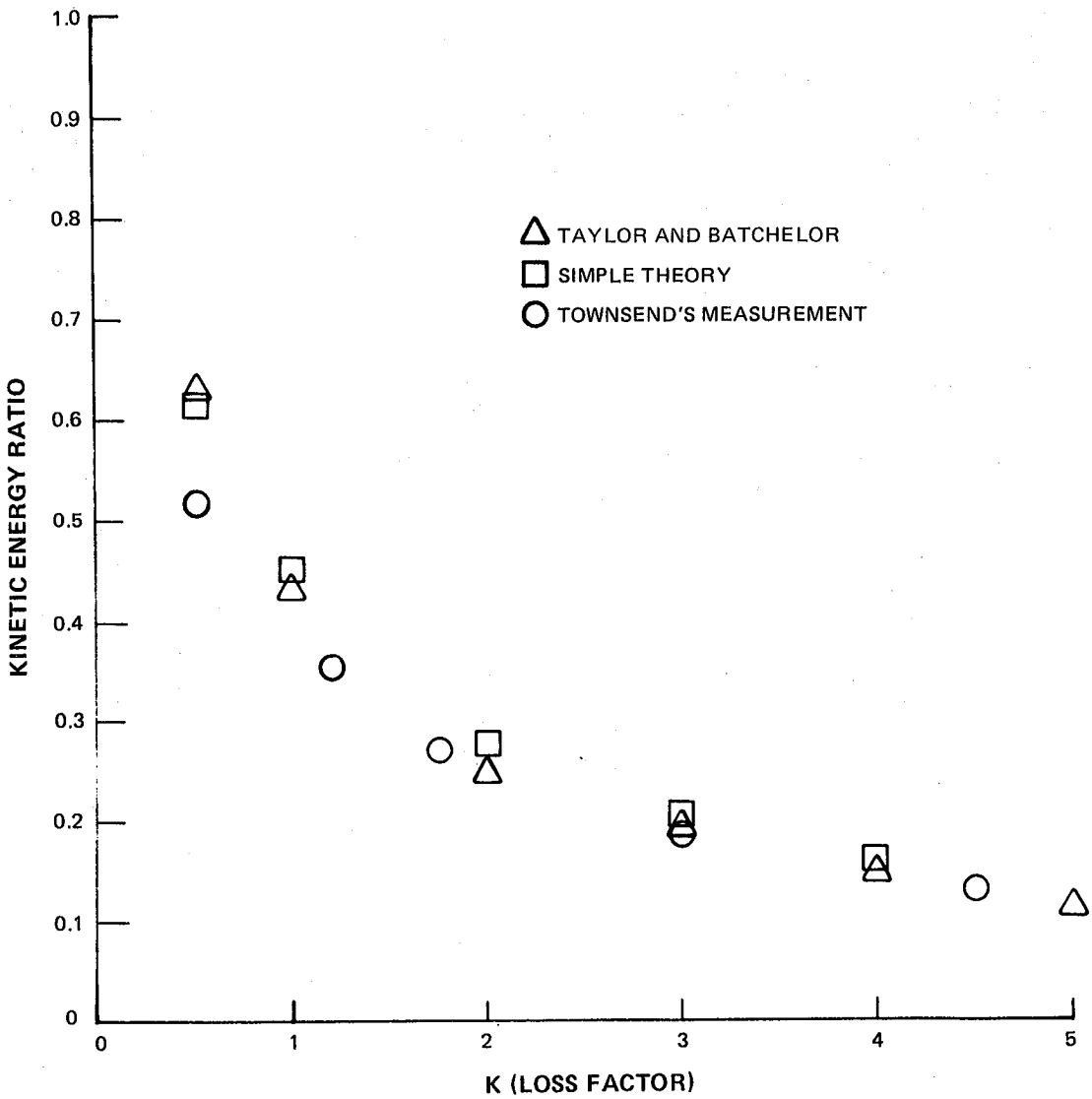

Figure 27 The comparison between measured and predicted turbulence kinetic energy ratios across a gauze.

Figure 29 depicts the geometry of the problem. If it is further assumed that the fluid perceives the screen as a continuous body then the solutions of these equations together with the boundary conditions at the screen, Equations 38, 39, and 40, allow the effect of the screen to be determined.

o Turning of the Screen

$$\left\{\frac{\partial \psi_B}{\partial x_1}\right\}_{x_1=-0} = \alpha \left\{\frac{\partial \psi_A}{\partial x_1}\right\}_{x_1=+0} \tag{38}$$

o Continuity Across the Screen

$$\left\{\frac{\partial \psi_B}{\partial x_2}\right\}_{x_1=-0} = \left\{\frac{\partial \psi_A}{\partial x_2}\right\}_{x_1=+0} \tag{39}$$

o Pressure Drop Across the Screen

$$\left\{\frac{\partial \psi_A}{\partial x_2}\right\}_{x_1=-\infty} - \left\{\frac{\partial \psi_B}{\partial x_2}\right\}_{x_1=+\infty} = K \left\{\frac{\partial \psi_A}{\partial x_2}\right\}_{x_1=0} \tag{40}$$

The boundary condition, Equation 40, also makes use of the small perturbation assumption. Solving these equations simultaneously Taylor and Batchelor concluded that

$$\frac{u_{1B}}{u_{1A}} = \frac{1-\alpha-\alpha K}{1+\alpha+K} \tag{41}$$

From this it can be deduced, in view of the linearity of the equations, that any combination of sinusoidal streamwise perturbation will be modified according to Equation 41.

The effect of the screen on this type of distortion is such that in the vicinity of the screen, the potential field results in a static pressure variation in the transverse direction. Fluid is thus directed laterally from the high to the low pressure region. Thus a transverse velocity component is induced in the flow. The magnitude of this component is determined by the resistance of the screen to the fluid. The

flow with the induced lateral velocity component is transported through the screen. The screen attenuates the lateral component according to the side load applied to the screen. The residual streamwise perturbation at the screen is attenuated according to the resistance of the screen. Downstream as the potential effect of the screen decreases the static pressure becomes uniform laterally and the transverse velocity component tends to zero.

The attenuation of a purely streamwise distortion, because of the screen induced lateral velocities, becomes then a function not only of the screen resistance but also of the ability of the screen to withstand a sideload.

As can be seen from Equation 41 there exists a condition when the streamwise perturbation is totally suppressed, this occurs when

$$1 + \alpha - \alpha K = 0 \tag{42}$$

and corresponds to the suppression of the integral length scale L_{11} noted in the previous section.

In the case of an arbitrary steady distortion in the transverse velocity field, the linearization leads to the deduction that the transverse velocity field is unaffected by the screen in that no potential field is superimposed on the flow by the screen. The change in the flow field across the screen is solely determined by continuity and thus by the ability of the screen to turn the flow. Thus

$$\frac{u_{2B}}{u_{2A}} = \alpha \tag{43}$$

The resistance of the screen is irrelevant for this type of disturbance.

Again the linearization of the problem allows Equations 41 and 43 to be applied separately to the individual components of a compound velocity field and the results recombined to form the downstream velocity field. The criteria for this linearization of the Navier Stokes equations are roughly

$$\begin{aligned} u_{1A} &\ll u_1 \\ u_{2A} &\ll u_i \end{aligned} \tag{44}$$

If a turbulence field is considered to be approximated by some superposition of the elements discussed above then an ensemble average of the square of the upstream and downstream perturbation velocity fields produces

$$\frac{\overline{u_{1B}^2}}{\overline{u_{1A}^2}} = \left(\frac{1+\alpha-\alpha K}{1+\alpha+K}\right)^2 \tag{45}$$

$$\frac{\overline{u_{2B}^2}}{\overline{u_{2A}^2}} = \frac{\overline{u_{3B}^2}}{\overline{u_{3A}^2}} = \alpha^2 \tag{46}$$

In order to further develop the simple model it is not necessary to evaluate Equations 45 and 46 for the purpose of comparison with predictions from the more rigorous theory and Townsend's data (45). Figure 27 shows this threeway comparison for overall turbulent kinetic energy change across the screen. In this comparison, a gauze is used for which it can be demonstrated that a relationship exists solely between α and K . An implication of a relationship existing between α and for gauzes is that both parameters are determined by the same geometric characteristics in the region where the relationship holds. This relationship is described and discussed further in Section 8.5. The pressure loss coefficient, K , is chosen as the independent variable for this comparison. The agreement between the two prediction methods and the data is generally very good.

The ratios of the mean square values of the individual velocity components are not as well predicted by either theory, as shown in Figure 28, although the theories are in reasonable agreement with each other. The reason is that downstream of the gauze turbulence inertial effects are not negligible and thus there is a tendency for the velocity field to become isotropic. Thus a possible modification to the simple model would be to assume that the downstream field is isotropic. Such an assumption, if the incident field were also isotropic would result in the relationship

$$\frac{\overline{u_{1B}^2}}{\overline{u_{1A}^2}} = \frac{1}{3}\left\{2\alpha^2+\left(\frac{1+\alpha-\alpha K}{1+\alpha+K}\right)^2\right\}. \tag{47}$$

The appropriateness of Equations 45 and 46 or 47 will be examined in Section 8.6.

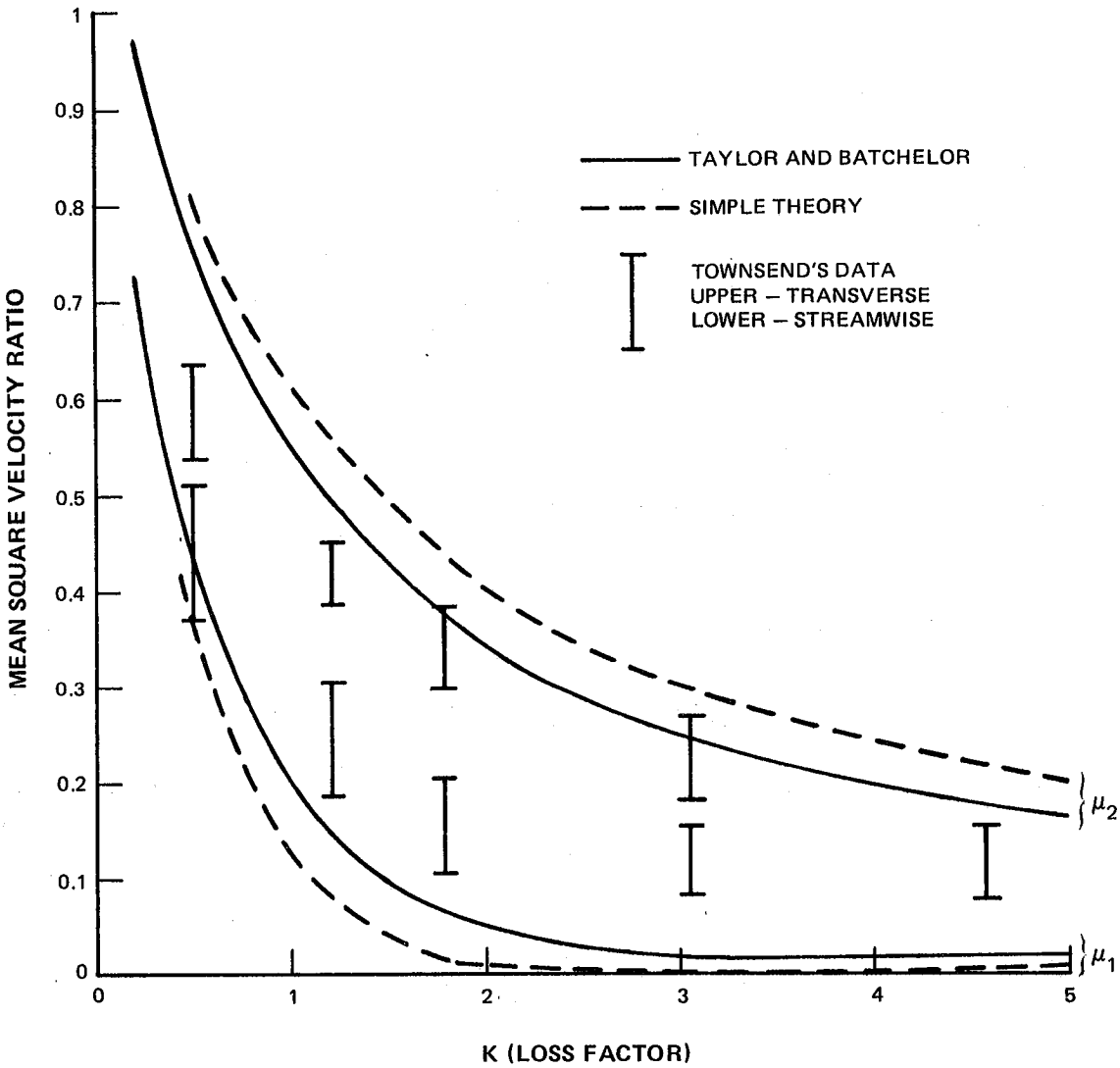

Figure 28 The comparison between measured and predicted mean square velocity ratios across a gauze.

The tendency to isotropy also alleviates the distortion of the length scales and the corresponding one dimensional spectra. To account for this effect, the simple model suggested here will incorporate this effect by having the same length scales upstream and downstream and the one dimensional spectra will be unchanged in shape, so that

$$L_{ijB} = L_{ijA} \tag{48}$$

$$F_{iB}(k_j) = A_i F_{iA}(k_j) \tag{49}$$

Where A_i is determined by Equations 45, 46.

There is some evidence in Townsend's data that the spectral relationships are approximately correct. Additionally, at least some of the length scales are substantially unchanged by the screen according to the more rigorous theory, see Figure 29.

This simple form of the theory provides a basis for generating empirical corrections from the measurements to be taken in the test program of Phase II, Task F. It should be emphasized that the theory above does not account for generation of turbulence by the screen. This aspect will be addressed in Section 8.7.

The theories described above assumed an infinitely thin screen, and as such should be applied only to thin screens and perforated plate. It is possible to extend these theories so they are applicable to finite depth screens such as honeycomb. This is the subject of the next section.

8.4 The Application of the Thin Screen Models to Honeycomb Screens

The analysis of Taylor and Batchelor assumes that the flow experiences an instantaneous total pressure drop at the screen. The consequence of this model is that the screen is, in effect, considered to be infinitely thin. Lumley (20) has attacked the problem for a specific situation of a honeycomb screen and so a formulation is available for a finite thickness screen acting on turbulence. If the contention that the gauze theory can be applied to honeycomb is correct, then a limiting case of Lumley's equation should give the same results as the Taylor-Batchelor theory. This comparison is made in the following text.

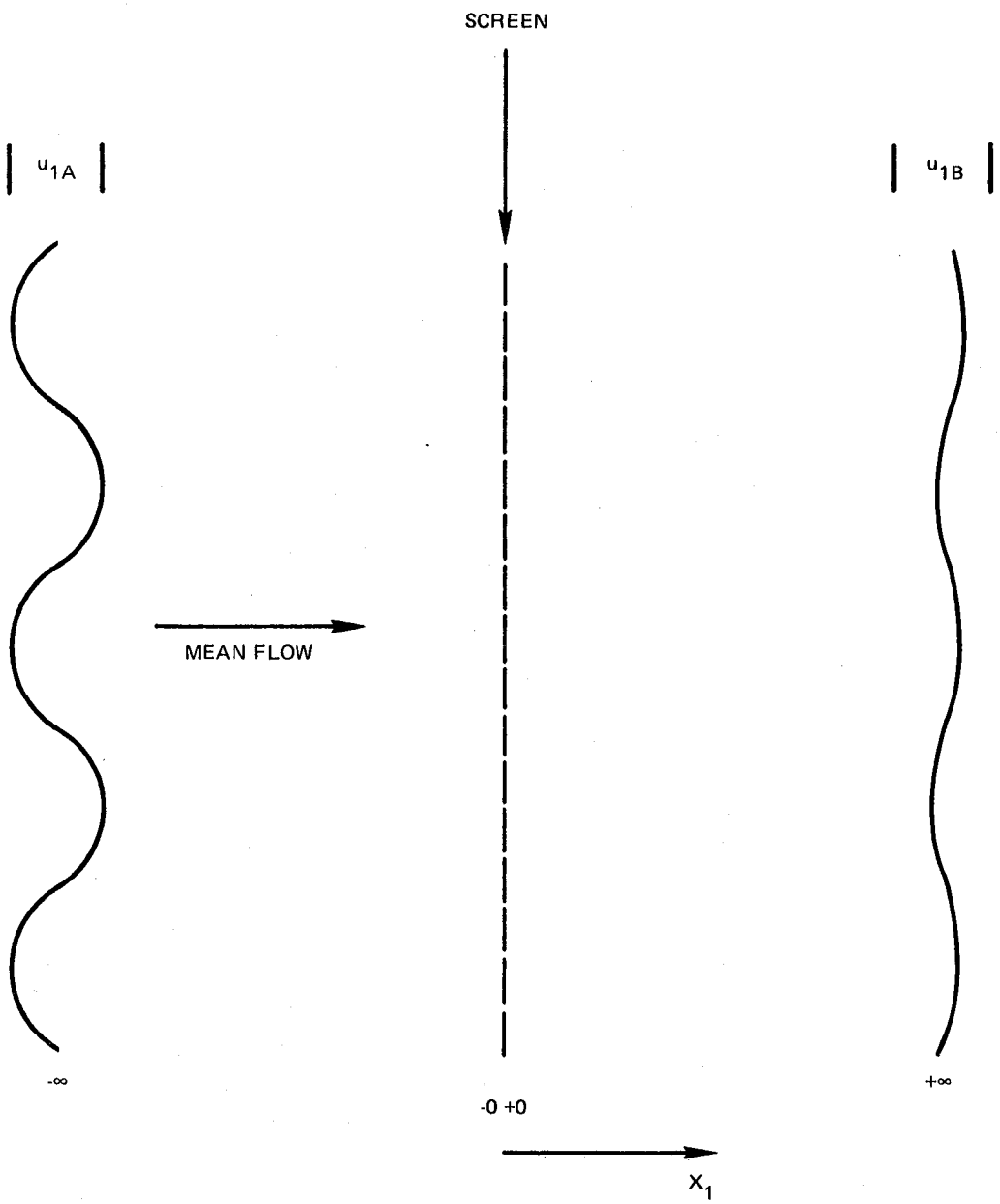

Figure 29 The simple screen model.

Lumley has derived a formulation for the effect of a honeycomb screen on a turbulent inflow for a specific set of conditions. He assumes that the inflow field is isotropic, that the honeycomb destroys all lateral velocity components and finally that downstream of the honeycomb there is a return to isotropy. From his theory he computes values of the ratio of the rms velocities, upstream and downstream, as a function of loss factor and the incoming streamwise length scale to cell depth ratio (Figure 30).

As this latter quantity becomes larger, the ratio of the mean square values of the velocity components tends to an asymptotic form solely dependent on the pressure loss coefficient. It is this form that is compared with the ratio determined from the simple model, since in this limit the honeycomb is perceived by the turbulence as being thin. Thus from Equation 46 setting $\alpha = 0$ to characterize the suppression of the transverse velocity by the honeycomb.

$$\frac{\overline{u_{1B}^2}}{\overline{u_{1A}^2}} = \frac{1}{3(1+K)^2} \qquad (50)$$

This corresponds to η of Lumley's formulation. A comparison of the results from the two theories is shown in Figure 31 and there is close correspondence. The asymptotic form of Lumley's theory is reached for streamwise length scales approximately equal to ten times the honeycomb thickness. This, therefore, constitutes a possible constraint on the application of Equation 50 to honeycombs.

Having established the region of validity of the simple theory, the evaluation of α and K for gauze and honeycombs will now be examined.

8.5 The Pressure Loss Coefficient and Flow Angle Ratio for Thin Screens and Honeycomb

In general, both the pressure loss coefficient, K, and flow angle ratio α, are dependent on the geometry of the screen and the nature of the flow i.e.

$$K = K(Re, M, G_1, \theta) \qquad (51)$$

$$\alpha = \alpha(Re, M, G_2, \theta) \qquad (52)$$

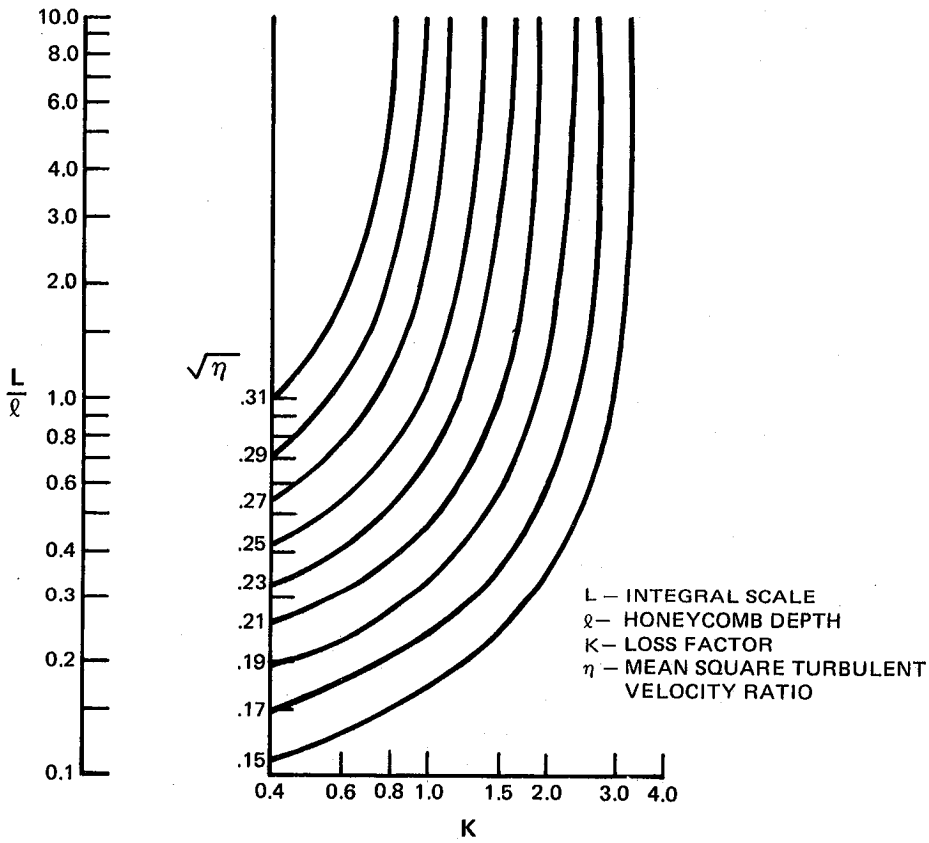

Figure 30 The graphical form of the results of Lumley's theory of honeycomb.

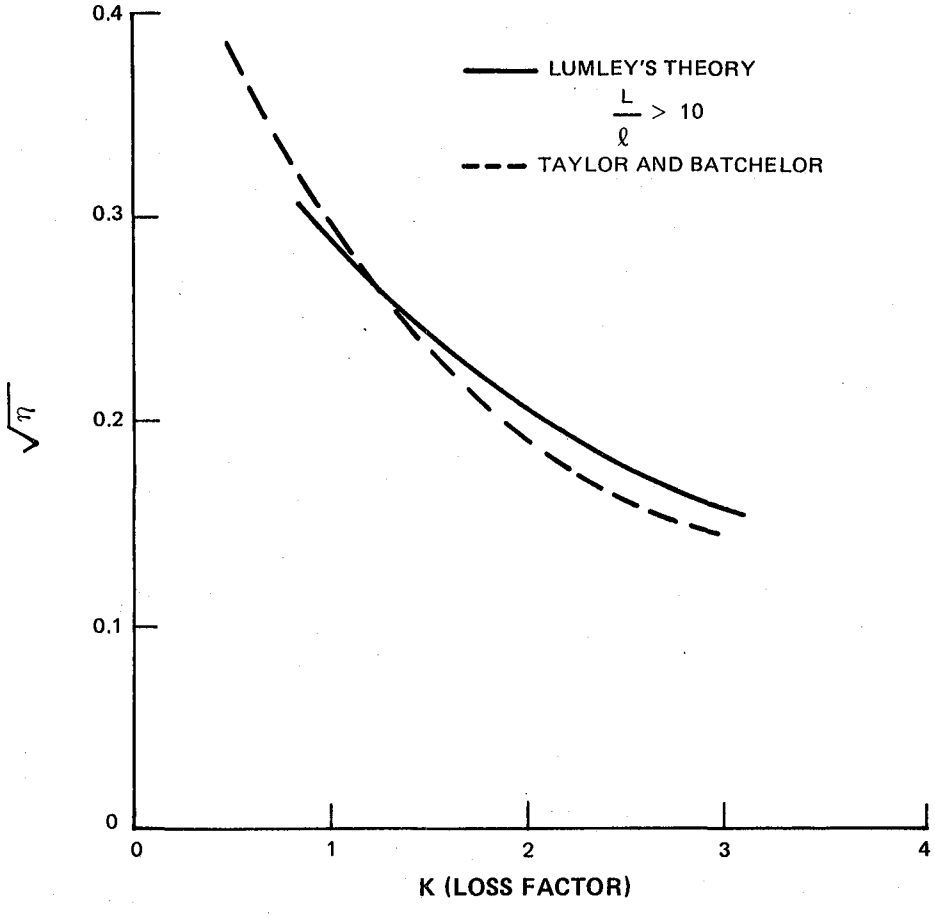

Figure 31 The comparison between the results of Taylor and Batchelor's gauze theory and a limiting case of Lumley's honeycomb theory.

Where G represents some geometric qualities. If compressibility effects are negligible and small incident flow angles are assumed, and if further, the turning of the screen is solely due to its potential effect on the flow then Equations 51 and 52 become

$$K = K\,(Re, G_1) \tag{53}$$

$$\alpha = \alpha\,(G_2) \tag{54}$$

Now the measurements of Dryden and Schubauer (46) lead to the conclusion that over the range of their experiment, the phenomenon is only weakly dependent on Reyonds Number, and if Equations (53) and (54) are examined in this light it seems quite reasonable to suspect that a relationship exists between α and K . Taylor and Batchelor determined that such a relationship existed from the above mentioned data and found that

$$\alpha = 1.1\,(1+K)^{-1/2} \qquad K > .7 \tag{55}$$

was reasonably good fit. Schubauer, Spangenberg and Klebanoff (47) determined that for $K <$ .7 their data was well fitted if

$$\alpha = \left(\frac{8-K}{8+K}\right) \tag{56}$$

It should be emphasized that these expressions are valid only for the small incident flow angles and were determined using gauzes. It is not known if other thin screens behave in this manner, however, it will be assumed here that they do and that Equations 55 and 56 apply to perforated plate screens in particular.

The pressure loss coefficient, K , depends on such geometric parameters as the hole density, hole diameter and thickness of the screen. Baines and Peterson (48) conducted extensive measurements on various thin screens forms including perforated plates and they noted that

$$K = \left(\frac{1}{C_c(1-s)} - 1\right)^2 \tag{57}$$

Where C_c is the contraction coefficient of a hole and s is the sceeen solidity. Their results were explainable in terms of this expression. The contraction coefficient is determined by the detailed geometry of the holes, ranging in value from .7 for sharp edges holes (thin perforated plate) to unity for well rounded holes. Figure 32 shows how the coefficient varies with solidity for different screen types. No dependence on a Reynolds Number based upon wire diameter or the equivalent dimension for a perforated plate was observed between values of 10^3 to 10^4. At low Reynolds Numbers, there is a dependence on that parameter, however, it is not anticipated that an inflow control screen will operate in this region.

To find a formulation for α and K that is suitable for a honeycomb screen requires consideration of the factors separately.

For the determination of α, it is noted that irrespective of the orientation of a flow with respect to the honeycomb, the flow perceives it as approximately a series of flat plates in cascade. Thus, it is suggested that the honeycomb acts on the flow in a similar manner to an infinite cascade of flat plates at zero stagger angle. The basic mechanism for deflection of the flow, namely, the loading of the material, is the same in each case and the magnitude of this loading is determined by the pitch-chord or diameter to length ratio. While the cascade effect is, essentially, a two dimensional phenomenon and, that due to the honeycomb, three dimensional, it will be assumed that the action of the honeycomb on the flow is axisymmetric and determined by the two dimensional model.

The solution to the cascade problem is presented by Von Karman and Burgers in (49) and is quite simple in form,

$$\alpha = e^{-\pi \frac{\ell}{d}} \tag{58}$$

With $\frac{\ell}{d}$ being the length to diameter ratio of the honeycomb.

This expression for the flow angle ratio for honeycomb does not have to stand alone, for as Prandtl notes, "a honeycomb length to diameter ratio of two is sufficient to straighten an incident flow field". More recently, the finding of Ginder, Kenison and Smith (33) that honeycomb of length to diameter ratios greater than two does not produce more turbulence attenuation is totally consistent with this form for α, since beyond this ratio, α is effectively zero. On a more personal level, anyone may blow through honeycomb at quite large angles of incidence and note that the flow is straightened for quite small values of ℓ/d.

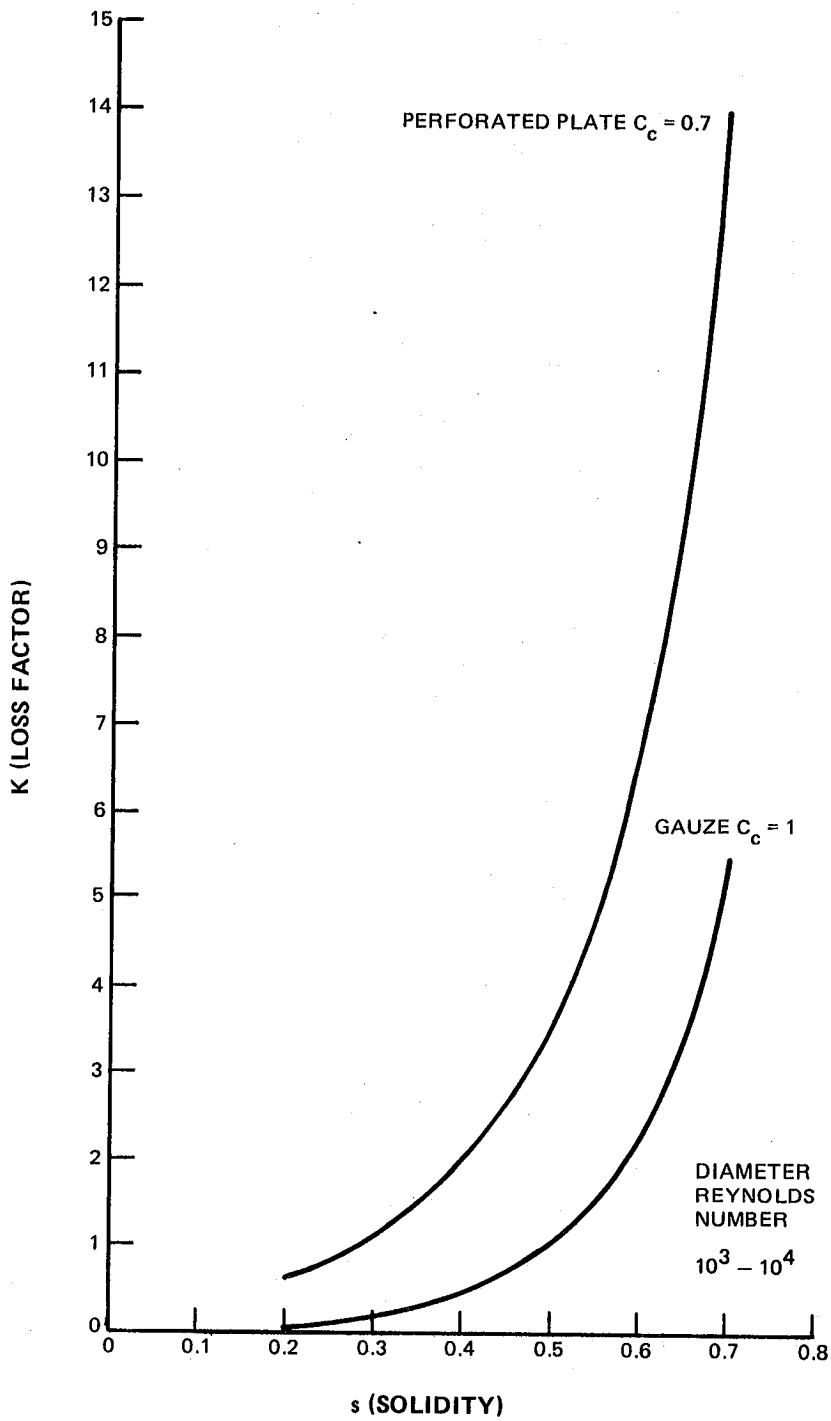

Figure 32 Thin screen loss factor.

To determine the pressure loss coefficient for honeycomb, Blasius' formula for the skin friction coefficient of turbulent flow in a pipe will be used, so that

$$K = \frac{.3164}{Re^{.25}} \frac{\ell}{d} \tag{59}$$

This empirical relationship is discussed by Schlichting (50) and is accurate in the range of diameter Reynolds Numbers from 3.10^3 to 10^5. Predictions of honeycomb loss coefficient using this expression were compared with measurements made by Paterson (51) (see Appendix E). Agreement was quite close.

It is quite possible that honeycomb screens will be operating at lower Reynolds Numbers than 3.10^3 and consequently the laminar pipe resistance coefficient might provide a more accurate expression,

$$K = \frac{64}{Re} \frac{\ell}{d} \tag{60}$$

This result of the solution of the Navier Stokes equations for Hagen-Poiseuille flow has compared well with measurements made in pipes containing laminar flow.

It is interesting to compare the effects on turbulence of thin gauze type screens with honeycomb. To facilitate this, an expression relating α and K for honeycombs can be obtained by combining Equations 59 and 60.

$$\alpha = exp\left[\frac{-\pi K Re^{.25}}{.3164}\right] \tag{61}$$

If a Reynolds Number of 1000 is assumed, (which corresponds roughly to a 6mm. honeycomb operating in a flow of 2 m/sec), it is immediately apparent that α tends rapidly to very small values for increasing K. The consequences of this behavior are shown in Figure 33 with predictions made using the simple theory. The transverse ratio moves rapidly to very small values and correspondingly, the streamwise ratio tends rapidly to decay as $(1+K)^{-2}$. The honeycomb then, in a sense, acts on the turbulent field, in an opposite manner to that of the thin screen. In the former, the transverse velocity components are preferentially

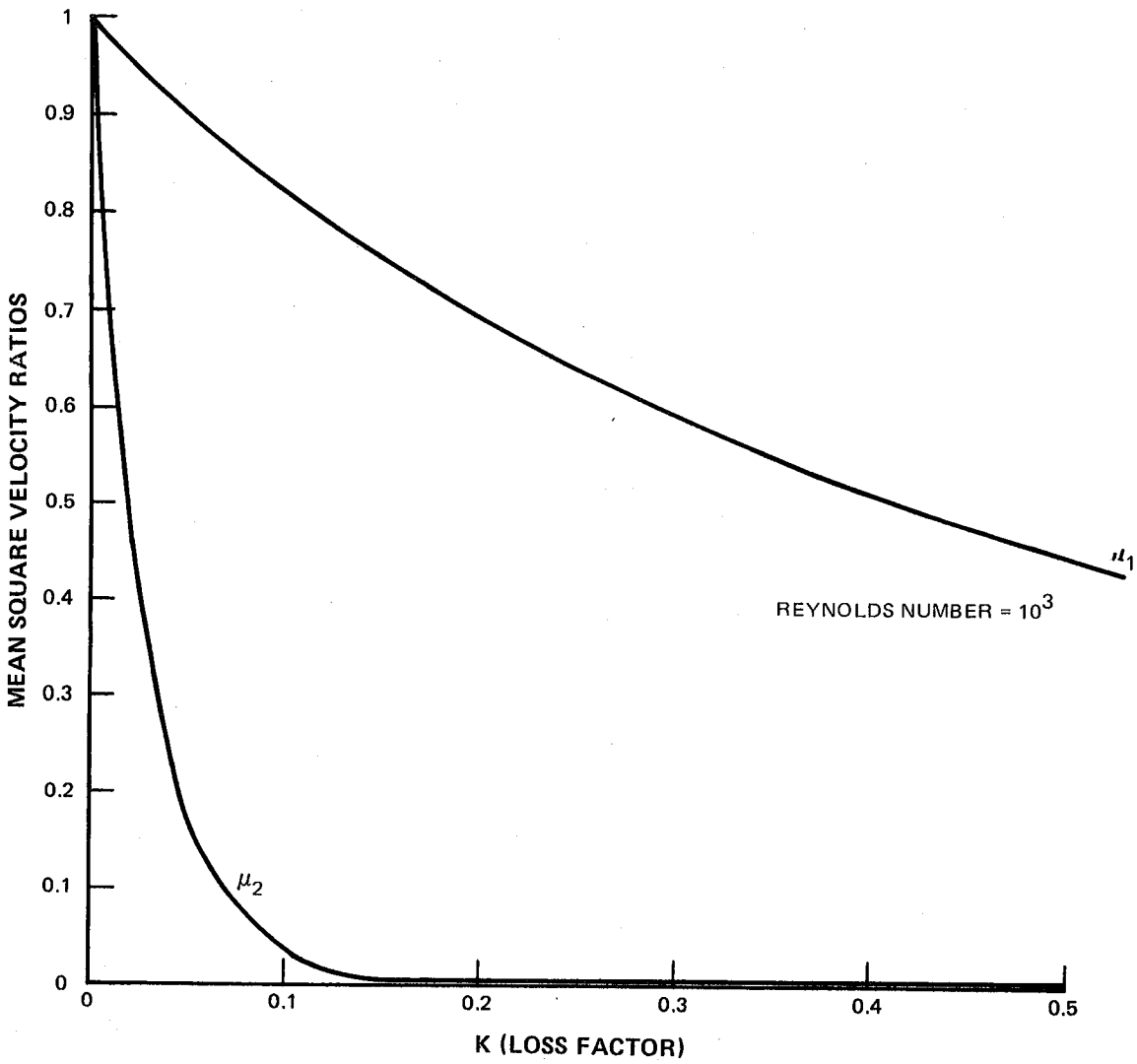

Figure 33 The mean square velocity ratios across a honeycomb.

suppressed while in the latter screen type, the streamwise components are attenuated most for a given screen loss coefficient. These complementary effects raise the interesting possibility of a combination screen that can attenuate an isotropic field and produce immediately downstream, another field that is at least isotropic as regards the mean square values of the component velocities.

8.6 The Application of the Simple Screen Model to a Screen Operating on Atmospheric Turbulence at the Test Stand

An important assumption that the linear theory rests on is that

$$\frac{(\overline{u_{ii}})^{\frac{1}{2}}}{u_1} \ll 1 \qquad (62)$$

This assumption corresponds to the requirement that turbulence inertial and viscous decay effects are unimportant whilst the flow is convecting through the region of influence of the screen. The validity of this assumption can be assessed using the results of the atmospheric turbulence model described in the Phase I Report. A typical value for $\left(\frac{\overline{u_u}}{u_1}\right)^{1/2}$ in the atmosphere near the ground is .3, however, at the screen, there is a superimposed velocity field due to the engine operation. For a JT9D at approach and a screen mounted at 4m. radius, this velocity will be about 7 m./sec. The typical mean atmospheric velocity used to compute a value of .3 was 2.68 m./sec., so that when the engine inflow field is imposed on the atmosphere, an overall intensity on the average of .3 x 2.68/4.84 = .167 at the screen would be expected. Consequently, the linear theory criterion is marginally satisfied for a static test situation. In addition, the satisfaction of this criterion means that the incident flow angles are sufficiently small so that the constancy of α and K is assured and the expressions for these factors are valid. The flow does not suffer from compressibility in this region. The change in the turbulence field across the screen is thus probably reasonably well approximated by the linear models. However, the subsequent tendency to isotropy which apparently is greater according to the extent of the anisotropy of the field is not modeled.

In view of the nature of the return to isotropy as described by Townsend (45) in which there is a rapid readjustment followed by a very slow return to isotropy, it is probably that neither the anisotropic nor the isotropic form of the simple model will exactly describe the phenomenon. The anisotropic form of Equations 45 and 46 will over estimate the distortion of the turbulence field by the screen while the isotropic form of Equation 47 will underestimate that distortion. Hence the two forms put bounds on the values of the turbulent velocity ratios, and can be used in this manner. The data gathered in the Phase II task of test program will be used to select the model that best describes the data and also to provide an empirical correction to that model.

8.7 Distortions Induced By Screens

A simple model has been presented that describes the phenomenon of turbulence convected through gauze type and honeycomb screens. The model does not consider self-generated distortions of which there are two types: one generated by unsteady deflection of the screen and the other consisting of the wakes and vortices shed from screen elements. The subject of screen deflection is discussed first.

If the screen is exposed to an unsteady vortical flow and deflects under the corresponding unsteady applied torque, then, as the applied torque varies, so will the screen torsional deflection thus imparting a swirling motion to the flow. The screen, then, in addition to suppressing vorticity in the flow, can also add vorticity. This effect can be important if the screen deflects significantly as an eddy passes through it. For after the eddy has passed, the screen will unwind and thereby impart a swirl to the flow that is coherent roughly over the area of the initial eddy. Thus eddies having scales that result in significant turbulence rotor interaction noise levels may not be effectively suppressed. It is, therefore, necessary that this type of screen induced distortion be minimized by either making the screen sufficiently torsionally rigid or mounting another screen downstream of it.

The other type of screen-induced distortion, that due to the wake of the screen, in general, will not be significant as regards turbulence - rotor interaction noise in view of the very small scales involved. However, wakes and vortices shed from screen structural support members may be important. This latter distortion can be effectively minimized by design or by suppression after it has been generated.

8.8 Conclusions

The theory developed by Taylor and Batchelor for the effect of a screen on small turbulent fluctuations has been discussed. Their linear theory does not account for turbulence inertial effects in the vicinity of the screen and thus the tendency to isotropy observed by Townsend and others is not described. A simplified form of the results of Taylor and Batchelor produces predictions that are in reasonable agreement with the more rigorous theory predictions. This simplified model relates pre-screen and post screen turbulence characteristics in terms of the flow angle ratio α , and pressure drop coefficient K , of the screen and these relations are

- The turbulence kinetic energy ratio

$$\frac{(\overline{u_{ii}})_B}{(\overline{u_{ii}})_A} = 2\alpha^2 + \left(\frac{1+\alpha-\alpha K}{1+\alpha+K}\right)^2$$

- The component mean square velocity ratios

$$\frac{(\overline{u_i^2})_B}{(\overline{u_i^2})_A} = A_i \;, \quad A_i = \left(\frac{\alpha + 1 - \alpha K}{1 + \alpha + K}\right)^2, \quad \alpha^2, \alpha^2$$

- The length scale ratios

$$L_{ijB} = L_{ijA}$$

- The power spectral density ratios

$$F_{iB}(k_j) = A_i \, F_{iA}(k_j)$$

Taylor and Batchelor's theory is applicable for situations where the flow perceived the screen as a homogeneous device, i.e., where turbulence scales are large compared to a characteristic transverse screen dimensions. Also a thin screen is assumed. It was demonstrated that the model is applicable to honeycomb type screens if they appear thin to the turbulent flow field, i.e., the turbulent scales are large compared to the honeycomb length. The forms of α and K are different for these two types of screens. The expressions identified for these quantities are:

- For gauze screens or perforated plate

$$K = \left\{\frac{1}{C_c(1-s)} - 1\right\}^2$$

$$\alpha = \frac{1.1}{(1+K)^{1/2}} \qquad K > .7$$

$$\alpha = \frac{8-K}{8-K} \qquad K < .7$$

where C_c is the hole contraction coefficient and s is the screen solidity.

- For honeycomb screens

$$K = \frac{.3164}{Re^{.25}} \frac{\ell}{d}$$ turbulent

$$K = \frac{64}{Re} \frac{\ell}{d}$$ laminar

$$\alpha = \bar{e}^{\pi \frac{\ell}{d}}$$

where $\frac{\ell}{d}$ is the length to diameter ratio of the honeycomb.

The expressions for honeycomb pressure drop coefficient are solely based on pipe friction. It is possible that there is a significant contribution to this quantity from other components of the honeycomb form drag.

The distortions generated by the screen itself were also discussed and in summary these are:

- Small scale turbulence determined by the detailed nature of the screen and insignificant as regards the generation of tone noise.
- Wakes and vortices generated at screen support structure and at screen discontinuities that are possibly significant in the generation of tone noise.
- Distortions caused by deflection of the screen, upon removal of torques applied to the screen by upstream unsteady distortions. These could be of importance in tone generation.

The latter two self induced distortion types can be readily avoided or eliminated by proper design.

9.0 THE EFFECT OF A FLOW CONTRACTION AND SCREENING ON A STEADY DISTORTION (Phase II Task D)

9.1 Introduction

Atmospheric turbulence, as discussed previously, is not the sole source of distortion of the inflow to an engine. The engine itself induces a velocity field over adjacent surfaces and thereby produces distortions to the flow such as wakes and vortices. Also the general asymmetry of the test stand situation results in a non-uniform inflow to the engine. These self-generated distortions are somewhat unsteady, due in part to the viscous effects at the generating surface and in part, due to modulation of the distortion by atmospheric turbulence and engine speed variations. Furthermore, the inflow distortion field is inhomogeneous and thus when it is modulated, it is perceived by a fixed transducer to be non-stationary. The modulating flow is at low frequency, so that over some period of time, the flow over the generating surface may be considered to be steady. Therefore, approximately, the effect of the modulation is to change the position of the distortion but not its structure. Thus in a frame of reference attached to the distortion, the velocity field is deterministic, approximately, and the mean value of the distortion velocity field exists. The phenomenon so described, may be termed "quasi-steady" in that the nature of the distortion as viewed from a frame attached to itself is approximately the same as that of a distortion from the same generating surface in a steady flow.

The vortex attached to the ground plane may be considered quasi-steady. It does exhibit intermittent growth and destruction (51), however, its structure is well defined over periods of time long compared to a rotor period and may therefore be treated as a steady distortion.

This section is concerned with the modification of the mean value of the velocity field associated with these types of distortion. The models used are substantially those described in Sections 7 and 8.

9.2 Contraction of a Steady Distortion

In Section 7, it was determined that distortions of the streamwise velocity component were attenuated, by a contraction, according to

$$\frac{\Delta u_{1B}}{\Delta u_{1A}} = \frac{1}{\ell_1} \qquad (63)$$

The steady velocity component of a wake will in addition be modified by dissipation through viscosity over the length of the contraction. The attenuation of Equation 63 is therefore a lower bound on the amount by which a wake will be suppressed. The contraction of a dissipative wake will now be considered.

The characteristics of the wake at the fan face of most interest from the point of view of fan noise generation are its width and velocity deficit. These characteristics are assumed to evolve according to

$$\Delta U_1 \propto \frac{U_{1\infty}(C_D a)^{1/2}}{X^{1/2}}$$
$$b \propto X^{1/2}(C_D a)^{1/2} \tag{64}$$

which corresponds to the development of the far wake of a rod of diameter a and drag coefficient C_D.

Further, to permit a tractable model to be constructed using existing theories for wake contraction and dissipation, it is assumed that this wake develops through the contraction in alternating purely dissipative regions and instantaneous contractions. In this manner, the contraction characteristic can be approximated by a series of steps, see Figure 34. Each dissipative region is characterized by a value of $U_{1\infty}$, $C_D a$, and X. The latter quantities in any dissipative region can be considered to be the virtual characteristics that, in a uniform flow, will produce the same wake as that present in the dissipative region. In the limit of an infinite number of dissipative regions of infinitesimal extent $C_D a$ and X, like $U_{1\infty}$, become continuous functions of position. In this limit, the wake characteristics at r_o can be related to some reference wake characteristics at such that

$$\frac{\Delta U_1(r)}{\Delta U_1(r_o)} = \frac{U_{1\infty}(r)}{U_{1\infty}(r_o)} \cdot \left|\frac{C_D a(r)}{C_D a(r_o)}\right|^{1/2} \left|\frac{X(r_o)}{X(r)}\right|^{1/2} \tag{65}$$

$$\frac{b(r)}{b(r_o)} = \left|\frac{X(r)}{X(r_o)}\right|^{1/2} \left|\frac{C_D a(r)}{C_D a(r_o)}\right|^{1/2} \tag{66}$$

Now $U_{1\infty}(r)$ is defined directly by the flow speed in the contraction, so that the problem is reduced to finding $C_D a$ (r) and X (r), the virtual characteristics of the wake. It can be shown that these become (Appendix F)

$$C_D a(r) = \{\ell_1(r)\}^{-5/2} C_D a(r_o) \tag{67}$$

$$X(r) = \{\ell_1(r)\}^{3/2} X(r_o) + \int_{r_o}^{r} \left\{\frac{U_{1\infty}(r)}{U_{1\infty}(r')}\right\}^{3/2} dr' \tag{68}$$

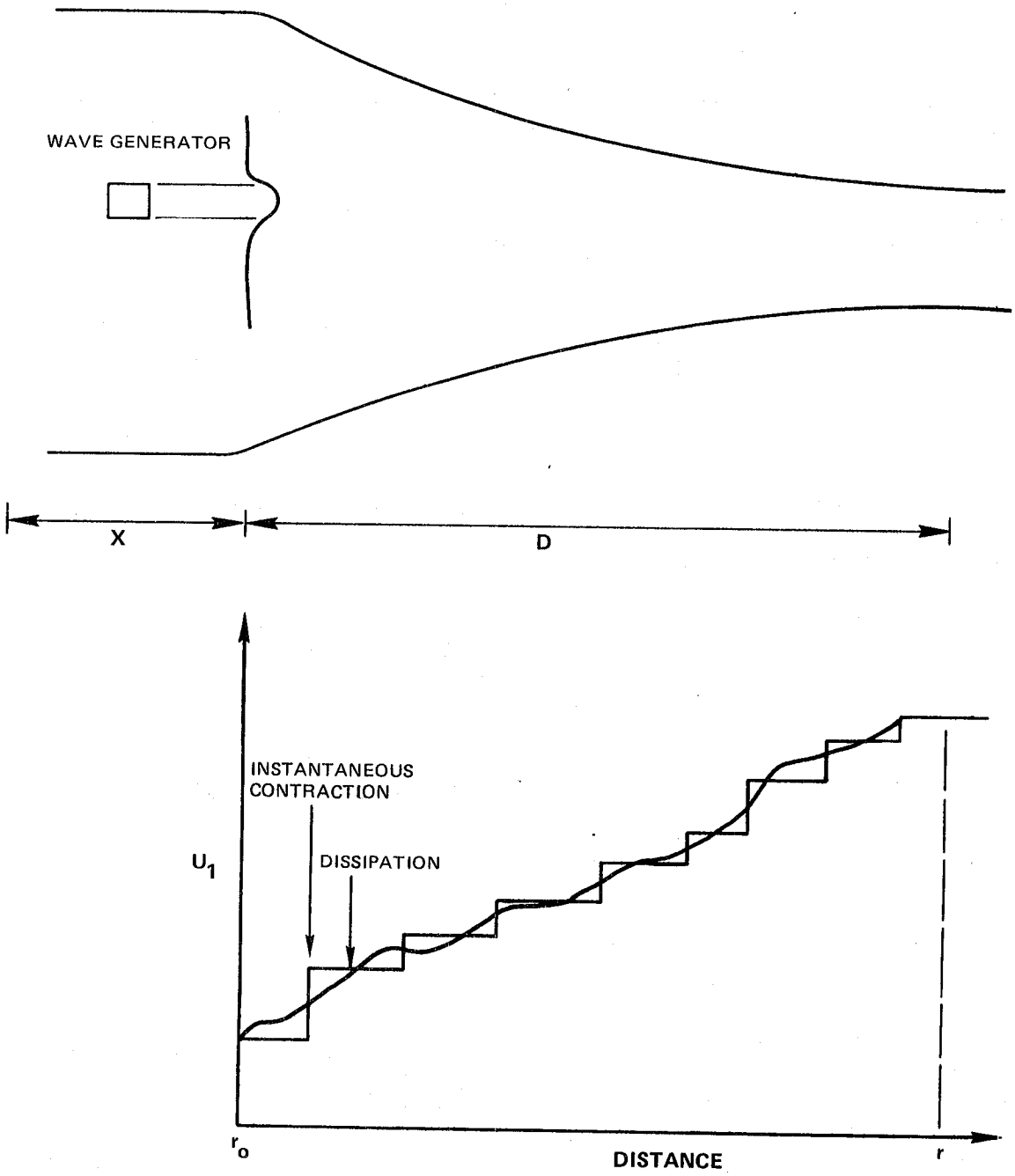

Figure 34 The approximation of the contraction characteristic.

In the limit of a uniform flow, Equations 65 and 66 degenerate to the purely dissipative forms and conversely for the zero dissipation situation the contraction form alone is recovered. If a contraction characteristic of the type

$$U_{1\infty}(r') = \left[U_{1\infty}(r) - U_{1\infty}(r_o)\right]\left(\frac{r'-r_o}{r-r_o}\right) + U_{1\infty}(r_o) \qquad (69)$$

is assumed which corresponds to a linear variation in velocity through the contraction, 65 and 66 reduce to

$$\frac{\Delta U_1(r)}{\Delta U_1(r_o)} = \left\{\ell_1(r)\right\}^{-1/4}\left\{\ell_1(r)^{3/2} + \frac{2(r-r_o)}{X(r_o)}\cdot\frac{\ell_1(r)}{(\ell_1(r)^{1/2}+1)}\right\}^{-1/2} \qquad (70)$$

$$\frac{b(r)}{b(r_o)} = \left\{\ell_1(r)\right\}^{-5/4}\left\{\ell_1(r)^{3/2} + \frac{2(r-r_o)}{X(r_o)}\cdot\frac{\ell_1(r)}{(\ell_1(r)^{1/2}+1)}\right\}^{1/2} \qquad (71)$$

These expressions were evaluated and the results shown in Figures 35 and 36. As was expected, the alleviation of the velocity deficit by dissipation is accentuated by the contraction. The wake width, however, can either increase or decrease through a contraction depending on the relative strengths of the two effects. It should be noted that Equations 70 and 71 are the results for a two-dimensional self similar wake convected through a one dimensional flow contraction. These expressions will be assessed using the results from the test program.

Consideration of the constancy of circulation in Section 7 leads to the relationship between transverse velocities in a vortex upstream and downstream of a contraction. It was found that

$$\frac{U_{2B}}{U_{2A}} = \sqrt{\ell_1} \; ; \; \frac{r_B}{r_A} = \frac{1}{\sqrt{\ell_1}} \qquad (72)$$

This expression will be used to define the effects of contraction on steady or quasi-steady vortical flows. However, these expressions do not tell the whole story. A vortex convected through a contraction will also experience changes in the axial velocity component. Batchelor (53) states that "acceleration of the fluid outside of the vortex leads to a change of axial velocity of the fluid within the vortex which is in the same direction and of greater magnitude than that outside". This effect will be studied in greater detail once test data from the test program becomes available.

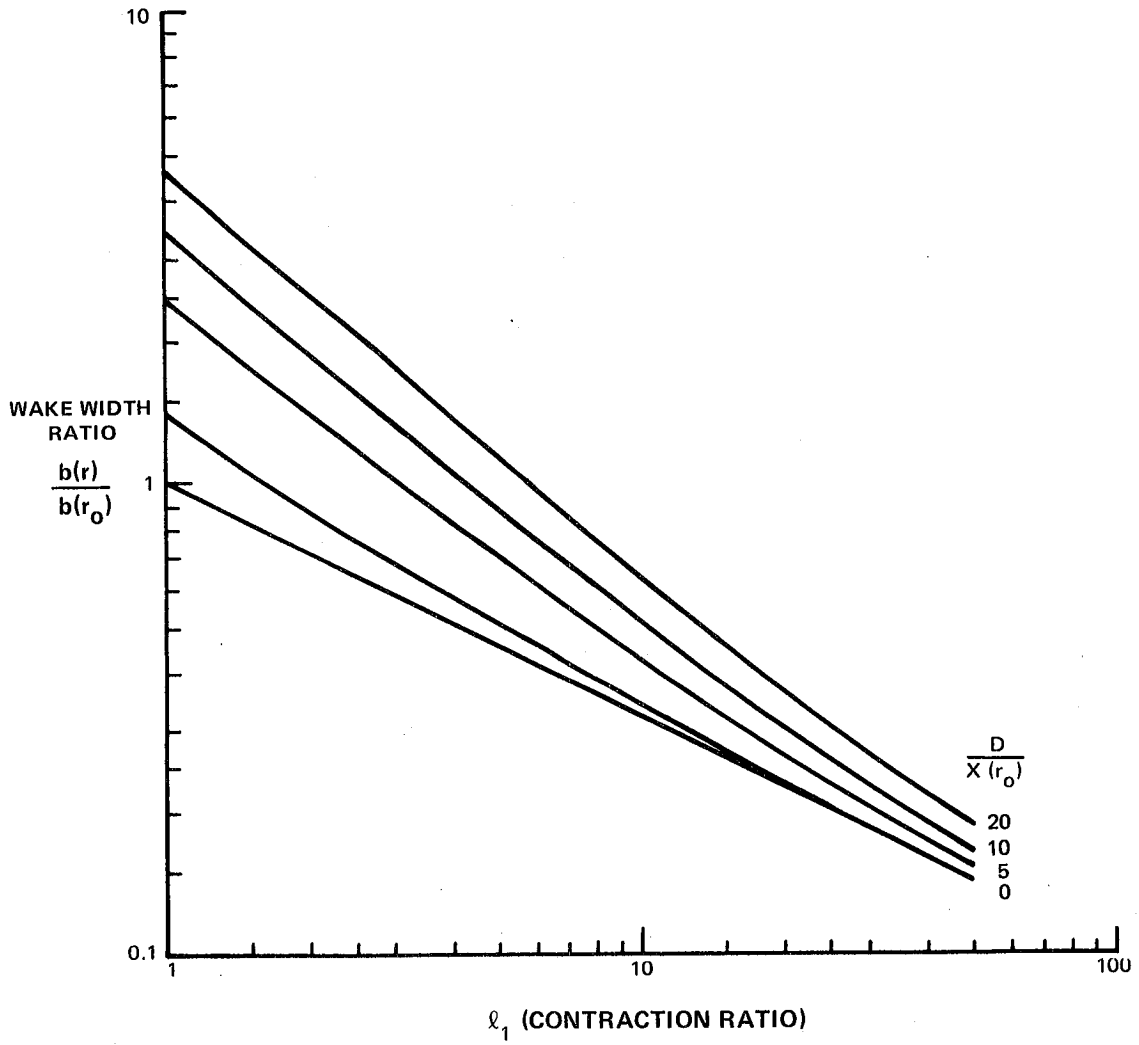

Figure 35 The contraction of a viscous wake on the effect on wake width.

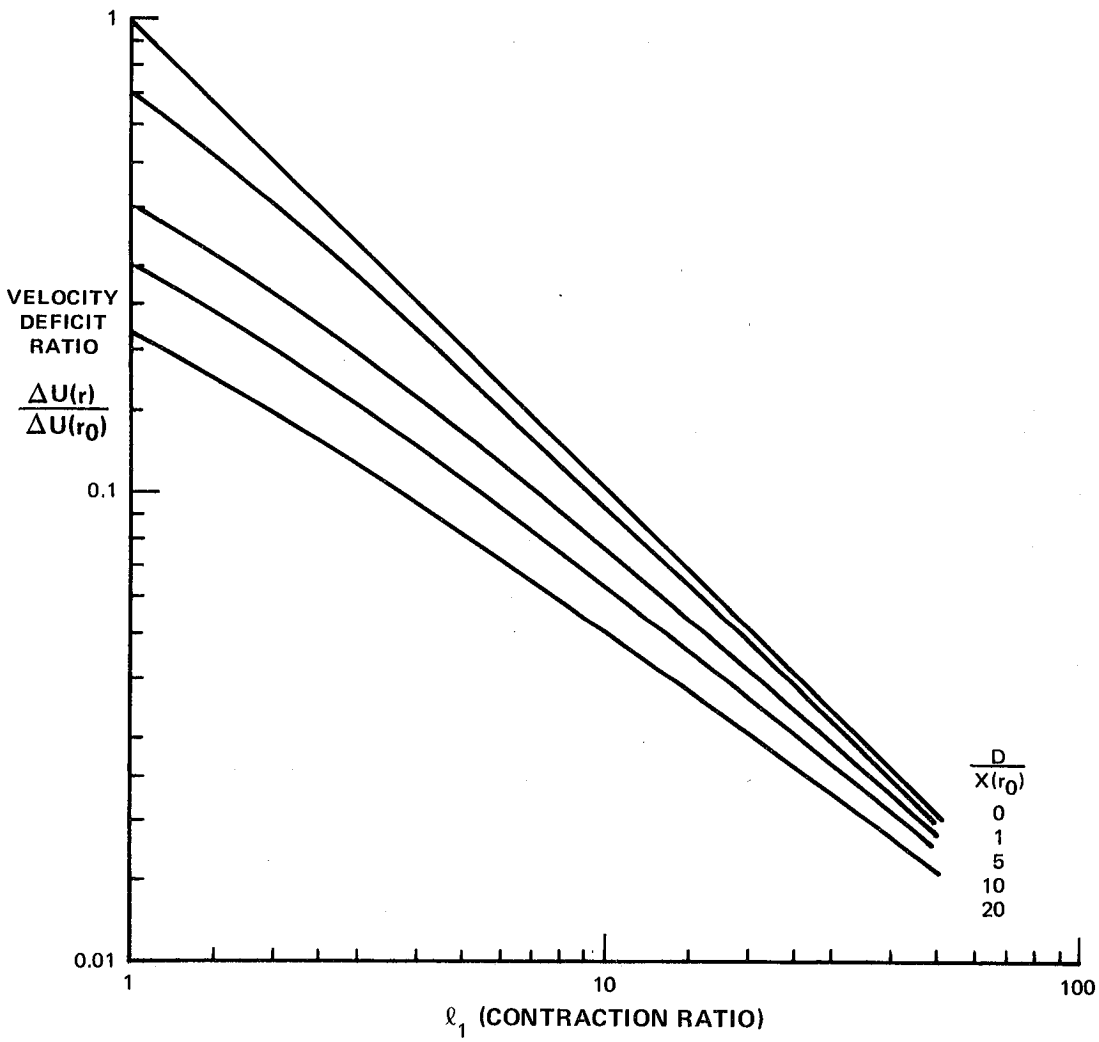

Figure 36 The contraction of a viscous wake on the effect on wake velocity deficit.

9.3 The Effect of a Screen on a Steady Distortion

The modification of a steady distortion by a screen is described by Equations 41 and 43, which were developed to define the effects of the screen on turbulence. Figures 37 and 38 show how the steady velocity components are attenuated by honeycomb and gauze type screens in terms of their characteristic parameters (length to diameter ratio and solidity, respectively).

The constraints on these expressions are that the distortions are small compared to the mean flow velocity at the screen. In the static test situation, this constraint is probably satisfied by the distortion in the streamwise velocity component. However, the transverse velocities encountered in a ground vortex may, at the screen be substantial. Again, the data from the test program will be used to modify the model as required to account for this.

9.4 Conclusions

In summary, the effect of contraction and screening on steady or quasi-steady distortions is modelled by Equations 70, 71 and 72 for contraction and Equations 41 and 43 for screening.

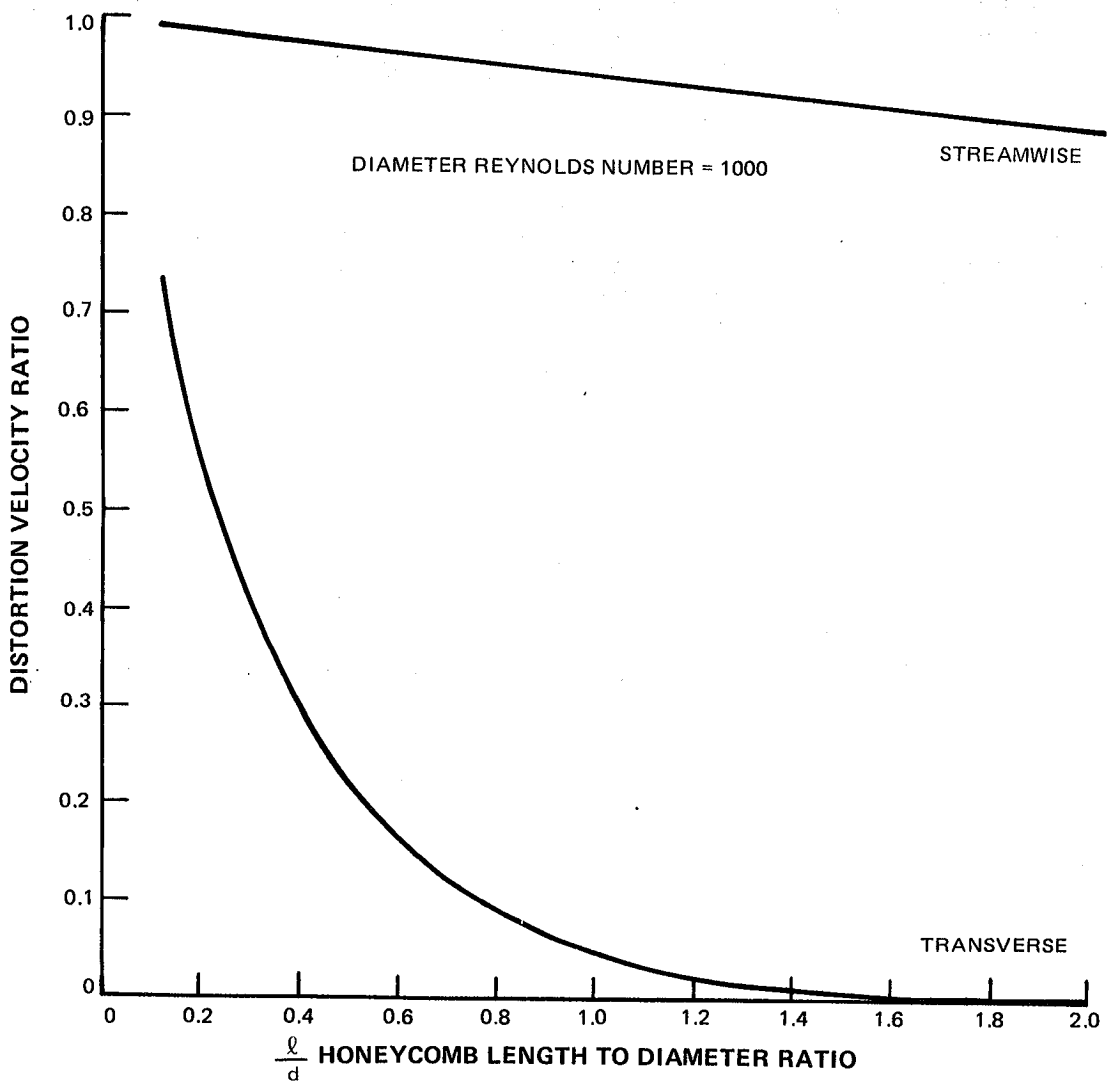

Figure 37 The distortion attenuation characteristics of honeycomb.

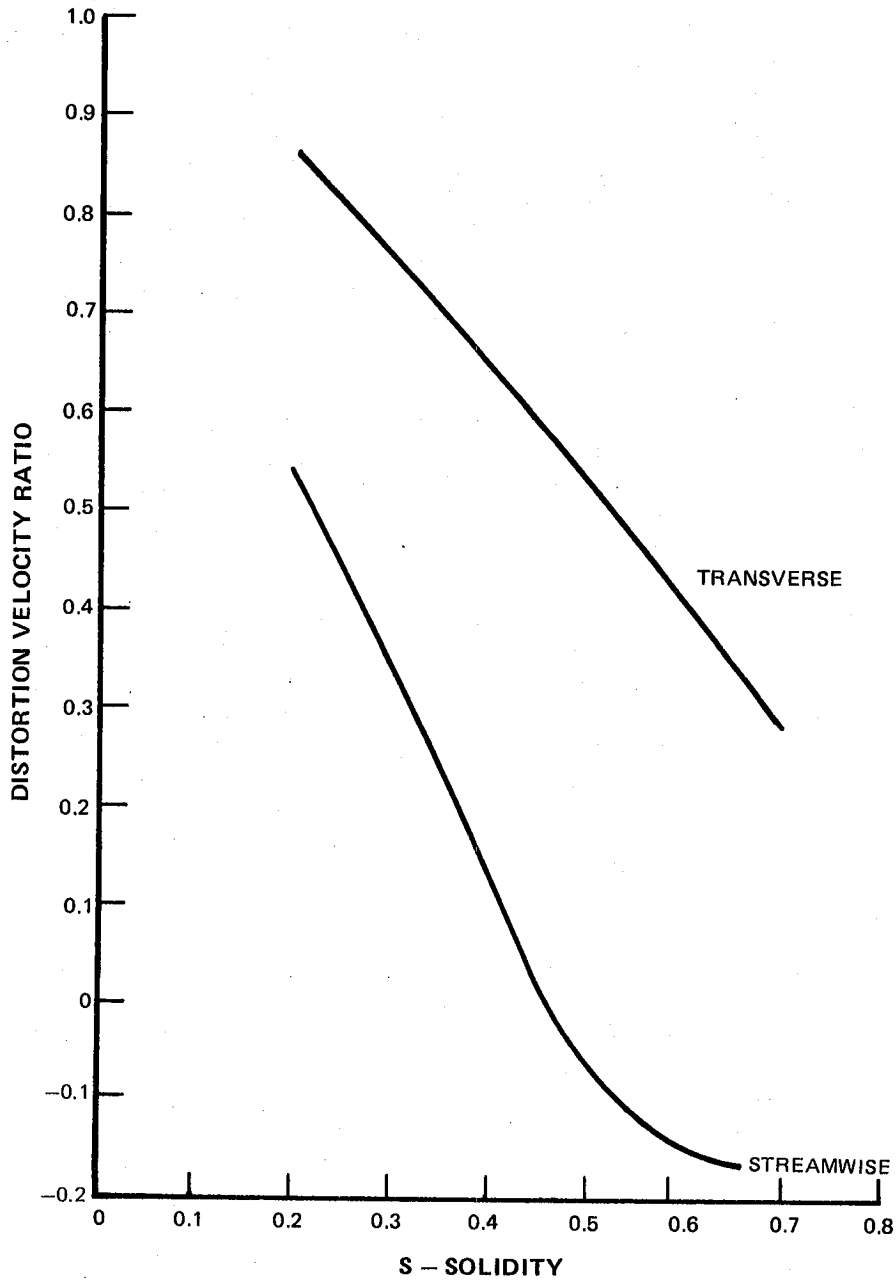

Figure 38 The distortion attenuation characteristics of perforated plate.

10.0 THE ACOUSTIC TRANSMISSION LOSS OF AN INFLOW CONTROL SCREEN (PHASE II TASK E)

10.1 Introduction

The inflow control screen mounted upstream of the inlet constitutes an obstruction to the acoustic radiation from the engine inlet. The nature of this obstruction and its effect on the radiation field are determined by the geometrical and structural chacteristics of the screen together with the mean throughflow, and the incident sound field. The effect of this obstruction is to produce a reflected field on the source side of the screen in addition to the incident field, and on the opposite side of the screen, a transmitted field. The interaction of the sound field and the screen is very complex and the problem has not, in general, been solved. Fortunately, if certain assumptions are made that are reasonable for some practical situations, the problem becomes tractable.

The first assumption is that the wavelength of the incident field is large compared to the screen aperture size. Secondly, the number of apertures per unit area is assumed sufficiently large and uniformly distributed so that at some small distance ϵ , on either side of the screen, the radiation impedance is constant. (Figure 39)

The consequence of the first requirement is that the pressure is in phase over the aperture and thus the particle velocity of the fluid in the aperture is approximately normal to the screen plane. This leads to the view of a "locally reacting" screen, the characteristic of which is that in the vicinity of the screen for any given condition, the pressure and particle velocity at a point on one side are solely related to those quantities at the corresponding point on the opposite side (Figure 39). The second assumption provides a plane on either side of the screen containing all of these points and thus the acoustic characteristics of the screen can be defined in terms of the radiation impedance at the ϵ planes; i.e., two complex numbers. In addition, the locally reacting screen assumption, leads to the deduction that the form of the transmitted field is the same as that of the incident sound field, its amplitude and phase being different. A further reasonable assumption is commonly made for transmission through thin screens, namely, that the wavelength of the incident field is large compared to the screen thickness. The screen is thus assumed to be acoustically thin. In this situation the pressure is approximately in phase through the screen and the fluid moves as a solid body in the aperture. When this occurs, the continuity equation provides a relationship between the particle velocities at the ϵ planes (they are equal in amplitude and phase) and the acoustic character of the screen is conventionally described in terms of a single quantity, the screen impedance.

$$\frac{p_{1\epsilon} - p_{2\epsilon}}{u_1}$$

In view of the wide-spread use of perforated plate as a lining material much work has been done on the impedance on this type of structure. The dependance of the impedance on the various pertinent parameters, i.e., flow, incident sound level and screen geometry has been examined. Invariably a single orifice has been examined (54), (55) from which using the second and third assumptions the screen impedance is readily deduced. The most commonly considered flow condition has been a grazing flow since this is encountered much in practice (56), (57). However, Ingard and Ising (54) among others, have made measurements of the impedance of orifices in the presence of normally incident flow. Their measurements of the resistive component of the impedance indicate, above a certain flow speed, a linear dependance on that quantity. This lends weight to the view that in this region the acoustic pressure loss is due to the same mechanism (jetting) as the mean pressure loss and can thus be determined from the pressure drop coefficient. At speeds approaching and including zero, the viscous dissipation in the acoustic boundary layer controls the resistance term. The reactive component, they found, is approximately the same as the no-flow value at low speeds. It should be noted that the reactive part of the impedance is determined by the inertia of the air in the holes, and since the air adjacent to the screen at the apertures is also carried along, there is an additional contribution to the inertia that must be accounted for. These so called end corrections are thus apparently unchanged by a low incident throughflow, in contrast to the situation of a grazing flow in which the attached air mass is blown away at very low flow speeds (56).

For honeycomb, the large wavelength to cell depth requirement may or may not be satisfied. In the former situation the acoustically thin screen approach is directly applicable provided the current screen impedance is determined. If the wavelength is not large compared to the cell depth the flow in the cell may no longer be considered incompressible. However, the "locally reacting" phenomenon leads to the notion that the field propagates through the cells as plane waves and this observation allows the problem to be solved.

On the test stand for engines in the size range of the JT9D and JT15D it is anticipated that the screen design will be such that the assumption of a locally reacting and acoustically homogeneous screen will be appropriate.

10.2 Theory

For the full scale test situation it is anticipated that the screen will be in the acoustic far field of the engine for a substantial part of the frequency range of interest. For the JT9D engine this criterion is satisfied for frequencies above roughly 1000 Hz if the screening is 1.5 diameters away. For the JT15D with the screening located at the same number of diameters away, the far field criterion is satisfied only above around 3500 Hz. Furthermore in most ICS designs, the screen elements are far enough from the source that the incident sound field

may be represented by a summation of plane waves and thus, in view of the linearity of the acoustic fields being examined, it is sufficient to solve the problem for one incident plane wave only. This is done for the acoustically thin screen (perforated plate) and also for honeycomb. The assumption of locally reacting homogeneous screens is, of course, also made.

10.2.1 The Acoustically Thin Screen (Perforated Plate)

For a normally incident flow (Figure 40) the convected wave equation is satisfied on both the upstream and downstream side of the screen by plane waves of form

$$\phi = P e^{i(\underline{k}\cdot\underline{r} - \omega t)} \tag{73}$$

The corresponding particle velocity field is

$$u = u e^{i(\underline{k}\cdot\underline{r} - \omega t)} \tag{74}$$

With, in particular, the magnitude of the component in the x-direction being given as,

$$u_1 = \pm \frac{\cos\theta}{\rho c}\phi \tag{75}$$

The sign depending on the direction of wave propagation. The acoustically thin screen assumption, which implies that the fluid between the ϵ planes is incompressible, allows the normal particle velocities on these surfaces to be equated.

$$(u_{1E} + u_{1R})_{\epsilon_1} = (u_{1T})_{\epsilon_2} \tag{76}$$

$$\text{AND } k\Delta \doteq 0$$

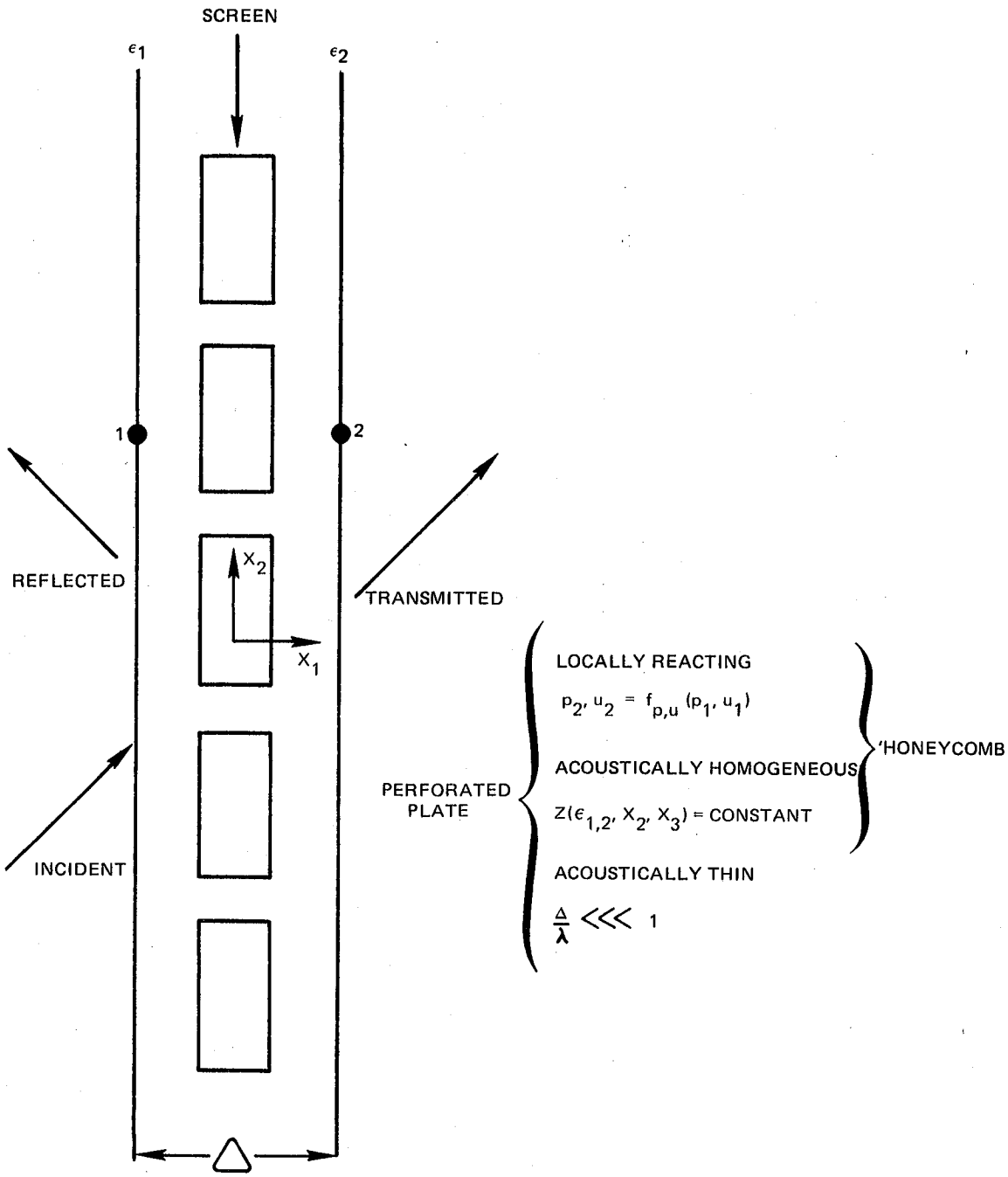

Figure 39 The assumptions for the screen transmission loss analysis.

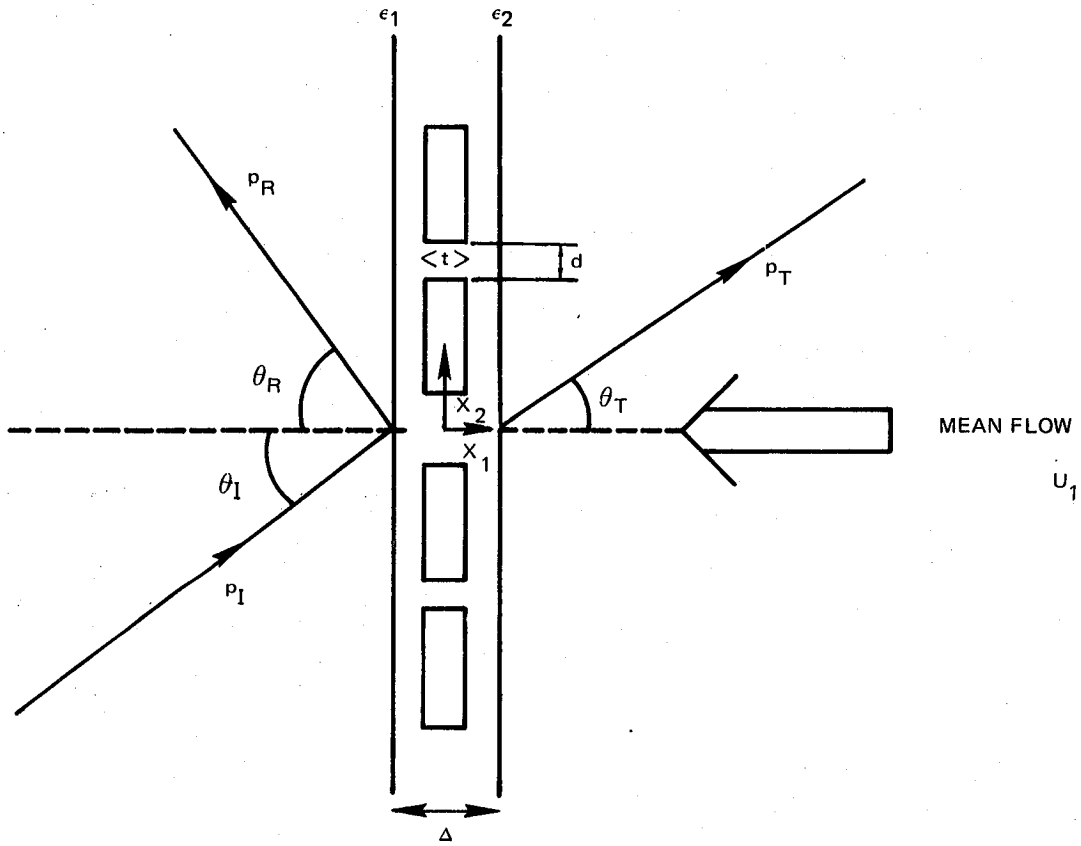

Figure 40 The perforated plate geometry.

The locally reacting screen produces a relationship between transmitted and incident fields so that

$$\theta_I = \theta_T \tag{77}$$

The matching of the trace wavelength on the incident ϵ plane for the reflected and incident waves together with the constant value of frequency in these two fields leads to

$$\frac{1 + M\cos\theta_I}{\sin\theta_I} = \frac{1+M\cos\theta_R}{\sin\theta_R} \tag{78}$$

Finally the acoustic pressure balance between the ϵ planes yields

$$P_I + P_R = P_T + \tilde{Z}_s\, u_{1T} \tag{79}$$

Where $\tilde{Z}$ is the screen impedance $\frac{\Delta p}{u_1}$

Solving these equations simultaneously allows expressions for the transmission and reflection coefficient to be found.

$$\frac{P_R}{P_I} = \frac{\frac{\tilde{Z}_s}{\rho c}\cos\theta_I}{(1+A)+A\frac{\tilde{Z}_s}{\rho c}\cos\theta_I} \tag{80}$$

and

$$\frac{P_T}{P_I} = \frac{1+A}{(1+A)+A\frac{\tilde{Z}_s}{\rho c}\cos\theta_I} \tag{81}$$

where

$$A = \frac{-M+T\sqrt{T^2+M^2-1}}{(M^2+T^2)\cos\theta_I} \tag{82}$$

$$T = \frac{1+M\cos\theta_I}{\sin\theta_I}$$

For the limiting case when $M \ll 1$ which corresponds to the situation at inflow control structures, $A \Omega \sec \theta_I$. The normally incident wave is attenuated most and this occurs when $\theta_I = 0$. Incorporating these two conditions into Equation 81 and taking the absolute value of the transmission coefficient

$$\left| \frac{P_T}{P_I} \right|^2_{MAX} = \frac{4}{\left(2 + \frac{R}{\rho c}\right)^2 + \frac{X^2}{\rho^2 c^2}} \tag{83}$$

where Z_2 has been replaced by $R + iX$.

Now if the resistance is due to jetting then

$$R = \rho K U_1 \tag{84}$$

and from Ingard and Ising the reactive component may be written

$$X \cong \frac{\rho \omega (\ell + \delta)}{\sigma} \tag{85}$$

Those authors note that the end correction δ varies from .85d to zero as the open area ratio σ goes from high to low solidity. This expression becomes increasingly in error as the limits of σ are reached. However, in the mid solidity range δ may be approximated by $(1 - \sigma)d$, thus Equation 85 becomes

$$X \cong \frac{\rho \omega \left[\ell + (1 - \sigma) d \right]}{\sigma} \tag{86}$$

substituting the expressions for R and X in Equation 83 produces

$$\left| \frac{P_T}{P_I} \right|^2_{MAX} = 4 \left\{ (2 + KM)^2 + \frac{\omega^2}{c^2 \sigma^2} \left[\ell + (1 - \sigma) d \right]^2 \right\}^{-1} \tag{87}$$

if

$$\frac{K}{2} = O(1), \quad \text{then } KM \ll 2$$

and

$$\left|\frac{p_r}{p_I}\right|^2_{MAX} = \left\{ 1 + \frac{\pi^2 f^2}{c^2 \sigma^2} \left[\ell + (1-\sigma) d \right]^2 \right\}^{-1} \qquad (88)$$

This transmission loss expression is plotted in terms of dB for a 50% open area screen in Figure 41. In Figure 42 the loss as a function of frequency is shown for the perforated plate used in the JNRP developed inflow control screens. The perforated plate having 51% open area, .3cm thick and with .47cm diameter holes has significant transmission loss at the higher frequencies while the perforated plate having 46% open area, .08cm thick and with .16cm diameter holes has a loss less then 1 dB at all frequencies of interest. Even though these curves show that normal incidence transmission characteristics, the range of incidence angles encountered in practice will not materially alter these curves.

If the criterion for a perforated plate is that the transmission loss must be less than 1 dB at all frequencies, and if the maximum frequency of interest is 10 kHz, Equation 88 leads to

$$\frac{\ell + (1-\sigma) d}{\sigma} < .55 cm. \qquad (89)$$

This expression is subject to the constraints of the analysis and the range over which the reactance expression is valid. The honeycomb presents a different problem for invariably it cannot be considered acoustically thin over the frequency range of interest.

10.2.2 The Acoustically Thick and Low Solidity Screen (Honeycomb)

The honeycomb screen problem, while it can be formulated in terms of the radiation impedances at its surfaces, is not particularly illuminated by this approach. The assumption of a locally reacting acoustically homogeneous screen results in the sound field propagating through the honeycomb cells as plane waves. In addition the low mean flows encountered in practice by these screens produce an angle of reflection that is equal, to a good approximation, to the angle of incidence (Figure 43). Viscous effects will be ignored in view of the low pressure drop coefficient and a single reflection only will be assumed to occur in the honeycomb cells.

The plane waves in the incident and reflected fields are of the form

$$\phi = p e^{i(\underline{k} \cdot \underline{r} - \omega t)} \qquad (90)$$

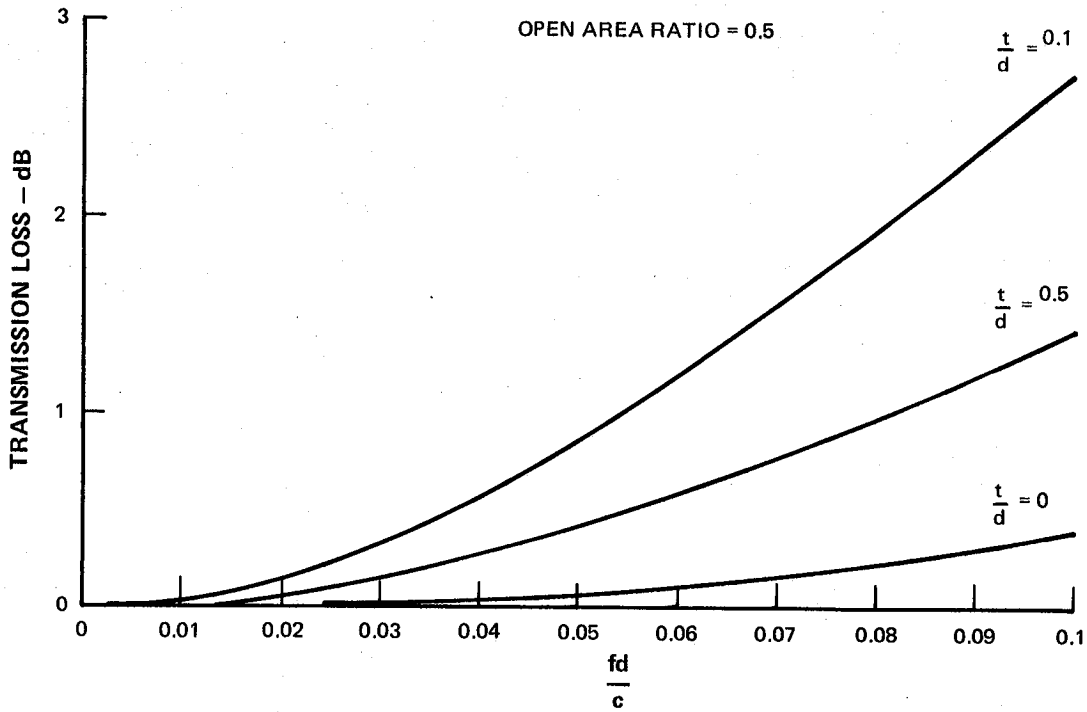

Figure 41 Perforated plate transmission loss.

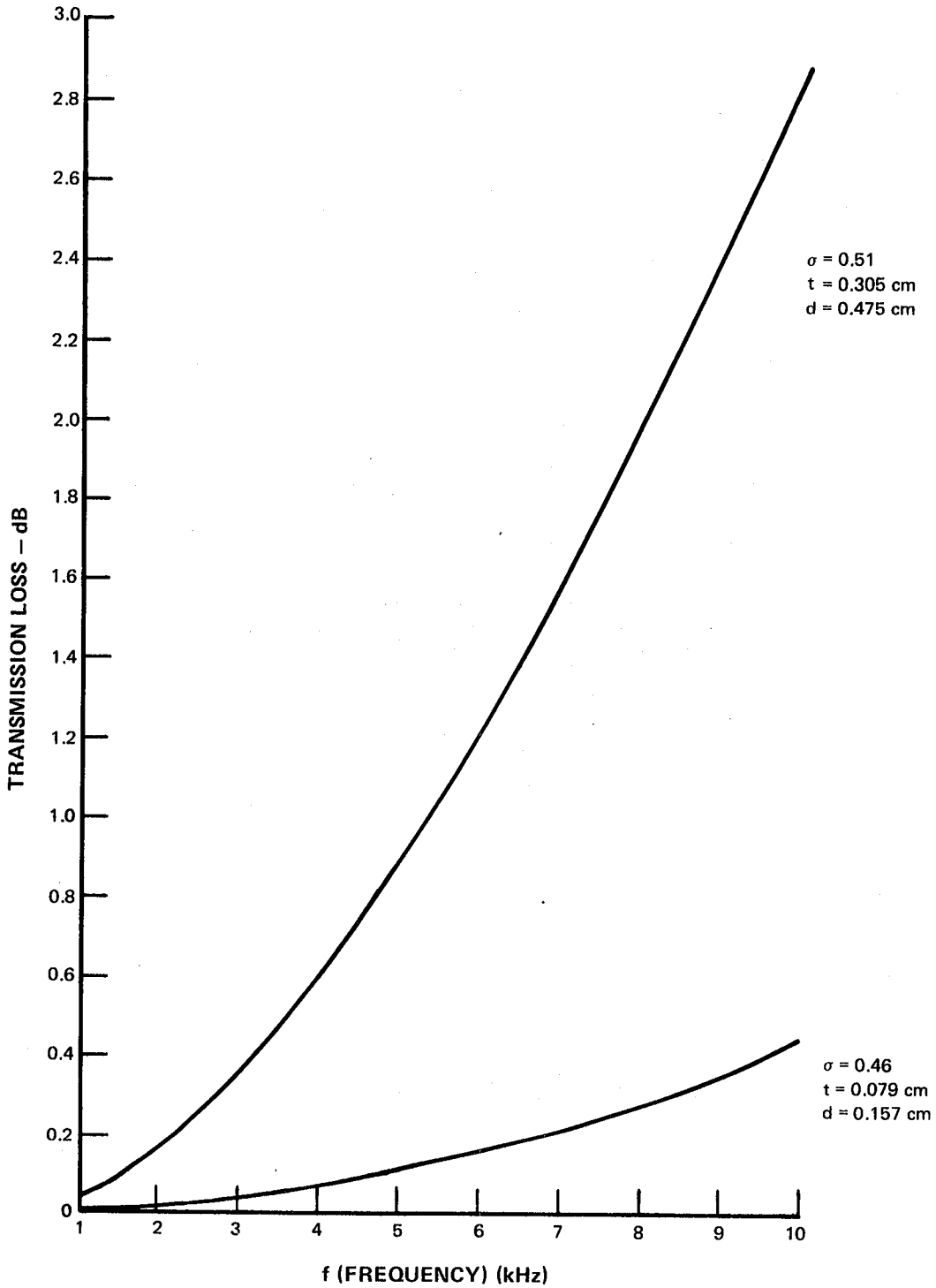

Figure 42 The transmission loss of JNRP developed perforated plate.

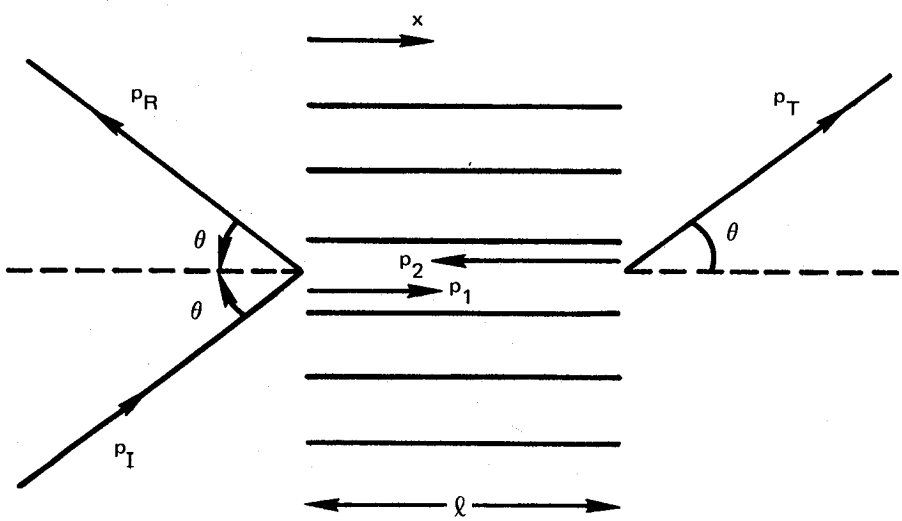

Figure 43 The honeycomb geometry.

with axial components

$$u_1 = \pm \frac{\cos\theta}{\rho c} p \tag{91}$$

The transmitted wave while of the same form is displaced by some phase that at this point is unknown and hence that pressure field can be represented by

$$p_T = p_T e^{-i\omega t} \tag{92}$$

where p_T is complex.

In the honeycomb cells, the waves are of the form

$$p = p e^{i(k_1 x - \omega t)} \tag{93}$$

$$u_1 = \pm \frac{p}{\rho c} \tag{94}$$

Now at the ends of the honeycomb (which correspond very closely to the ϵ planes) both acoustic pressure and normal velocity fields must match and so at $x_1 = 0$

$$p_I + p_R = p_1 + p_2 \tag{95}$$

$$p_I \cos\theta - p_R \cos\theta = p_1 - p_2 \tag{96}$$

At $x_1 = \ell$

$$p_1 e^{ik_1\ell} + p_2 e^{-ik_1\ell} = p_T \tag{97}$$

$$p_1 e^{ik_1\ell} - p_2 e^{-ik_1\ell} = p_T \cos\theta \tag{98}$$

These four equations are in five unknowns and thus can be solved simultaneously for the transmission and reflection coefficient

$$\left|\frac{P_R}{P_I}\right|^2 = \frac{\sin^4\theta \sin^2 k_1 \ell}{4\cos^2\theta + \sin^4\theta \sin^2 k_1 \ell} \qquad (99)$$

$$\left|\frac{P_T}{P_I}\right|^2 = \frac{4\cos^2\theta}{4\cos^2\theta + \sin^4\theta \sin^2 k_1 \ell} \qquad (100)$$

In the angle of incidence range encountered by the inflow control structures this transmission coefficient is effectively unity for all frequencies. As for the perforated plate this observation is qualified by the assumptions on which the analysis rests.

10.3 Conclusions

The experience for the acoustic transmission loss of perforated plate type and honeycomb type screens that are presented here are

$$TL = 10 \log \left\{1 + \frac{\pi^2 f^2}{c^2 \sigma^2}\left[\ell + (1-\sigma)d\right]^2\right\}$$

for perforated plate

$$TL = 10 \log \left\{1 + \frac{\sin^4\theta \sin^2 k_1 \ell}{4\cos^2\theta}\right\}$$

for honeycomb.

At the low mean flow speeds to which an inflow control structure is exposed the honeycomb is acoustically transparent and perforated plate has a transmission loss that is controlled by the reactance of the screen. In view of the frequency dependance of the perforated plate reactance, significant transmission loss can occur at the higher frequencies.

11.0 THE DIRECTIVITY EFFECTS OF SCREEN COMPONENTS (PHASE II TASK)

11.1 Introduction

While the transmission loss associated with both honeycomb and gauze type screens can be confined to 1 dB, the structure supporting the panels can provide some modification of the radiation field. In fact, any discontinuity in the inflow control screen will cause some change in the directivity pattern of the source. Ideally, the screens should be constructed such that discontinuities do not exist, but within the constraints imposed when operating on a test stand, this is not possible although the inflow control structures designed and built under the JNRP come pretty close to the ideal in this respect. Other smaller scale screens (27, 28, 29, and 31) also exhibit a minimal amount of discontinuity in their structure.

In structures where there are significant discontinuities in the profile, caused by either support structure or the intersection of honeycomb sections, some modification to the radiation field is anticipated. The magnitude and extent of the directivity change is dependent on the source, so that different sources radiating through the same screen will experience different directivity changes. In general, then, an engine operating at different conditions will produce radiation fields that are modified differently by the screen at each condition. The model developed in this section is of a simple source radiating through a corner between two adjacent honeycomb panels. The accuracy of this model is determined by comparison with measurements made of the phenomenon.

11.2 The Model

The model described here will be used to predict the effects on acoustic directivity patterns of ICS honeycomb panel intersections. This model may also be used to determine the effect of structural members on the sound field, however, the present discussion is confined to a honeycomb corner.

The source of sound at the test stand is, of course, the engine, and since the size of this source is not small compared to the distance to the screen, the source cannot be considered to occur at a point. If however, this source can be represented by a distribution of simple sources and if further the wave equation governs the propagation, then the resultant radiation field may be constructed by superposition of the radiation fields due to each source. Now, by the time a wave emitted from one of these sources reaches a corner, its radius of curvature is large compared to a typical corner dimension and therefore may be considered locally plane. Furthermore, as noted in Section 11, if the wavelength of the wave is large compared to the honeycomb cell size, the wave propagates through each cell as a plane wave, then reforms on the other side as a wave whose direction is unchanged, Figure 44.

Consider now a field point that receives significant contributions to the fluctuating pressure level through each of the adjacent panels. Usually, the source will not lie on the line of symmetry of the corner, and so rays passing through the adjacent panels will travel along different paths, with different path lengths to reach the field point. The two rays will consequently interfere with each other after they have passed through the honeycomb structure (Figure 44) (N.B. for simplicity, Figure 44 shows the source and field point lying in a plane normal to the corner panels). In general, this is not the case. The nature of the interference depends on the source signal for a given geometry and for linear radiation, it is sufficient to solve the problem of a point monopole radiating at a single frequency. More complex sources can be determined by superposition.

The phenomenon that will be modelled is then the interference effects experienced in the far field of a monochromatic source due to the presence of a honeycomb corner. The model chosen is shown in Figure 45 (N.B. again, as in Figure 44, for simplicity, both source and field point are shown lying in a plane normal to the corner panels, the model is not limited to this case). It is three dimensional. It consists of two parallel semi-infinite and totally reflecting planes, on the opposing sides of which are two simple sources of the same frequency. The distance between the planes is related to the blockage of the corner. The phase relationships of the two sources is determined by the path length difference of the waves passing through the adjacent panels. The distance of the sources from the plane boundary is the distance from the source to the corner.

The model then, exhibits all the important characteristics of the phenomenon.

To find the solution to this problem, a look at the diffraction pattern for a single source and plate is beneficial (Figure 46) because the two plate solution may be constructed from the single plate solution, by super-position, in view of the linearity of the problem.

The solution is presented by Bowman, Senior and Uslenghi in (58) and is given for the velocity potential at the field point (R,Φ).

$$\psi(R,\Phi) = 2_i \int_{-m}^{\infty} \frac{H_1^{(1)}(\mu^2 + kR)}{(\mu^2 + 2kR)^{1/2}}\, d\mu \qquad (101)$$

where

$$m = \pm\sqrt{k(R_1 - R)}$$

$+ve$ for $0 < \Phi \leq \pi$

$-ve$ for $0 \geq \Phi \geq -\pi$

This expression may be simplified (Appendix F) by requiring that

$$2\xi_0 \ll R, \quad kR \gg 1$$

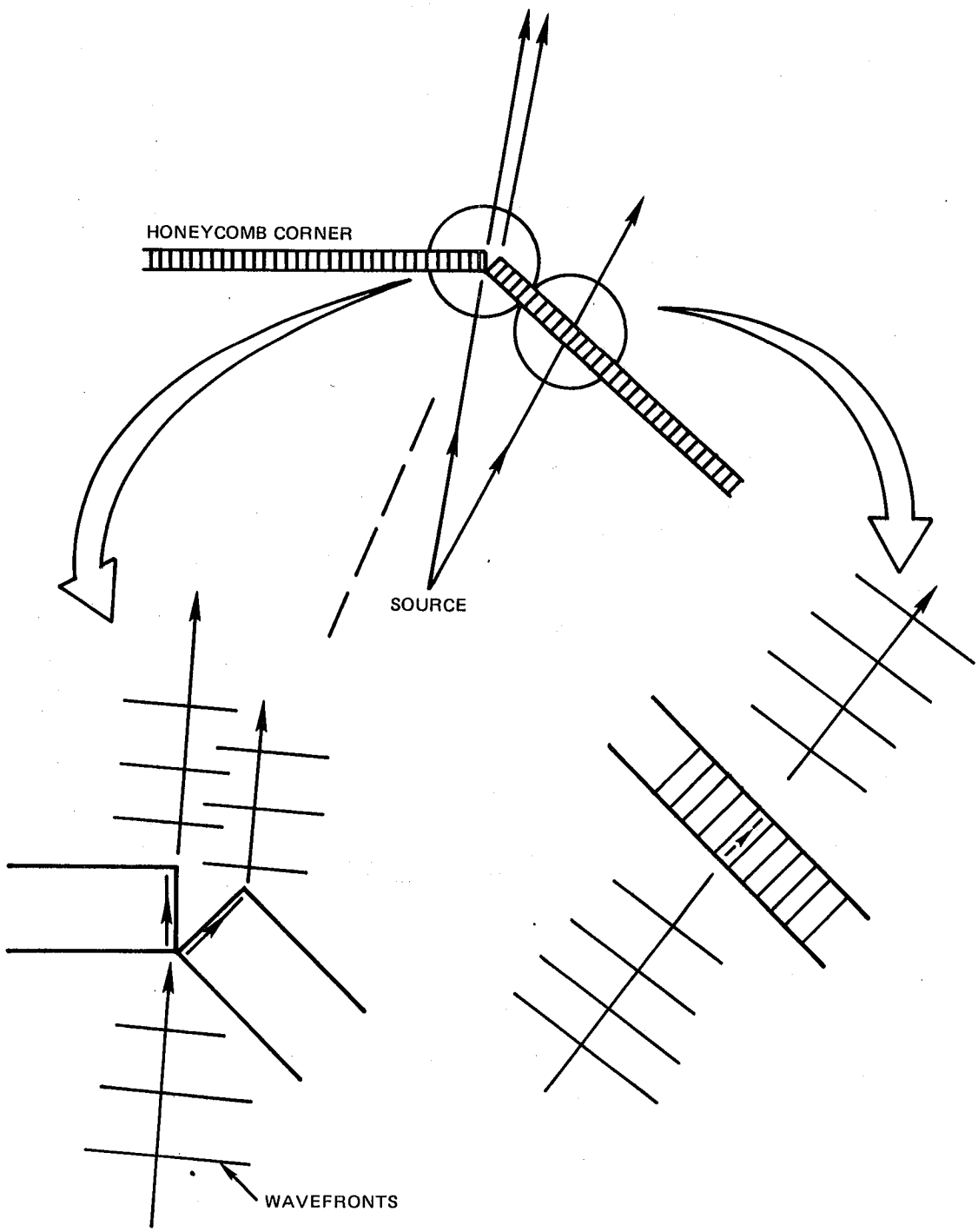

Figure 44 Interference and transmission effects in honeycomb.

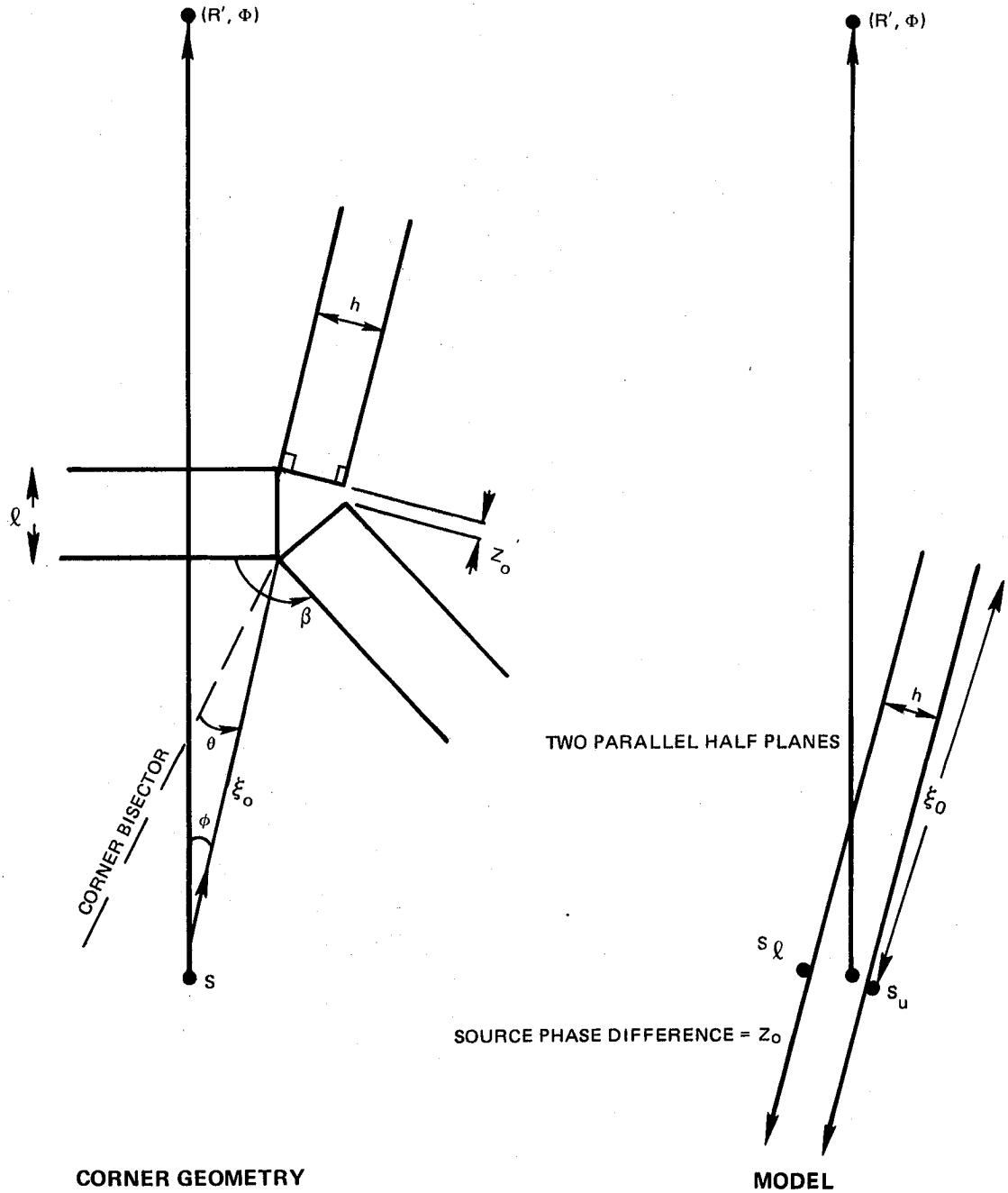

Figure 45 The diffraction model.

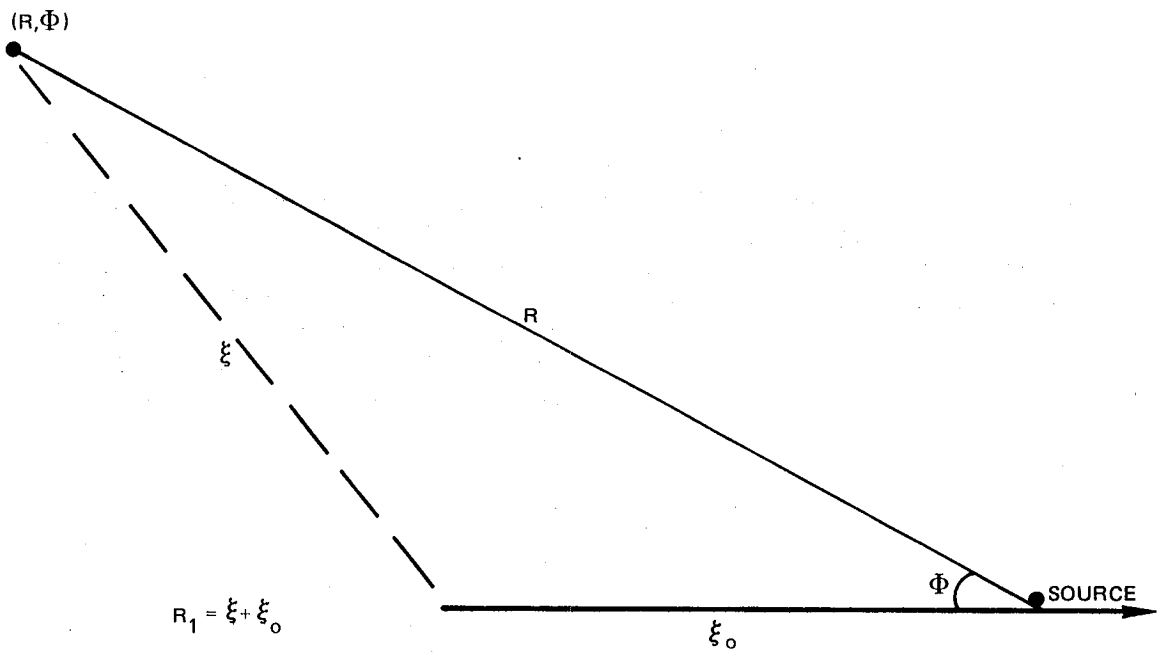

Figure 46 A point source on a semi infinite plane.

(The validity of these and subsequent assumptions in this section will be examined in Section 11.4).

A simple expression for the velocity potential can be obtained in terms of Fresnel integrals and is

$$\psi(R,\Phi) = \frac{\sqrt{2}}{2kR} \exp\left[i\left(kR - \frac{\pi}{4}\right)\right]\left\{\left(\frac{1}{2} + C\right) + i\left(\frac{1}{2} + S\right)\right\} \tag{102}$$

The Fresnel integrals C and S, are functions of m, which for a fixed value of R and ξ means that they are functions only of the field point angular position Φ and the coordinate along the corner z. The expressions for them are

$$C = \int_0^{\frac{\sqrt{2}}{\pi} m} \cos\left(\frac{\pi}{2}\tau^2\right) d\tau$$

$$S = \int_0^{\frac{\sqrt{2}}{\pi} m} \sin\left(\frac{\pi}{2}\tau^2\right) d\tau \tag{103}$$

Now noting that the intensity in the far field is proportional to the square of the amplitude of the velocity potential (i.e. $\Psi\,\Psi^*$), the intensity can be written as shown in Equation 104, and may be plotted as a function of Φ for a given R, ξ_0 and z. A typical shape is shown in Figure 47. In general the shadow is not sharp edged and the boundary is characterized by a diffraction pattern with interference fringes on the source side of the plane. This shape is due to the Fresnel integrals.

$$\text{Intensity} \propto \frac{1}{k^2R^2}\left[\left(\frac{1}{2} + C\right)^2 + \left(\frac{1}{2} + S\right)^2\right] \tag{104}$$

It is noted, that this form for the intensity is identical to that produced for the case of Fresnel diffraction around a half plane, (59). Apparently the $2k\xi_0 << kR >> 1$ constitutes a definition of Fresnel diffraction for this geometry.

Using the solution to the single plane problem the solution for the model, Figure 48, can be found, by superposition, and in terms of the velocity potential is

$$\psi_t = \frac{\sqrt{2}}{2k} e^{-i\frac{\pi}{4}}\left[\frac{e^{i(kR_u+\zeta)}}{R_u}\left\{\left(\frac{1}{2} + C_u\right) + i\left(\frac{1}{2} + S_u\right)\right\}\right. \tag{105}$$

$$\left. + \frac{e^{ikR_\ell}}{R_\ell}\left\{\left(\frac{1}{2} + C_\ell\right) + i\left(\frac{1}{2} + S_\ell\right)\right\}\right]$$

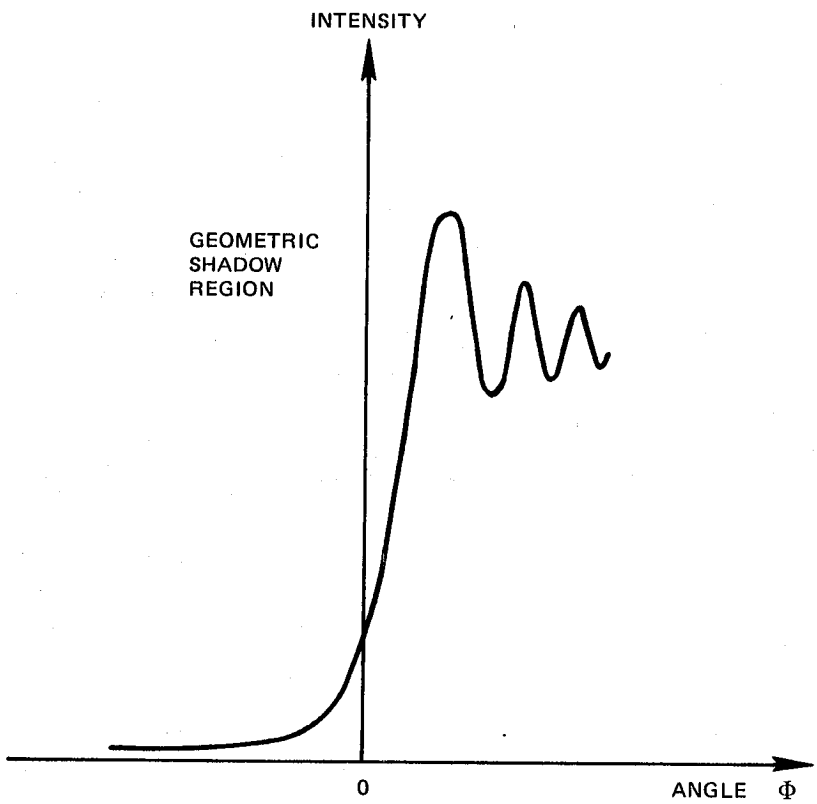

Figure 47 A typical diffraction pattern.

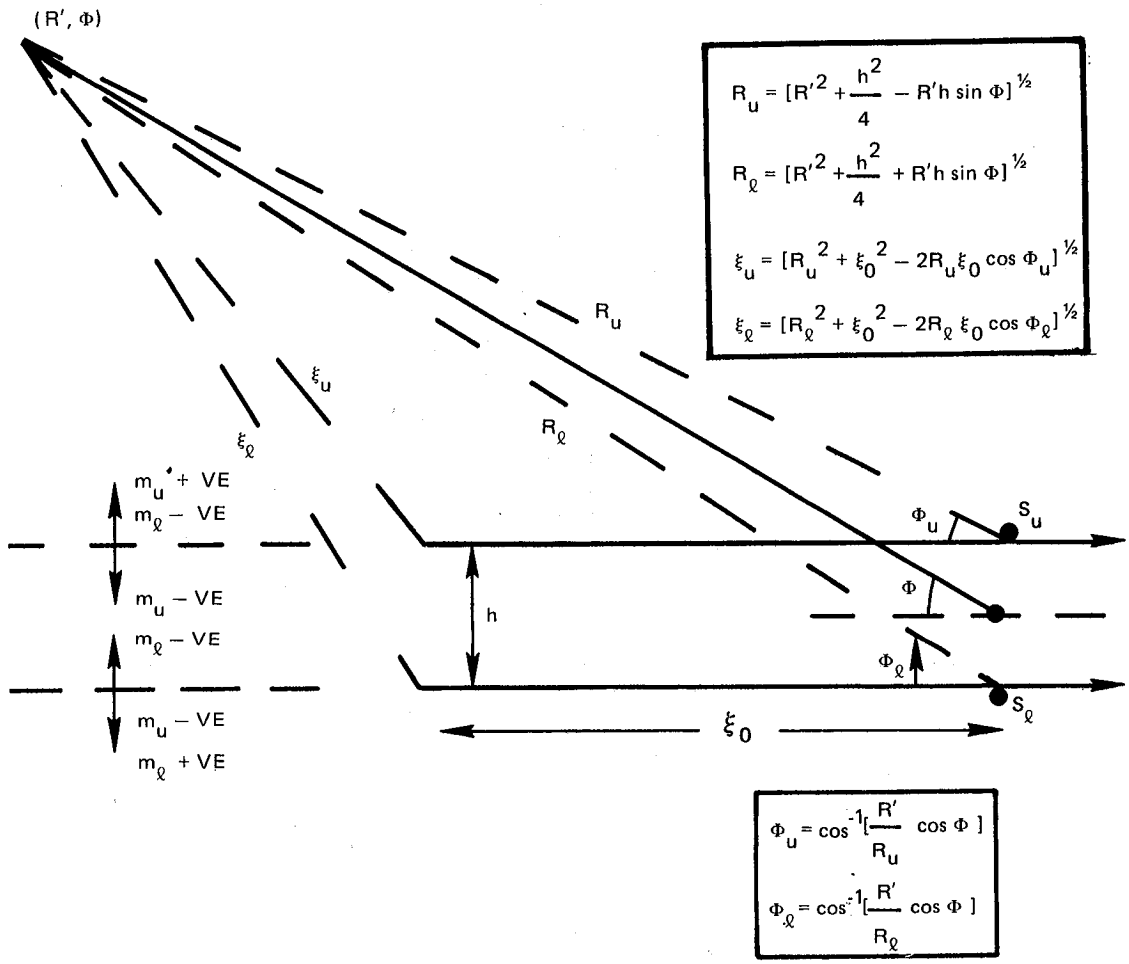

Figure 48 The geometry of the model.

The subscripts u,ℓ refer to the upper and lower sources, and ζ is the phase difference between the sources.

There are three distinct regions of the field - firstly, where m_u is $+ve$ and m_ℓ is $-ve$, corresponding to field points that are exposed to the incident fields of the upper source but in the shadow of the lower. The second regime is the converse, while the third consists of those positions in the geometric shadow of both (Figure 48). The intensity can thus be written, (within a constant) as

$$I_t \propto \frac{1}{k^2R_u^2}\left[\left\{\frac{1}{2}+C_u\right\}^2+\left\{\frac{1}{2}+S_u\right\}^2\right]$$

$$+\frac{1}{k^2R_\ell^2}\left[\left\{\frac{1}{2}+C_\ell\right\}^2+\left\{\frac{1}{2}+S_\ell\right\}^2\right]+ \tag{106}$$

$$\frac{2}{kR_uR_\ell}\left\{\left[\left(\frac{1}{2}+C_u\right)\left(\frac{1}{2}+C_\ell\right)+\left(\frac{1}{2}+S_u\right)\left(\frac{1}{2}+S_\ell\right)\right]\cos(k(R_u-R_\ell)+\zeta)\right.$$

$$\left.+\left[\left(\frac{1}{2}+S_u\right)\left(\frac{1}{2}+C_\ell\right)-\left(\frac{1}{2}+S_\ell\right)\left(\frac{1}{2}+C_u\right)\right]\sin(k(R_u-R_\ell)-\zeta)\right)$$

The first two terms are the separate contributions from each source, while the third and fourth are due to the interference between them.

In this expression all distances appear as a product with the wave number k. For ease of computation the field point is referenced to an origin halfway betwen the two sources and the relevant relationships are shown in Figure 48.

At this point, it is necessary to relate the parameters of the model to the geometry of the honeycomb corner. The plate separation, h and source phase difference ζ, may be determined from the geometry of Figure 45 in terms of the corner angle, β, honeycomb depth, ℓ, and incidence angle θ so that

$$h = 2\ell\cos\frac{\beta}{2}\cos\theta$$

$$Z_o = \frac{\zeta}{k} = 2\ell\cos\frac{\beta}{2}\sin\theta \tag{107}$$

There is an assumption implicit in the above expression for the phase factor; it is that ray tracing is valid for determining this factor. To quantify the range of validity, it is noted that geometric acoustic techniques are valid when $ka \gg 1$ where a is a characteristic dimension normal to the propagation direction. This is also the region in which scattering is referred to as diffraction. Since as noted previously, the model is a diffraction model, when the condition that ka be large is not satisfied, neither the phase calculation nor the use of the model is valid.

The intensity in Equation 106 is divided by a reference intensity and converted to dB. This process is described in the following section.

11.3 Comparison Between Experiment and Theory

As part of Phase II, Task F, measurements were made to determine the directivity effect of a honeycomb corner with a view to assessing the theoretical model. This test program was performed in an anechoic chamber at X-206 stand, Figure 49.

Briefly, a honeycomb corner was set up in the anechoic chamber and exposed to a driver .91cm feet away (Figure 50). An array of microphones at a radius of 15 feet was used to measure the transmitted sound field. The incident angle, θ , could be varied between 0^{o}, 5^{o}, and 10^{o}. The honeycomb was 7.62cm inches thick with an included angle of 135^{o} between panels. Cell size was .95cm in diameter. The source was driven at nominally, 2kHz, 5kHz, and 9kHz and was not omnidirectional in the angle range of interest. The corner was covered by tape in order to prevent sound leaking through it.

Two types of tape were used; a green cloth tape and an aluminum tape. No substantial difference was observed between data gathered from the two situations, except for the 2kHz case at 5^{o} incidence. Here it is conjectured that an inadvertant configuration change was made in the aluminum tape case (e.g., moving of absorbing material in the anechoic chamber).

The measured directivity patterns are shown in Figures 51 through 59. These were obtained by subtracting the levels obtained with the corner in place from those obtained without it. In general, the directivity changes increase with the frequency, indicating that the corner is more disruptive to the radiation field as the incident sound wavelengths decrease. In addition, there is, at the two higher frequencies, a local maximum in sound pressure level directly behind the corner as viewed from the source, at zero incidence there is no shadow zone behind the corner, the directivity patterns being seemingly arbitrary to the intuitive eye. These patterns are compared with those obtained from the model in these same figures.

To obtain directivity patterns from the model it was necessary to determine a reference level. This was done by observing that the interference occurred predominantly at a range of angles in the vicinity of the source - corner axis, and outside of this range the intensity levels were substantially constant. It was this constant level that was used as the reference (or corner removed) level.

In the table of Figure 60, two quantities are shown that provide an assessment of the model. The first is the mean difference between the measured and predicted directivity patterns. The second is the standard deviation of the measured data from the theoretical directivity pattern. These quantities are computed for each configuration and are used together with the comparisons of measured and theoretical predictions, shown in Figures 51 through 59 to provide the following assessment of the model.

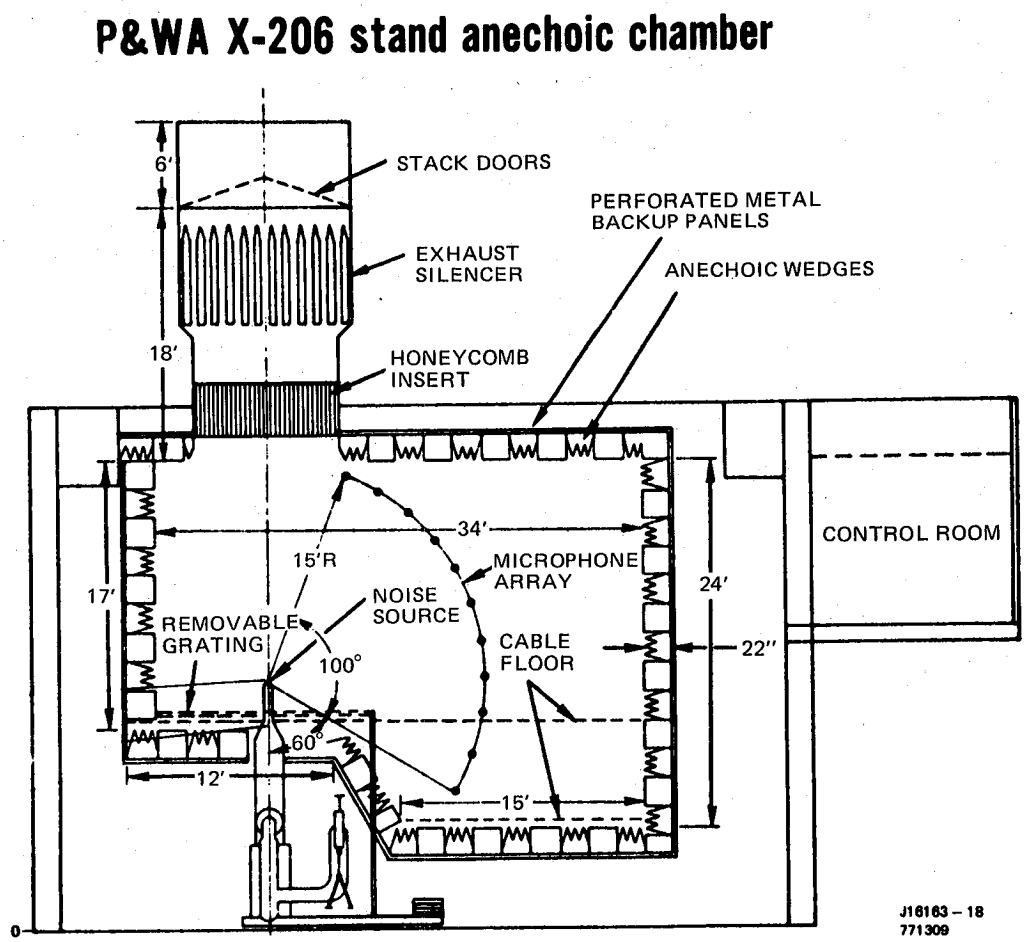

Figure 49 A schematic diagram of the anechoic chamber.

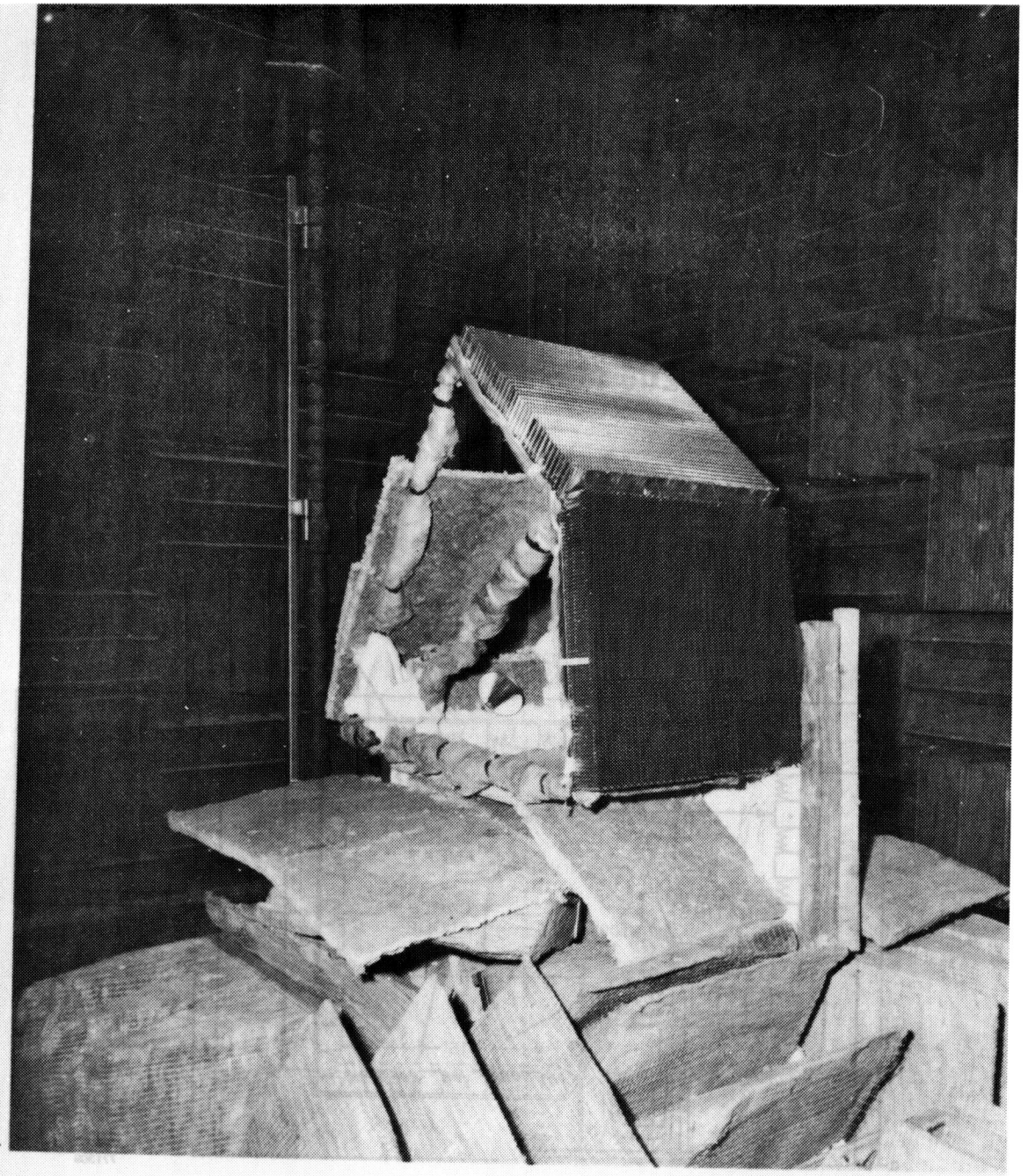

Figure 50 The test configuration.

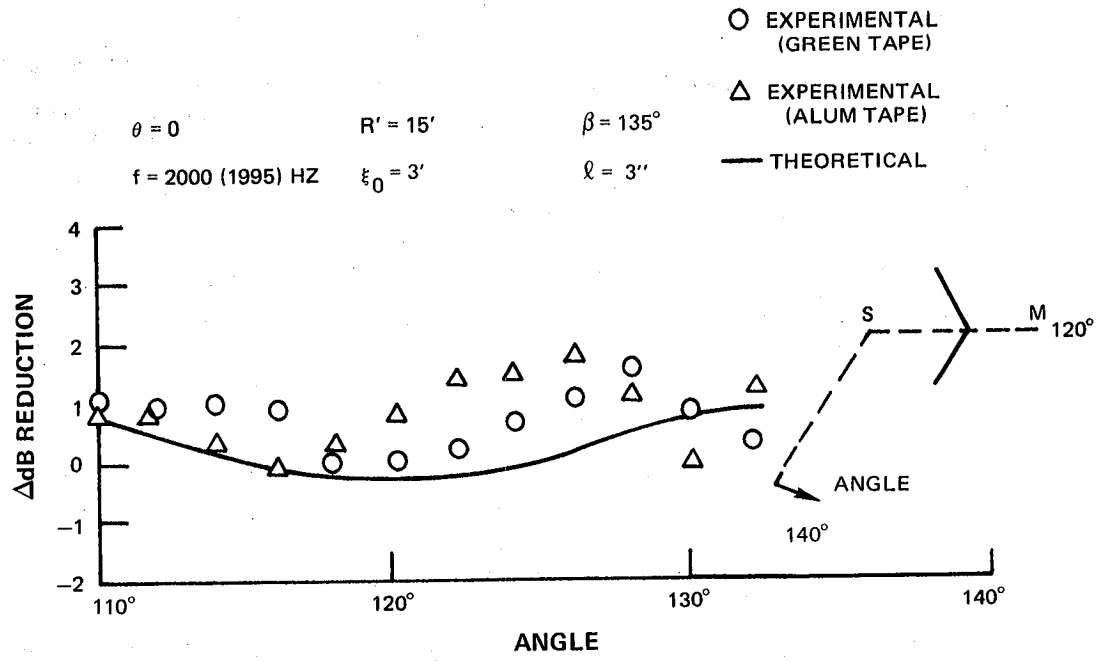

Figure 51 Diffraction at honeycomb corner comparison of measurement and prediction.

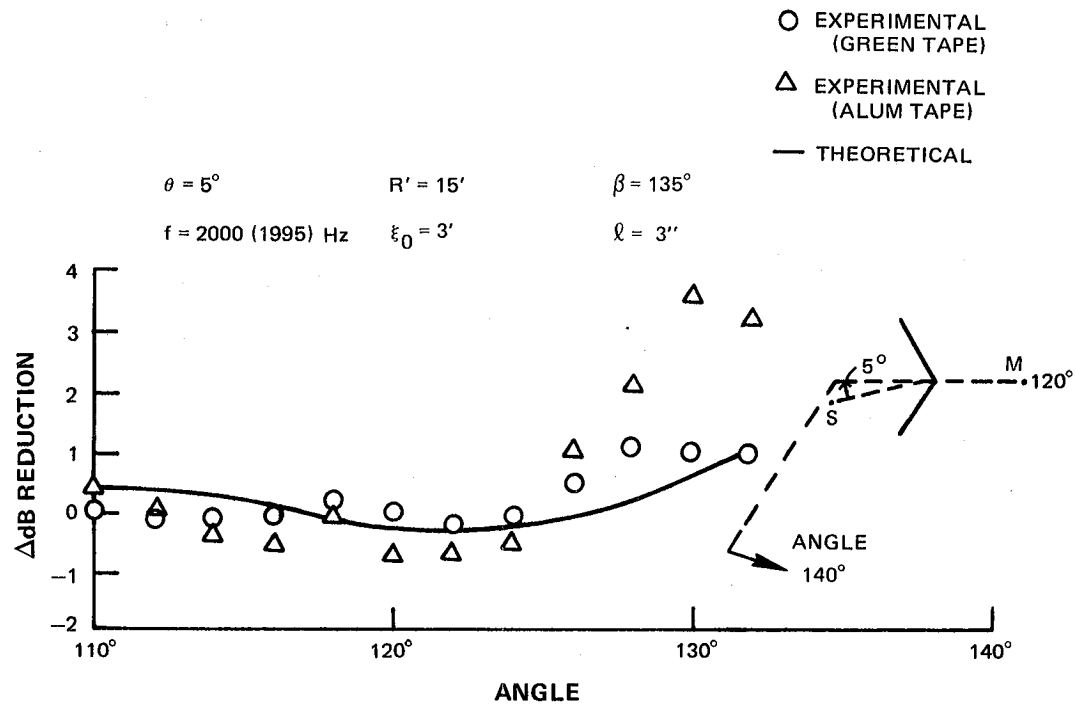

Figure 52 Diffraction at honeycomb corner comparison of measurement and prediction.

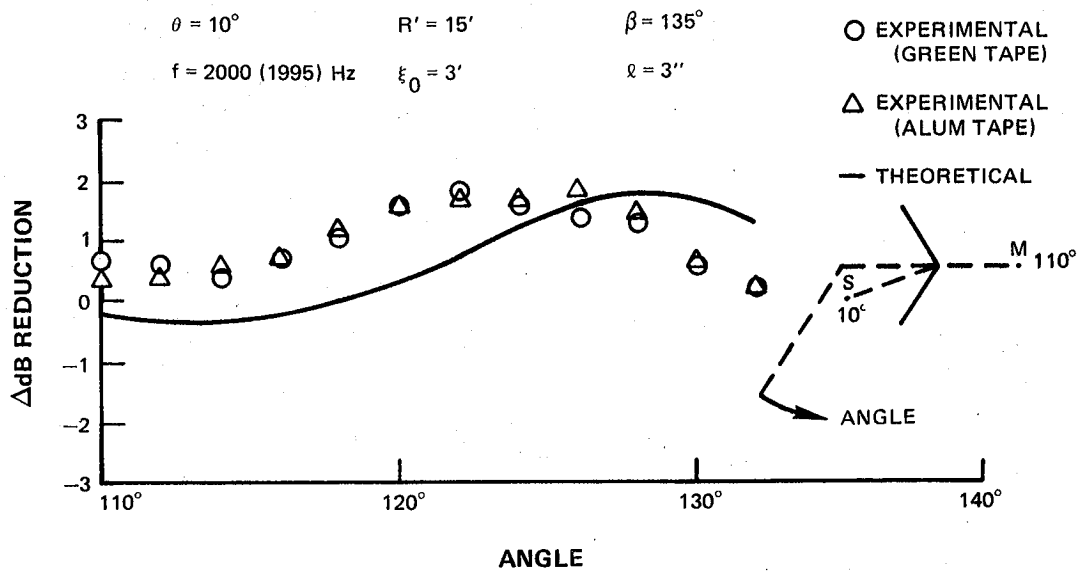

Figure 53 Diffraction at honeycomb corner comparison of measurement and prediction.

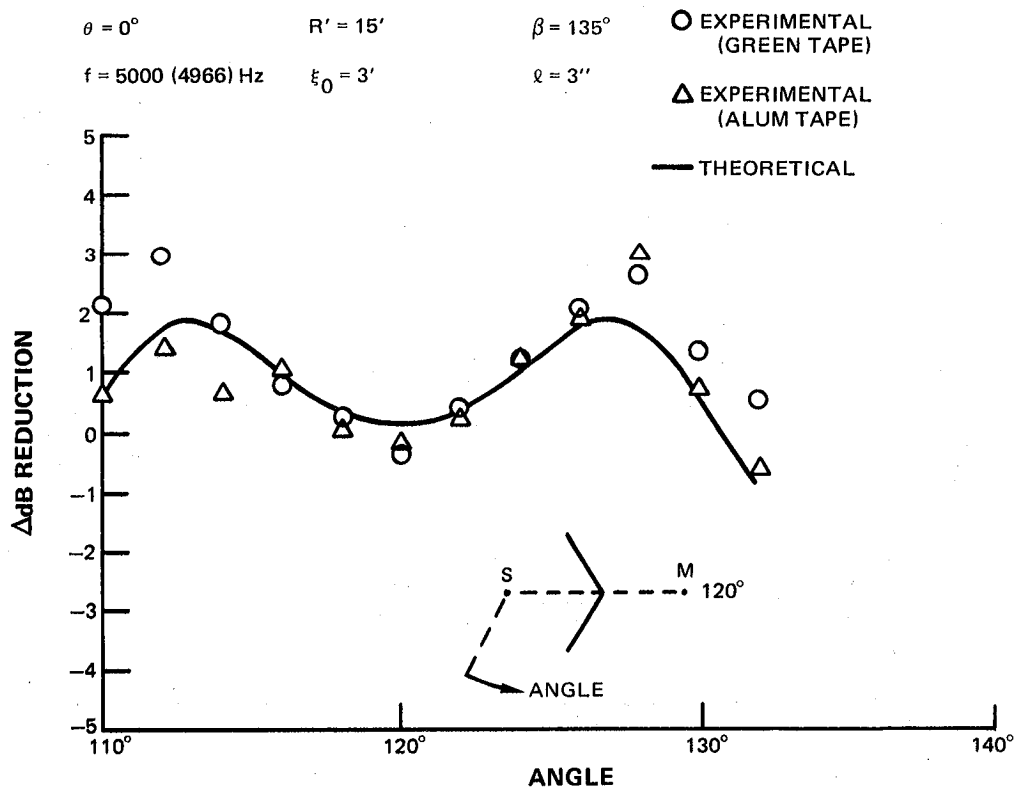

Figure 54 Diffraction at honeycomb corner comparison of measurement and prediction.

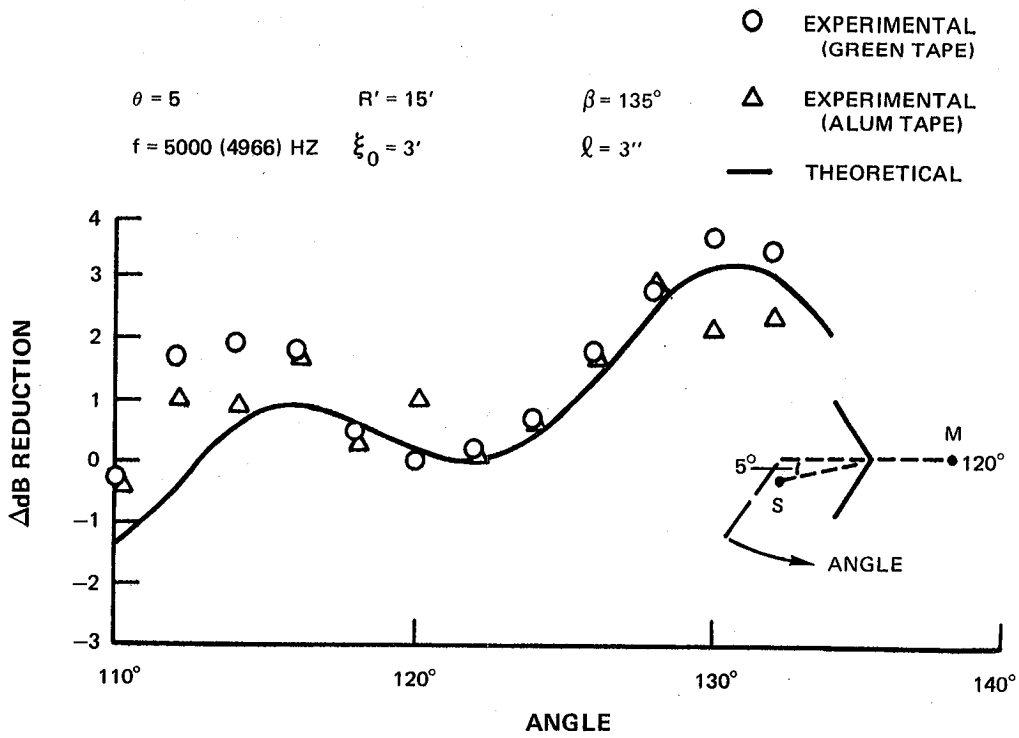

Figure 55 Diffraction at honeycomb corner comparison of measurement and prediction.

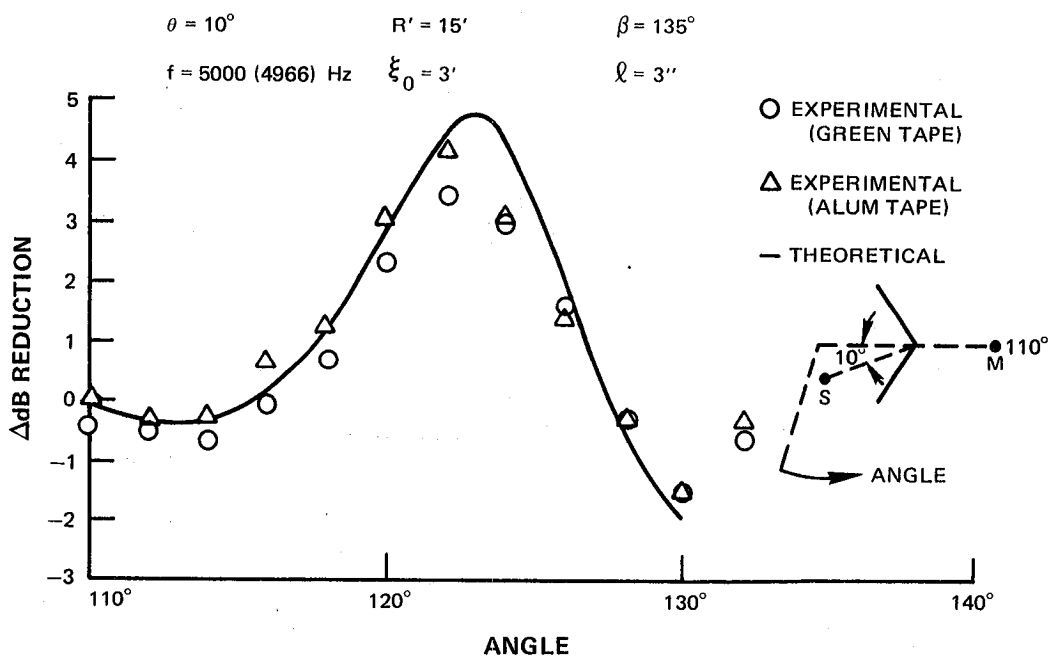

Figure 56 Diffraction at honeycomb corner comparison of measurement and prediction.

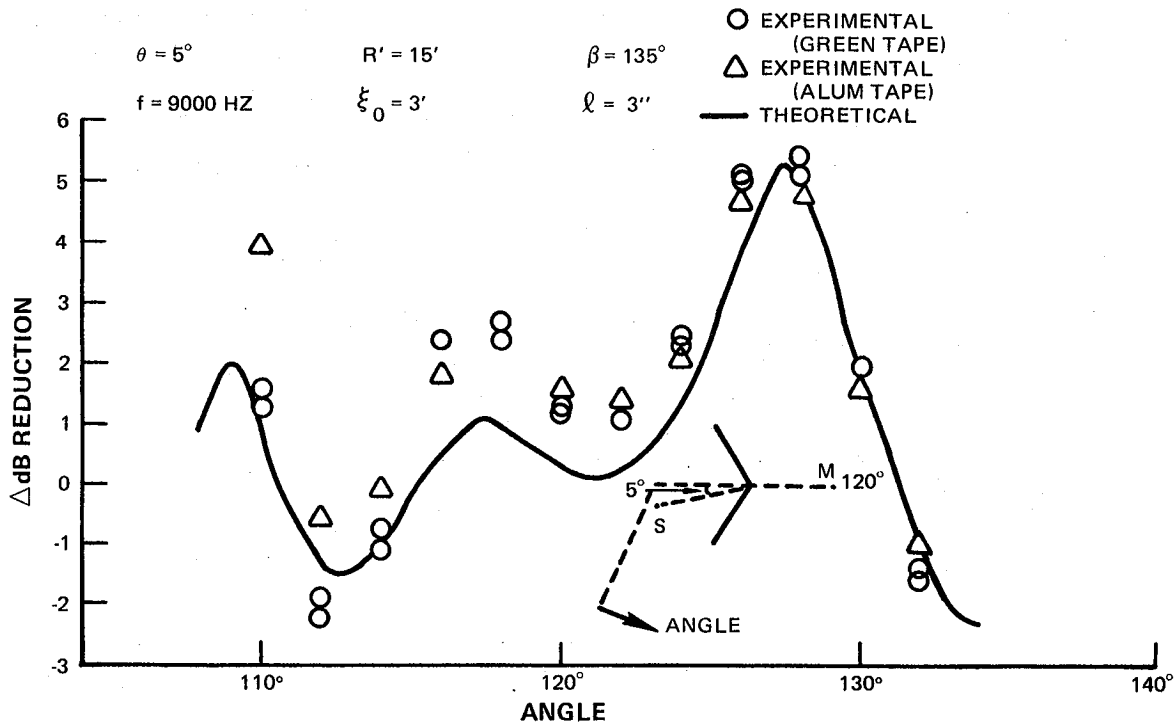

Figure 57 Diffraction at honeycomb corner comparison of measurement and prediction.

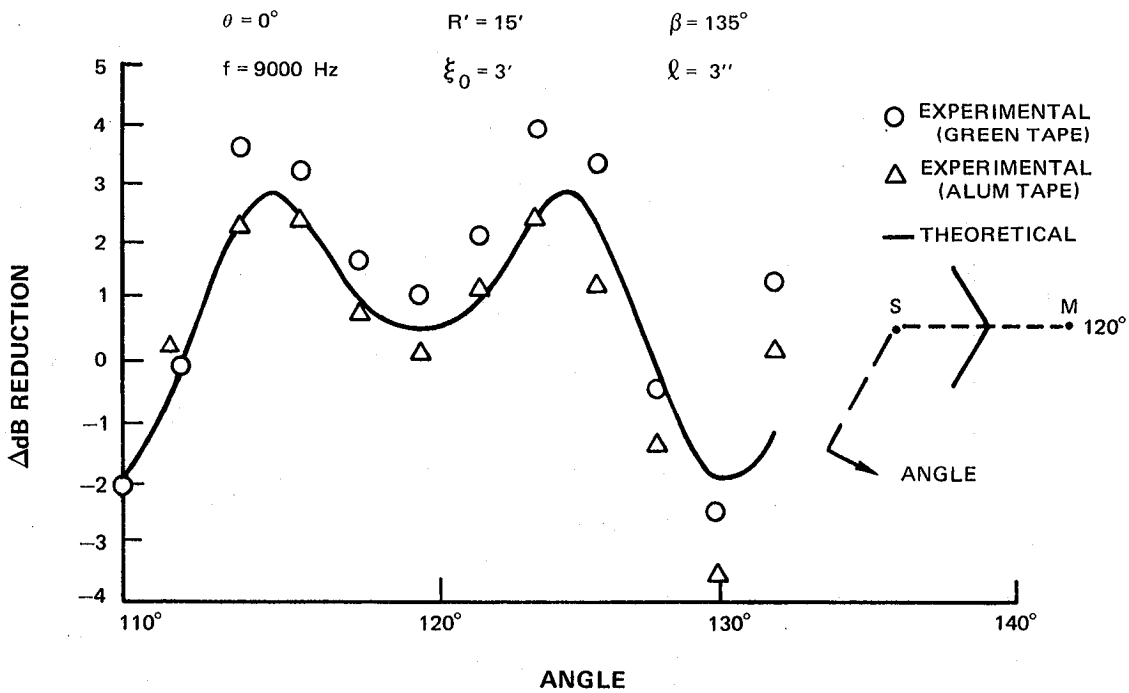

Figure 58 Diffraction at honeycomb corner comparison of measurement and prediction.

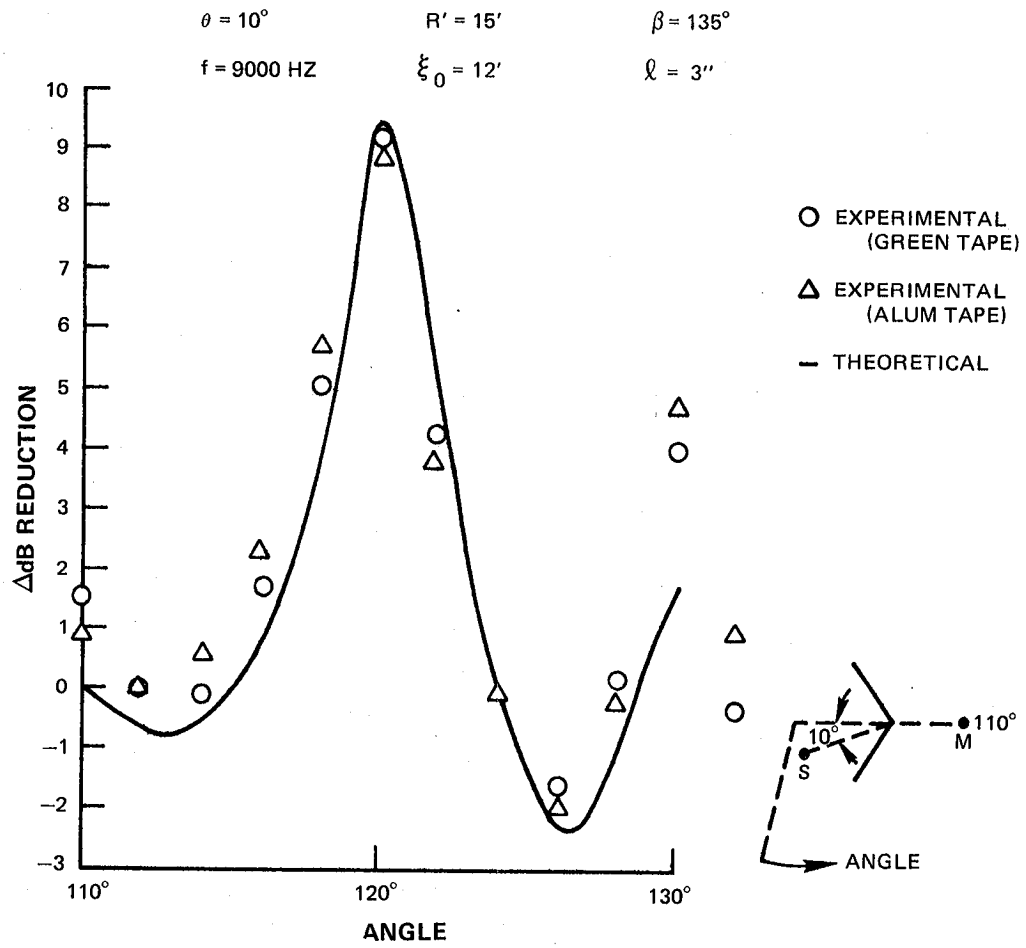

Figure 59 Diffraction at honeycomb corner comparison of measurement and prediction.

FREQUENCY / ANGLE OF INCIDENCE ↓	2KHz		5KHz		9KHz	
	MEAN DIFF.	S.D. FROM THEORY	MEAN DIFF.	S.D. FROM THEORY	MEAN DIFF.	S.D. FROM THEORY
0°	0.54	0.875	0.23	0.673	0.19	0.951
5°	0.29	0.969	0.45	0.793	0.79	1.138
10°	0.4	0.883	−0.22	0.546	0.71	1.248

FIGURE 11.3.12 VALUES OF (i) THE MEAN DIFFERENCE BETWEEN MEASUREMENT AND THEORETICAL PREDICTION

(ii) THE STANDARD DEVIATION OF THE MEASUREMENT FROM THE THEORETICAL PREDICTION IN dB.

Figure 60 The values of (i) the mean difference between measurement and prediction, (ii) the standard deviation of the measurement from the prediction in dB.

At 2kHz, all cases indicate that the levels are predicted well in an absolute sense and that the shape is well reproduced. The 5^0 incidence case is not predicted as well on either count as the other two. This is due to 3 data points around 130^0 taken for the aluminum tape configuration and these points are in conflict with the green tape measurements, which indicates that there were other differences between the configurations.

At 5kHz, both absolute levels and shape are very well predicted. In this case, it is apparent that the model is very impressive.

At 9kHz, a superficial glance indicates that the shapes are reasonably well predicted with absolute levels not very impressive, however, there are some alleviating considerations. Firstly, at this frequency small variations in angular position result in large changes in level. The position accuracy of the microphone has been estimated at $1/2^0$. Such a variation would cause large variations in the two parameters of Figure 60 particularly for the 10^0 incidence case. Thus at this high frequency case, errors can be attributed to measurement position error as well as model error, and discrimination between them is difficult.

Neglecting all alleviating considerations, however, upon averaging over all tests, 74% of the data was within 1 dB of the predictions. The 1dB figure is chosen since this is the error bound of measured SPL's. In addition, the mean difference obtained by averaging over all tests is about .38 dB and the corresponding standard deviation from the model prediction is about .9 dB.

11.4 Validity of the Model Assumptions

(i) $2\xi_o \gg R$

For the full scale inflow control structure, fitted on a JT9D, at a typical stand, ξ_o (the source to screen corner distance) is about 4.57m. R (the microphone array radius) is 4.57m. The assumption is thus marginally valid.

For the experimental situation ξ_o was .91m, and R was 4.57m. The assumption is not valid in this case.

(ii) $ka \gg 1$

For the full scale measurement situation, at a frequency of 2kHz (approximately B.P.F. at approach for JT9D), $kR \triangleq$ 1700. The assumption is definitely valid.

For the experimental situation, at 2kHz, $kR \triangleq$ 170. Again the assumption is valid.

(iii) $ka \gg 1$

For the full scale inflow control structure, a is about 7.62cm. and at 2kHz, $ka \triangleq 3$. This was also the lowest value for the experimental situation. This assumption is not valid at this frequency, but at frequencies above 5 kHz it is probably valid.

11.5 Concluding Statements

In spite of the violation of two model assumptions by the experimental arrangement, the theory produces predictions that are quite close to the measured directivity patterns. In addition, the full test situation will tend to meet one of these assumptions better. Consequently, this model can be used with some confidence in the full scale case.

The application of this model to a distributed source can be implemented by summing the contributions to the far field from each individual source region. A determination of the radiation field due to a line of sources is currently being made.

12.0 IMPLICATIONS OF ANALYTICAL STUDIES TO ICS DESIGN

Based on the analytical studies reported herein, the following general observations can be made to guide future ICS designs.

1. It is becoming increasingly apparent that the inflow distortion field is not solely due to direct contraction of atmospheric turbulence but also receives contributions from flow over stand structure, ground effects, etc. The consequence of this is that, to produce an optimum screen design for a given engine, the immediate structural environment must be accounted for. This obviously is going to vary from stand to stand. The most reasonable design course, given the variation in stands seems to be to specify a worst case and design for that. It should be noted that honeycomb and perforated plate suppress steady as well as unsteady velocity distortions.

2. In existing inflow control structures various combinations of honeycomb and perforated plate are used. The rationale for using honeycomb is quite easy to understand since transverse velocity components are amplified substantially by the subsequent contraction. The use of perforated plate which suppresses preferentially the streamwise components is somewhat harder to justify since the contraction strongly attenuates this component. However, the rapid initial rate of return to isotrophy downstream of the screen will cause the transverse velocity component to increase in value and thus be subsequently amplifiable by the contraction. The suppression of streamwise distortions appears then desirable in order to prevent this transfer of energy back into the transverse distortion component.

3. In order to render honeycomb transmission losses negligible, it is necessary to design for small through-flow velocities, on the order of 4.63 - 9.25m/s. Designs of this type require that the honeycomb structure be located outside the inlet, and in a region where inflow velocities are low.

4. Perforated plate transmission losses can be minimized by invoking Item 3 and requiring that design criterion of Equations 89 be met.

5. Directivity effects can be minimized by designing ICS's with a minimum of structure and discontinuities in the honeycomb and perforated plate surfaces.

13.0 CONCLUSIONS

1. A transfer function was developed that relates blade mounted transducer pressure measurements to inflow normal velocity. This function is defined in Figure 13 and will be applied to define inflight and static fan velocity distortion field.

2. Observations of PWA/Boeing Joint Noise Program Blade Mounted Transducer Data show that during static engine testing significant inflow distortions can result not only from atmospheric turbulence, but from the ground stand structure as well. Furthermore, the ICS's designed by PWA and Boeing for application to the JT9D engine were reasonably effective in removing these distortion types. These findings are discussed in Section 6 of this report.

3. Existing theoretical studies on the effects of contraction and screening on flow distortion have permitted formulation of analytical models that account for the effects of contraction and screening on steady and unsteady flow distortions.

   The models for the effects of contraction on unsteady and steady distortions are given in Equations 20, 21, 22, and 70, 71, 72, respectively. The models for the effects of screening on unsteady and steady distortions are given by Equations 45, 46, 48, 49, and 41, 43, respectively.

4. Models accounting for the effects of honeycomb and screen on acoustic transmission loss were developed and are given by Equations 100 and 88.

5. A model accounting for the effects of honeycomb and structure on acoustic directivity patterns was developed and shown to agree well with experimental data. This model is given by Equation 106.

6. Based on the studies carried out in Phases I and II of this contract, guidelines for future ICS designs were identified. These guidelines are discussed in Section 12 of this report.

APPENDIX A

The Power Spectral Density of the Unsteady Upwash Velocity Component of the Inflow Field

To determine the blade mounted transducer (BMT) response function it is necessary in part to relate the upwash velocity power spectral density to the measurements made by a hot film probe. This probe measures the streamwise and the circumferential component of the unsteady velocity field. The relationships between these various velocity components is shown in Figure 4.

By considering the rotation of the coordinate system it is seen that

$$u_\eta\ t = -u_1(t)\cos\gamma + u_2(t)\sin\gamma \tag{108}$$

Taking the Fourier transform of 108 yields

$$\mathcal{F}_\eta(\omega) = -\mathcal{F}_1(\omega)\cos\gamma + \mathcal{F}_2(\omega)\sin\gamma$$
$$\mathcal{F}(\omega)\,\mathcal{F}^*(\omega) \tag{109}$$

The power spectral density is proportional to $\mathcal{F}(\omega)\ \mathcal{F}^*(\omega)$ so that the relationships between the power spectral densities of the various velocity components is

$$F_\eta(\omega) = F_1(\omega)\cos^2\gamma + F_2(\omega)\sin^2\gamma -$$
$$\frac{1}{2}\left(F_{12}(\omega) + F_{21}(\omega)\right)\sin 2\gamma \tag{110}$$

Robson (60) has considered the general problem of the effect of angular rotation on spectral quantities and derives an expression corresponding to 110. There is, however, a misprint in that expression.

Estimates of the various terms in Equation 110 on an order of magnitude basis for the case of static operation of a JT9D at an approach power setting allows some simplification of the expression.

According to hot film measurement and analysis, in the tip region not in the boundary layer,

$$F_2(\omega) = 0\ \left\{10\,F_1(\omega)\right\}\quad \frac{|F_{12}(\omega)|^2}{F_1(\omega)F_2(\omega)} = 0\ \left\{.01\right\} \tag{111}$$

Now the magnitude of the real part of the cross spectral density function must be less than the total magnitude of the function or,

$$\left|Re\ \left[F_{12}(\omega)\right]\right| \leq \left|F_{12}(\omega)\right| \tag{112}$$

but from Equation 111

$$\left|F_{12}(\omega)\right| = 0\left\{.3\left|F_1(\omega)\right|\right\} = 0\left\{.3\,F_1(\omega)\right\} \tag{113}$$

Therefore,

$$\left|Re\ \left[F_{12}(\omega)\right]\right| \leq 0\left\{.3F_1(\omega)\right\} \tag{114}$$

Now in addition, in the vicinity of the tip the blade relative flow angle, $\gamma \cong 30^0$.

Thus the order of magnitude of the terms in Equation 110 become, for the static JT9D case under consideration;

$$F_\eta(\omega) = .75\,F_1(\omega) + .25\ \ 0\left\{10\,F_1(\omega)\right\} \pm 0\left\{.3F_1(\omega)\right\} \tag{115}$$

or

$$F_\eta(\omega) = 0\left\{3.25\,F_1(\omega)\right\} \pm 0\left\{.3F_1(\omega)\right\} \tag{116}$$

Therefore the term containing the real part of the cross spectral density is small compared to the sum of the other two terms and thus may be neglected. For this case, then Equation 110 may be simplified to

$$F_\eta(\omega) \cong F_1(\omega)\cos^2\gamma + F_2(\omega)\sin^2\gamma \tag{117}$$

APPENDIX B

Criteria for the Linearization of Equation 16 and the Applicability of that Equation to the JT9D Inflight and Static Operation

As stated previously the equation of motion for an incompressible, constant viscosity unsteady flow with zero mean vorticity is from Equation 16.

$$\frac{D\omega_i}{Dt} = \omega_j \frac{\partial U_i}{\partial x_j} + \omega_j \frac{\partial u_i}{\partial x_j} + \nu \nabla^2 \omega_i \qquad (118)$$

Taylor linearized this equation by neglecting the last two terms of Equation 118 thereby recovering Cauchy's equations. The justification for neglecting these terms is that of considering only a rapid distortion. Batchelor argues that if the contraction is sufficiently rapid, the straining of the fluid by the mean flow is the dominant effect. He formulates the criterion for the rapid distortion as

$$\frac{1}{\overline{u_{ii}}} \frac{d\overline{u_{ii}}}{dt} \ll \frac{U_{1AV}}{D} \qquad (119)$$

The change in the unsteady kinetic energy of the flow is that due to the turbulence inertial effect and the viscous decay U_1 average is the mean particle velocity through the contraction. Equation 119 states that the rate of change of the turbulent kinetic energy due to the two above mentioned effects is much less than the contraction rate. Batchelor proceeds to approximate $\frac{d\overline{u_{ii}}}{dt}$ with an expression empirically derived for turbulence in the initial period of delay and in the absence of mean flow gradients.

$$\frac{d\overline{u_{ii}}}{dt} = \frac{E}{\ell} \left\{\overline{u_{ii}}\right\}^{3/2} \qquad (120)$$

Where ℓ is a turbulent scale and $E \simeq 1$.

Substituting this expression in Equation 119 and assigning characteristic values to the kinetic energy and turbulence length scale produce the Batchelor's criterion for neglecting the last two terms in Equation 118.

$$\frac{(\overline{u_{ii}})^{1/2}}{U_{1AV}} \ll \frac{\ell}{D} \qquad (121)$$

In terms of the initial mean flow velocity and contraction

$$\frac{(\overline{u_{ii}})^{1/2}}{U_{1A}} \ll \frac{\ell}{D}\left(\frac{\ell_1+1}{2}\right) \tag{122}$$

It is noted that this inequality is always satisfied for sufficiently large contraction rate, $\frac{\ell}{d}$. Furthermore, on consideration of this inequality at any point x , from the beginning of the contraction

$$\frac{(\overline{u_{ii}})^{1/2}}{U_{1A}} \ll \frac{\ell}{x_1}\;\frac{\ell_1(x_1)+1}{2} \tag{123}$$

It is immediately apparent that this inequality is satisfied for sufficiently small x_1 . The criterion for linearization in 122 depends on the empirical relationship 120 whose applicability to turbulence in the presence of mean flow gradients must be questioned. It is suggested as an alternative that the approach used by Ribner and Tucker (37) may be more satisfactory. Those authors generate the criteria directly from Equation 118. Thus, for neglect of the turbulence inertial and viscous decay terms in Equation 118 it is necessary that

$$\left|\omega_j \frac{\partial u_i}{\partial x_j}\right| \ll \left|\omega_j \frac{\partial U_i}{\partial x_j}\right| \tag{124}$$

and

$$\left|\nu\nabla^2\omega_i\right| \ll \left|\omega_j \frac{\partial U_i}{\partial x_j}\right| \tag{125}$$

Considering first the turbulence inertial criteria 124, Ribner and Tucker suggest that the dominant mean flow gradients in a typical contraction are $\frac{\partial U_1}{\partial x_1}$, $\frac{\partial U_2}{\partial x_2}$ and $\frac{\partial U_3}{\partial x_3}$ and these are of comparable magnitude. If it is assumed that the other gradients are zero, inequalities 124 reduce to

$$\left|\omega_j \frac{\partial u_1}{\partial x_j}\right| \ll \left|\omega_1 \frac{\partial U_1}{\partial x_1}\right| \left|\omega_j \frac{\partial u_2}{\partial x_j}\right| \ll \left|\omega_2 \frac{\partial U_1}{\partial x_1}\right| \tag{126}$$

$$\left|\omega_j \frac{\partial u_3}{\partial x_j}\right| \ll \left|\omega_3 \frac{\partial U_1}{\partial x_1}\right|$$

To determine more useful forms of the inequalities 126 the gradients will be estimated using average values. This 126 becomes

$$\frac{(\overline{\omega_j^2})^{1/2}\,(\overline{u_1^2})^{1/2}}{\ell_j} \ll (\overline{\omega_1^2})^{1/2}\frac{\Delta U_1}{\Delta x_1}$$

$$\frac{(\overline{\omega_j^2})^{1/2}\,(\overline{u_2^2})^{1/2}}{\ell_j} \ll (\overline{\omega_2^2})^{1/2}\frac{\Delta U_1}{\Delta x_1} \qquad (127)$$

$$\frac{(\overline{\omega_j^2})^{1/2}\,(\overline{u_3^2})^{1/2}}{\ell_j} \ll (\overline{\omega_3^2})^{1/2}\frac{\Delta U_1}{\Delta x_1}$$

where $\ell_j = \ell_1, \ell_2, \ell_3$ are Cartesian length scales. In an axisymmetric flow the last two inequalities become the same.

Now the results from the simple contraction model are reasonably close to the mean square velocity ratios determined by the Batchelor and Proudman, Ribner and Tucker solutions to the problem. Consequently these simple model results may be considered approximations to the linearized theory and as such when substituted in 127 will provide criteria for the neglect of the turbulence inertial terms. Before this substitution is made, however, it is noted that the inequalities in 127 must be satisfied everywhere in the contraction in order for the linearization of Taylor to be valid. Therefore, the inequalities will be established at the beginning and end of the contraction and the most constraining criterion will be the minimum requirement for neglect of the turbulence inertial terms. If then the turbulence field is assumed initially isotropic, at the beginning of the contraction

$$\overline{\omega_{1A}^2} = \overline{\omega_{2A}^2} = \overline{\omega_{3A}^2}$$

$$\overline{u_{1A}^2} = \overline{u_{2A}^2} = \overline{u_{3A}^2}$$

and if isotropic turbulence is characterized by spherical eddies then

$$\ell_{1A} = \ell_{2A} = \ell_{3A}$$

and thus inequalities in 127 reduce the

$$\frac{3(\overline{u_{1A}^2})^{1/2}}{\ell_{1A}} \ll \frac{\Delta U_1}{\Delta x_1} = \frac{U_{1A}}{D}(\lambda_1 - 1) \qquad (128)$$

or

$$\frac{(\overline{u_{1A}^2})^{1/2}}{U_{1A}} \ll \frac{\ell_{1A}(\lambda_1 - 1)}{3D}$$

where ℓ_1 = contraction ratio

and D = contraction length

The A subscript denotes the pre-contraction station. At the end of the contraction, using the simple model results in

$$(\overline{\omega_{1B}^2}) = \ell_1 \quad (\overline{\omega_{1A}^2})^{1/2}$$

$$(\overline{\omega_{2B}^2}) = \ell_1^{-1/2} (\overline{\omega_{2A}^2})^{1/2} = \ell_1^{-1/2} (\overline{\omega_{1A}^2})^{1/2}$$

$$(\overline{\omega_{3B}^2}) = \ell_1^{-1/2} (\overline{\omega_{3A}^2})^{1/2} = \ell_1^{-1/2} (\overline{\omega_{1A}^2})^{1/2}$$

$$\overline{u_{1B}^2} = \ell_1^{-2} \overline{u_{1A}^2}$$

$$\overline{u_{2B}^2} = \ell_1 \overline{u_{2A}^2} = \ell_1 \overline{u_{1A}^2}$$

$$\overline{u_{3B}^2} = \ell_1 \overline{u_{3A}^2} = \ell_1 \overline{u_{1A}^2}$$

$$\ell_{1B} = \ell_1 \ell_{1A}$$

$$\ell_{2B} = \ell_1^{-1/2} \ell_{2A} = \ell_1^{-1/2} \ell_{1A}$$

$$\ell_{3B} = \ell_1^{-1/2} \ell_{3A} = \ell_1^{-1/2} \ell_{1A}$$

Substitution in 127 yields

$$\frac{(\overline{u_{1A}^2})^{1/2}}{u_{1A}} \ll \frac{\ell_{1A}}{D} \frac{\ell_1^2(\ell_1-1)}{3} \qquad \text{a} \qquad (129)$$

$$\frac{(\overline{u_{1A}^2})^{1/2}}{u_{1A}} \ll \frac{\ell_{1A}}{D} \frac{(\ell_1-1)}{3\ell_1} \qquad \text{b}$$

Comparing the criteria(128, 129a and 129b) it is noted that if 129b is satisfied, all are satisfied and so this inequality must be satisfied if the turbulence inertial terms are to be neglected through the contraction.

Kibner and Tucker developed the criterion for neglect of the viscous decay term in Equation 118 by simply requiring that

$$\nu \nabla^2 \omega_i \ll \omega_j \frac{\partial U_i}{\partial x_j} \tag{130}$$

and then considering a single shear wave they obtained the result that

$$\nu k^2 \ll \left| \frac{\partial U_1}{\partial x_1} \right| \tag{131}$$

where k is the absolute value of the wave number vector.

If the mean flow gradient in Equation 131 is approximated, that inequality becomes

$$\nu k^2 \ll \frac{U_1 (l_1 - 1)}{D} \tag{132}$$

It is the opinion of Kibner and Tucker that the major part of the spectrum will satisfy this condition. It should be noted that the viscous neglect criterion 132 is conditional on the turbulence inertial term in Equation 118 being negligible.

Application of the turbulence inertial effect neglect criterion 129b to a JT9D operating statically and in flight provides information on the applicability of the linearized theories to these situation. Both sides of the inequality are shown in the table below for both operating environments. The values of initial turbulence intensity are determined from the atmospheric model presented in the Phase I report of this contract.

	Contraction Ratio ℓ_1	Contraction Length D	Initial Scale ℓ_{1A}	Initial Intensity $\frac{(u_{1B}^2)^{1/2}}{(u_{1A})}$	$\frac{\ell_{1A}(\ell_1-1)}{D\ 3\ell_1}$
Inflight	1.5	3m	.43m	.0016	.016
Statically	50	15m	3.54m	.2	.077

The inequalities are satisfied for the flight case but not for static operation. Therefore the linear solution approximated by the eddy model is valid for the in-flight contraction phenomenon. In static operation however, turbulence inertial effects are not negligible and consequently the tendency to isotropy will alleviate the distortion of the turbulence due to the flow contraction. In this latter case however, it is possible that a reasonable estimate of the turbulent kinetic energy change through the contraction is provided by the eddy model if a decay correction is incorporated (43).

The test program of Task F will supply information on the effect of non-linear contractions on turbulence, since the linearizing requirement is not satisfied for the small test facility.

APPENDIX C

The Effect of a Contraction on Turbulence Integral Length Scales Using the Linear Theory

Using the results of Batchelor and Proudman (38) and their notation

$$\Phi_{11}(0, K_2, K_3) = \frac{1}{e_1^2}\,\Phi_{11}'(0, k_2, k_3) \tag{133}$$

where

Φ_{ii} is the three dimensional spectrum tensor for the ith velocity component.

The prime indicates the pre contraction location

k_i, K_i are the pre and post contraction wavenumber vectors.

e_i are the diagonal components of the strain tensor.

with corresponding expressions for $\Phi_{22}(K_1=0)$, and $\Phi_{33}(K_1=0)$. Integrating over K_2 and K_3 produces the relationships between the corresponding upstream and downstream one dimensional spectra at $K_1 = 0$.

$$P_1(K_1=0) = \frac{1}{e_1}\,P_1'(k_1=0) \tag{134}$$

and noting that the scale of the ith velocity component in the j direction.

$$L_{ij} \propto \frac{P_i\ k_j=0}{\overline{u_i^2}} \tag{135}$$

then

$$\frac{L_{11}}{L_{11}'} = \frac{1}{e_1}\,\frac{\overline{u_1'^2}}{\overline{u_1^2}} \tag{136}$$

and for the other components

$$\frac{L_{22}}{L'_{22}} = \frac{1}{e_2}\,\frac{\overline{u_2'^2}}{\overline{u_2^2}}\;;\quad \frac{L_{33}}{L'_{33}} = \frac{1}{e_3}\,\frac{\overline{u_3'^2}}{\overline{u_3^2}} \tag{137}$$

for an axisymmetric contraction such that then $e_1 = \ell_1$, and $e_2 = e_3 = \ell_1^{-1/2}$ then

$$\frac{L_{11}}{L'_{11}} = \frac{1}{\ell_1 \mu_1}\;;\quad \frac{L_{22}}{L'_{22}} = \frac{\sqrt{\ell_1}}{\mu_2}\;;\quad \frac{L_{33}}{L'_{33}} = \frac{\sqrt{\ell_1}}{\mu_3} \tag{138}$$

where

$$\mu_1 = \frac{\overline{u_1^2}}{\overline{u_1'^2}}\,,\ \mu_2 = \frac{\overline{u_2^2}}{\overline{u_2'^2}}\;;\ \mu_3 = \frac{\overline{u_2^2}}{\overline{u_3'^2}}\,.$$

For an axisymmetric contraction it is also true that

$$\Phi_{22}(0, K_2, K_3) = \ell_1 \Phi'_{22}(0, k_2, k_3) \tag{139}$$

and consequently

$$\frac{L_{21}}{L'_{21}} = \frac{\ell_1^2}{\mu_2}\;;\quad \frac{L_{31}}{L'_{31}} = \frac{\ell_1^2}{\mu_3}\,. \tag{140}$$

These relationships are all independent of the initial turbulence field, however, for any initially isotropic field $\nu_1 = \nu_2$ and Batchelors' expressions for $\mu = \mu_1$ and $\nu = \mu_2 = \mu_3$ may be used in Equations 138 and 140. For the latter case the ratios are shown in Figure 19.

APPENDIX D

The Effect of Screens on Turbulence Integral Length Scales Using the Linear Theory

As in the contraction effect, certain length scales of an isotropic turbulence field are changed by the screen in a manner that does not depend on the particular form of the field.

From Batchelor's formulation of the solution(43)a little manipulation shows that

$$\Phi_{11}(0, K_2, K_3) = JJ^*(K_1=0)\,\Phi'_{11}(0, K_2, K_3) \tag{141}$$

$$\Phi_{22}(0, K_2, K_3) = \alpha^2\,\Phi'_{22}(0, K_2, K_3) \tag{142}$$

$$\Phi_{33}(0, K_2, K_3) = \alpha^2\,\Phi'_{33}(0, K_2, K_3) \tag{143}$$

$$\Phi_{22}(K_1, 0, K_3) = \alpha^2\,\Phi'_{22}(K_1, 0, K_3) \tag{144}$$

$$\Phi_{33}(K_1, K_2, 0) = \alpha^2\,\Phi'_{33}(K_1, K_2, 0) \tag{145}$$

where $JJ^*(K_1=0) = \dfrac{1+\alpha-\alpha K}{1+\alpha+K}$

Φ_{ii} is the velocity spectrum tensor and

the prime denotes the downstream location

K_i is the wave number vector

α is the flow angle ratio

The coefficients in each case being independent of K_i, and thus integration over the non zero wavenumber components produces the relationships between the one dimensional spectra value at zero.

$$P_1(K_1=0) = JJ^*(K_1=0)\,P_1'(K_1=0) \tag{146}$$

$$P_2(K_1=0) = \alpha^2 \; P_2'(K_1=0) \tag{147}$$

$$P_3(K_1=0) = \alpha^2 \; P_3'(K_1=0) \tag{148}$$

$$P_2(K_2=0) = P_2'(K_2=0) \tag{149}$$

$$P_3(K_3=0) = P_3'(K_3=0) \tag{150}$$

and again noting that the scale of the ith velocity component in the j direction

$$L_{ij} \propto \frac{P_i(K_i=0)}{\mu_i^2} \tag{151}$$

then

$$\frac{L_{11}}{L_{11}'} = \frac{JJ^*(K_1=0)}{\mu_1} \tag{152}$$

$$\frac{L_{21}}{L_{21}'} = \frac{\alpha^2}{\mu_2} \tag{153}$$

$$\frac{L_{31}}{L_{31}'} = \frac{\alpha^2}{\mu_3} \tag{154}$$

$$\frac{L_{22}}{L_{22}'} = \frac{\alpha^2}{\mu_2} \tag{155}$$

$$\frac{L_{33}}{L_{33}'} = \frac{\alpha^2}{\mu_3} \tag{156}$$

For an initially isotropic field $\mu_2=\mu_3$ and Taylor and Batchelor's expressions Equations 32 and 33 for $\mu=\mu_1$ and $\nu=\mu_2=\mu_3$ may be used in Equations 152 through 156 above. It should be noted that the other length scale ratios are dependent in form on the initial turbulence spectrum and general statements cannot be made about them.

APPENDIX E

A Comparison Between Measured Honeycomb Loss Coefficients and Values Determined Using Blasius' Formula for Turbulent Pipe Flow

The Blasius formula for turbulent flow in smooth pipes is valid for diameter Reynolds Number less than 10^5 and greater than 3.10^3. It may be written in the form of a loss coefficient.

$$K = \frac{.3164}{Re^{.25}} \cdot \frac{\ell}{d} \qquad (157)$$

where Re is the diameter Reynolds Number
and $\frac{\ell}{d}$ is the pipe length to diameter ratio

The only adaptation necessary to apply this expression to a honeycomb is to determine the velocity of the flow in the cell U_c . This may be written as $(1-s)^{-1} U_{1\infty}$ for incompressible flow, where s is the solidity of the honeycomb.

The measurements conducted by Paterson were made for flow speeds, using .95cm diameter honeycomb with a length of 7.62cm. The characteristics of this honeycomb were $\ell/d = 8$ and $s = 0.05$.

The results of the comparison are shown in the table below.

$U_{1\infty}$	U_{1c}	Re	$Re^{.25}$	K calculated	K measured
16	16.8	3350	7.61	.333	.365
30	31.6	6302	8.91	.284	.295
50	52.6	10490	10.12	.25	.26
68	71.6	14279	10.93	.232	.255

Table 1 Comparison of Measured and Calculated Honeycomb Loss Factors

The turbulent pipe flow loss coefficient provides reasonably accurate estimates of the zero incidence angel pressure drop coefficient for this honeycomb. The pressure drop coefficient for this honeycomb appears to be dominated by skin friction, however, for higher solidity honeycombs other components of the form drag, e.g., base drag, may be important.

APPENDIX F

The Virtual Characteristics of the Dissipative Wake in a Flow Contraction

The contraction of the wake is approximated by a series of steps in which alternately the wake is dissipated in a uniform flow and then contracted instantaneously. In each of the dissipating regions the wake can be considered to evolve as if it were generated, for each region, by a rod of diameter a, drag coefficient C_D located at a distance X. These values will be different for each dissipative region and are thus termed here as "virtual characteristics". In each dissipative region the product $C_D a$ will be invariant and will change instantaneously across each contraction, Figure 61.

The assumption of wake characteristics obeying the Equations 64 allows the observation that

$$\Delta U_1 b = U_{1\infty} C_D a \tag{158}$$

at any point in the flow contraction. Thus across the first instantaneous contraction

$$\frac{C_D a(r_B)}{C_D a(r_A)} = \frac{\Delta U_1(r_B)}{\Delta U_1(r_A)} \cdot \frac{b(r_B)}{b(r_A)} \cdot \frac{U_{1\infty}(r_A)}{U_{1\infty}(r_B)} \tag{159}$$

by definition $\frac{U_{1\infty}(r_B)}{U_{1\infty}(r_A)} = c_1$, (the contraction ratio of Step 1) and from the approximate contraction theory

$$\frac{\Delta U_1(r_B)}{\Delta U_1(r_A)} = \frac{1}{c_1} \quad \text{and} \quad \frac{b(r_B)}{b(r_A)} = \frac{1}{c_1^{1/2}} \tag{160}$$

but $$\frac{C_D a(r_B)}{C_D a(r_A)} = c_1^{-5/2}$$

$$C_D a(r_A) = C_D a(r_o)$$

$$\therefore \quad C_D a(r_B) = c_1^{-5/2} C_D a(r_o)$$

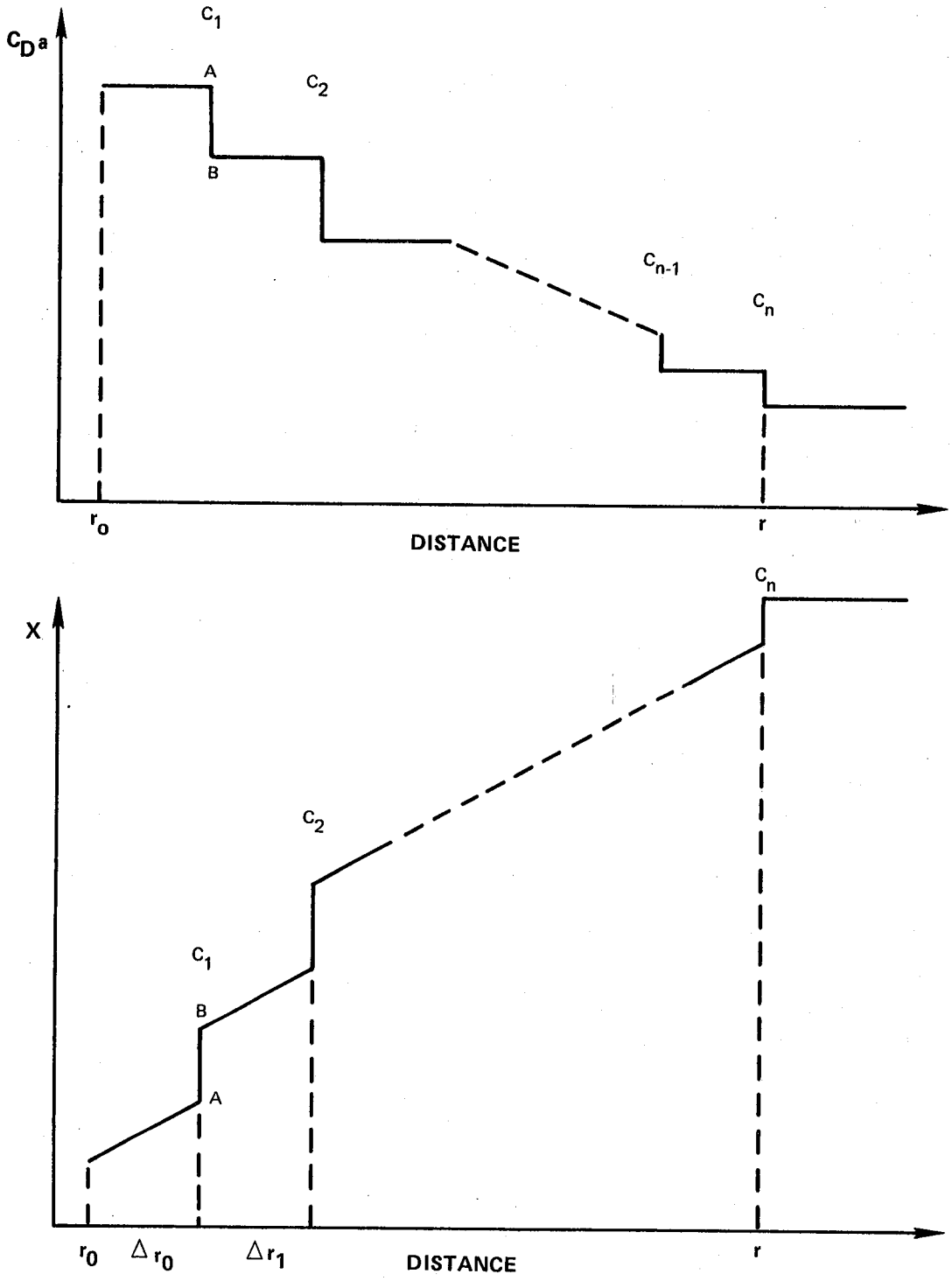

Figure 61 The virtual wake characteristics in a contraction.

and after n contractions in a length $(r - r_o)$

$$C_D a(r) = (C_1 \cdot C_2 \cdots\cdots C_n)^{-5/2} \; C_D a(r_o) \tag{161}$$

Now letting $n \to \infty$

$$\begin{aligned} C_D a(r) &= \mathcal{L}t_{n\to\infty} (C_1 \cdot C_2 ---- C_n)^{-5/2} \; C_D a(r_o) \\ &= \ell_1(r)^{-5/2} \; C_D a(r_o) \end{aligned} \tag{162}$$

where $\ell_1(r)$ is the overall flow contraction ratio to the point r.

The virtual source distance varies through the dissipative region and changes instantaneously at the contraction Figure 61.

Again from 64

$$\frac{b}{\Delta u_1} = \frac{x}{u_{1\infty}} \tag{163}$$

which yields the relationship of the virtual source distance across the first contraction

$$\frac{X(r_B)}{X(r_A)} = C_1^{3/2} \tag{164}$$

but $$X(r_A) = X(r_o) + \Delta r_o$$

thus $$X(r_B) = C_1^{3/2} (X(r_o) + \Delta r_o) \tag{165}$$

and after n contractions

$$\begin{aligned} X(r) &= C_n^{3/2} \left[C_{n-1}^{3/2} \left[C_{n-2}^{3/2} \left[- - - \left[C_1^{3/2} \left[X(r_o) + \Delta r_o \right] - - - + \Delta r_{n-2} \right] \right. \right. \right. \\ &\quad \left. \left. \left. + \Delta r_{n-1} \right] \right] \\ &= \ell_1^{3/2}(r) (X(r_o) + \Delta r_o) + \frac{\ell_1^{3/2}(r)}{C_1^{3/2}} \Delta r_1 + \frac{\ell_1^{3/2}(r)}{C_1^{3/2} C_2^{3/2}} \Delta r_2 \\ &\quad ---- + \frac{\ell_1(r)^{3/2}}{C_1^{3/2} C_2^{3/2} ---\cdot C_{n-1}^{3/2}} \Delta r_{n-1} \end{aligned}$$

Writing in terms of the mean velocities

$$X(r) = \ell_1^{3/2}(r)\,(X(r_0)+\Delta r_0) + \left\{\frac{U_\infty(r)}{U_{\infty_1}}\right\}^{3/2}\Delta r_1 + \tag{166}$$

$$+\left\{\frac{U_\infty(r)}{U_{\infty_2}}\right\}^{3/2}\Delta r_2 + \text{----} + \left\{\frac{U_\infty(r)}{U_{\infty(n-1)}}\right\}^{3/2}\Delta r_{n-1}$$

or $$X(r) = \ell_1^{3/2}(r)\,X(r_0) + \sum_{i=1}^{n}\left\{\frac{U_\infty(r)}{U_{\infty_{i-1}}}\right\}^{3/2}\Delta r_{i-1}$$

Let $n\to\infty$

$$X(r) = \ell^{3/2}(r)\,X(r_0) + \int_{r_0}^{r}\left\{\frac{U_\infty(r)}{U_\infty(r')}\right\}^{3/2} dr' \tag{167}$$

Equations 162 and 167 contain the expressions for the virtual wake characteristics that are used in Section 9.

APPENDIX G

Simplification of the Velocity Potential Due to a Source on a Half Plane

Bowman, Senior and Uslenghi(57) present the solution for the non dimensional velocity potential for the hardwall case as

$$\psi(R,\phi) = 2i\int_{-m}^{\infty} \frac{H_1^{(1)}(\mu^2+kR)}{(\mu^2+2kR)^{1/2}}\, d\mu \qquad (168)$$

where

$$m = \pm\sqrt{k(R_1-R)}$$

See Figure 46 for the geometry

For the farfield regime $kR \gg 1$, and so

$$\mu^2 + kR \gg 1$$

Now from Morse and Ingard (61), for large arguments the Hankel function may be approximated as

$$H_1^{(1)}(z) = \sqrt{\frac{2}{\pi z}}\ \exp\left[i\left\{z - \frac{3\pi}{4}\right\}\right] \qquad (169)$$

$$\therefore\ \psi = 2i\sqrt{\frac{2}{\pi}}\ \exp\left[i(kR - \tfrac{3\pi}{4})\right] \int_{-m}^{\infty} \frac{e^{i\mu^2}\, d\mu}{\{(\mu^2+kR)(\mu^2+2kR)\}^{1/2}} \qquad (170)$$

Now putting

$$W = 2i\sqrt{\frac{2}{\pi}}\ \exp\left[i(kR - \tfrac{3\pi}{4})\right]$$

and splitting the integration in two, leads to

$$\psi = W\left\{\underbrace{\int_{-m}^{0}}_{I_1} + \underbrace{\int_{0}^{\infty}}_{I_2}\right\} \qquad (171)$$

Examining I_1 ; note that $m^2_{MAX} = k(R_1-R)_{MAX} = 2k\xi_0$

Therefore if it is assumed that $R \gg 2\xi_0$ then in the range of integration, the denominator of the integrand may be considered independent of μ .

Thus $$I_1 = \int_{-m}^{\circ} \frac{\cos \mu^2 d\mu}{kR\sqrt{2}} + i \int_{-m}^{\circ} \frac{\sin \mu^2 d\mu}{kR\sqrt{2}} \qquad (172)$$

Evaluating this integral in terms of Fresnel integrals, see Equation 103, yields

for $m+ve$ $$I_1 = \frac{\sqrt{\pi}}{2kR}\{C + iS\} \qquad (173)$$

and for $m-ve$ $$I_1 = \frac{\sqrt{\pi}}{2kR}\{C + iS\} \qquad (174)$$

Then for $m+ve$ $$\psi = W\left\{\frac{\sqrt{\pi}}{2kR}(C+iS) + I_2\right\} \qquad (175)$$

and for $m-ve$

$$\psi = W\left\{-\frac{\sqrt{\pi}}{2kR}(C+iS) + I_2\right\} \qquad (176)$$

where $|m|$ is used in the Fresnel integrals. Now note that the sum of these fields produces the same field as that generated by a simple source of twice the strength

i.e. $$\psi_{m+ve} + \psi_{m-ve} = \frac{2e^{ikR}}{kR} \qquad (177)$$

or

$$4i\sqrt{\frac{2}{\pi}} \exp\left[i\left(kR - \frac{3\pi}{4}\right)\right] I_2 = \frac{2e}{kR}^{ikR}$$

which gives

$$I_2 = \frac{\sqrt{\pi}}{4kR}(1+i) \qquad (178)$$

Substituting 178 and 175 or 176 produces the expression for

$$\psi = \frac{\sqrt{2}}{2kR} \exp\left[i\left(kR - \frac{\pi}{4}\right)\right]\left\{\left(\frac{1}{2}+C\right) + i\left(\frac{1}{2}+S\right)\right\} \qquad (179)$$

This form of the velocity potential for a simple source on a half plane is the building block for the honeycomb corner diffraction model of Section 11.

References:

1. T. G. Sofrin and J. C. McCann, "Pratt and Whitney Aircraft Experience to Compressor Noise Reduction", Paper presented at 72nd Meeting of Acoustical Society of America, 1966.

2. Cumpsty, N. A. and Lowrie, B. W., "The Cause of Tone Generation by Aero-Engine Fans at High Subsonic Tip Speeds and the Effect of Forward Speed", Paper 73-Wa/GT-4 ASME, 1973.

3. Hodder, B. K., "The Effects of Forward Speed on Fan Inlet Turbulence and Its Relation to Tone Noise Generation", NASA TMX 62, 381, 1974.

4. Roundhill, J. P. and Schaut, L. A., "Model and Full Scale Test Results Relating to Fan Noise Inflight Effects", AIAA Paper 75-465.

5. Feiler, C. E. and Merriman, J. E., "Effects of Forward Velocity and Acoustic Treatment on Inlet Fan Noise", NASA TMX-71591, 1974.

6. Plucinsky, J. C., "Quiet Aspects of the Pratt and Whitney Aircraft JT15D Turbofan", SAE Paper 730289, 1973.

7. Hanson, D. B., "Spectrum of Rotor Noise Caused by Atmospheric Turbulence", NASA Volume 56 No. 1, 1974.

8. Hanson, D. B., "Study of Noise Sources in a Subsonic Fan Using Measured Blade Pressures and Acoustic Theory", NASA CR-2574, 1975.

9. Hanson, D. B., "Study of Noise and Inflow Distortion Sources in the NASA QF-1B Fan Using Measured Blade and Vane Pressures", NASA CR-2899, 1977.

10. Bekofske, K. L., Sheer, R. E. Wang, J. F. C., "Fan Inlet Disturbances and Their Effect on Static Acoustic Data", ASME Paper No. 77-GT-63, 1977.

11. Povinelli, V. P., Dittmar, J. H., and Woodward, R. P., "Effects of Installation Caused Flow Distortion on Noise from a Fan Designed for Turbofan Engines", NASA TN D-7076, 1972.

12. Hodder, B. K., "An Investigation of Possible Causes for the Reduction of Fan Noise Inflight", AIAA Paper 78-585.

13. Shaw, L. M., Woodward, R. P., Glaser, F. W., and Dastoli, B. J., "Inlet and Fan Noise Measured in an Anechoic Wind Tunnel and Statically with an Inflow Control Device", NASA TM-73723.

14. Lowrie, B. W., "Simulation of Flight Effects on Aero Engine Noise", AIAA Paper 75-463.

References: (Cont'd)

15. Heidmann, M. F. and Dietrich, D. A., "Simulation of Flight Type Engine Fan Noise in the NASA-Lewis 9x15 Anechoic Wind Tunnel", NASA TMX-73540.

16. Prantl, L., "Attaining a Steady Airstream in Wind Tunnels", NASA TM 726.

17. Collar, A. R., "The Effect of a Gauze on the Velocity Distribution in a Uniform Duct", ARC R&M, 1867 1937.

18. Batchelor, G. K., "On the Concept and Properties of the Idealized Hydrodynamic Resistance", Australian Council for Aeronautics, ACA 13, 1945.

19. Taylor, G. I., and Batchelor, G. K., "The Effect of Wire Gauze on Small Disturbances in a Uniform Stream", Quart Journ. Mech. and Applied Math, Vol. II Part 1, 1949.

20. Lumley, J. L., "Passage of a Turbulent Stream Through Honeycomb of Large Length to Diameter Ratio", ASME Paper No. 63-AHGT-2, 1964.

21. Loehrke, R. I., and Nagib, H. M., "Control of Free Stream Turbulence by Means of Honeycombs: A Balance Between Suppression and Generation", ASME Paper No. 76-FE-2.

22. Leggat, L. J. and Siddon, T. E., "Experimental Study of the Aeroacoustic Mechanism of Rotor-Vortex Interactions", JASA 64 (4), 1978.

23. Jones, W. L., McArdle, J. G., and Miak, "Evaluation of Two Inflow Control Devices for Flight Simulation of Fan Noise Using a JT15D Engine", AIAA Paper 79-0654.

24. Ffowcs-Williams, J. E., and Hawkings, D. L., "Theory Relating to the Noise of Rotating Machinery", JSV 10 (1), 1969.

25. Mani, R., "Noise Due to Interaction of Inlet Turbulence with Isolated Stators and Rotors", JSV 17 (2), 1971.

26. Pickett, G. F., "Effects of Non-Uniform Inflow on Fan Noise", Presented at the Spring Meeting, Acoustical Society of America, New York City, April 23-26, 1974.

27. Lowrie, B. W., and Newby, D. R., "The Design and Calibration of a Distortion-Reducing Screen for Fan Noise Testing", AIAA Paper 77-1323.

References: (Cont'd)

28. Woodward, R. P., Wazyniak, J. A. Shaw, L. M., MacKinnon, M. J., "Effectiveness of an Inlet Flow Turbulence Control Device to Simulate Flight Fan Noise in an Anechoic Chamber", NASA-TM-73855, 1977.

29. Cocking, B. J., and Ginder, R. B., "The Effect of An Inflow Conditioner on Fan Distortion Tones", AIAA Paper 77-1324.

30. Kantola, R. A. and Warren, R. E., "Reduction of Rotor-Turbulence Interaction Noise in Static Fan Noise Testing", AIAA Paper 79-0656.

31. Ho, P. Y., Smith, E. B., and Kantola, R. A., "An Inflow Turbulence Reduction Structure for Scale Model Fan Testing", AIAA Paper 79-0655.

32. Ginder, R. B., Kenison, R. C. Smith, A. D., "Considerations for the Design of Inlet Flow Conditioners for Static Fan Noise Testing", AIAA Paper 79-0657.

33. Hanson, D. B., "Application of Rotor Mounted Pressure Transducers to Analysis of Inlet Turbulence", Paper Number 177-9, AGARD 46th Propulsion and Energetics Panel Meeting on Unsteady Phenomena in Turbomachinery, September 1975.

34. Ganz, U., "Forward Speed Effects on Fan Noise", NAS1-15085, Phase I Final Report NASA CR

35. Taylor, G. J., "Turbulence in a Contracting Stream", ZAMM, XV, 1935.

36. Lamb, H., "Hydrodynamics", Dover, 1945.

37. Ribner, H. S., Tucker, M., "Spectrum of Turbulence in a Contracting Stream", NACA 1113, 1953.

38. Batchelor, G. K., Proudman, I., "The Effect of Rapid Distortion of a Fluid in Turbulent Motion", Quart. Journ. Mech. and App. Math. Vol VII, Pt. 1, 1954.

39. Pearson, J. R. A., "The Effect of Uniform Distortion on Weak Homogeneous Turbulence", J.F.M., Vol. 5, Pt. 3, 1959.

40. Uberoi, M. S., "Effect of Wind-Tunnel Contraction on Free-Stream Turbulence", J. Aero. Sci. 23, 8. 1956.

41. Hussain, A. K. M. F., Ramjee, V., "Effects of the Axisymmetric Contraction Shape on Incompressible Turbulent Flow", Journal of Fluids Eng., March 1976.

References: (Cont'd)

42. Townsend, A. A., "The Uniform Distortion of Homogeneous Turbulence", Quart. Journ Mech. and App. Math., Volume VII, Pt. 1, 1954.

43. Tucker, H. J., Reynolds, A. J., "The Distortion of Turbulence by Irrotational Plane Strain", J.F.M., Volume 32, Pt. 4, 1968.

44. Batchelor, G. K., "The Theory of Homogeneous Turbulence", Cambridge University Press. 1959.

45. Townsend, A. A., "The Passage of Turbulence Through Wire Gauzes", Quart. Journ. Mech. and App. Math., Volume 4, 1951.

46. Dryden, H. L. Schubauer, G. B., Appendix to (19).

47. Schubauer, G. B., Spangenberg, W. G., Klebanoff, P. S., "Aerodynamic Characteristics of Damping Screens", NACA TN-2001, 1950.

48. Baines, W. D., Peterson, E. G., "An Investigation of Flow Through Screens", Trans. of ASME, July 1951.

49. Durand, W. F., "Aerodynamic Theory", Volume II, Dover, 1963.

50. Schlicting, H., "Boundary Layer Theory", McGraw-Hill, 1960.

51. Paterson, R. W., "Transmittal of Loss Coefficient Data for Various Flow Obstructions", Internal Report 1976.

52. Bissinger, N. C., Braun, G. W., "On the Inlet Vortex System", NGR-43-001-086 Tenn. Univ. Space Inst. 1974.

53. Batchelor, G. K., "An Introduction of Fluid Dynamics", Cambridge University Press. 1974.

54. Ingard, W., Ising, H., "Acoustic Nonlinearity of an Orifice", J.A.S.A. Volume 42, Number 1, 1967.

55. Hersh, A. S., Rogers, T., "Fluid Mechanical Model of the Acoustic Impedance of Small Orifices", AIAA Paper 75-495, 1975.

56. Ronneberger' D., "The Acoustical Impedance of Holes in the Wall of Flow Ducts", Journal of Sound & Vibration, Volume 24, Part 1, 1972.

57. Rice, E. J., "A Theoretical Study of the Acoustic Impedance of Orifices in the Presence of a Steady Grazing Flow", NASA TM X-71903, 1976.

References: (Cont'd)

58. Bowman, J. J., Senior, T. B., Uslenghi, P. L. E., "Electromagnetic and Acoustic Scattering by Simple Shapes", North Holland Publishing Company, 1969.

59. Born, M., Wolfe, E., "Optics", Pergamon, 1965.

60. Robson, J. D., "Angular Transformation Properties of the Resolved Components of a Vector Random Process", J.S.V. Vol. 63, 1979.

61. Morse, P. M., Ingard, K. U., "Theoretical Acoustics", McGraw-Hill 1968.

1. Report No.	2. Government Accession No.	3. Recipient's Catalog No.
NASA CR-159189		

4. Title and Subtitle	5. Report Date
ANALYTICAL MODELS FOR USE IN FAN INFLOW CONTROL STRUCTURE DESIGN Inflow Distortion and Acoustic Transmission Models	December 1979
	6. Performing Organization Code
7. Author(s)	8. Performing Organization Report No.
M.R. Gedge	PWA-5580-32
	10. Work Unit No.
9. Performing Organization Name and Address	11. Contract or Grant No.
United Technologies Corporation Pratt & Whitney Aircraft Group - CPD East Hartford, Connecticut 06108	NAS1-15085
	13. Type of Report and Period Covered
12. Sponsoring Agency Name and Address	Contractor Report
National Aeronautics and Space Administration Washington, DC 20546	14. Sponsoring Agency Code

15. Supplementary Notes

Langley Technical Monitor: David Chestnutt
Phase II Interim Report

16. Abstract

Analytical models required for the development of an engine inflow control structure design system are presented and discussed. The effect of flow contraction and screening on velocity distortions is examined. The acoustic characteristics of honeycomb and perforated plate are quantified and qualitative inflow control structure design criteria are identified.

17. Key Words (Suggested by Author(s))	18. Distribution Statement
Inflow Control Structure, Turbulence, Flow Contraction, Screens, Vortex, Wake, Diffraction, Honeycomb	Unclassified - Unlimited

19. Security Classif. (of this report)	20. Security Classif. (of this page)	21. No. of Pages	22. Price*
Unclassified	Unclassified	159	

* For sale by the National Technical Information Service, Springfield, Virginia 22161